Towards functional oxide heterostructures

Dissertation zur Erlangung des
naturwissenschaftlichen Doktorgrades der
Julius-Maximilians-Universität Würzburg

vorgelegt von
Andreas Müller
aus Karlstein

Würzburg 2012

'It's all about the oxygen.'

Unknown

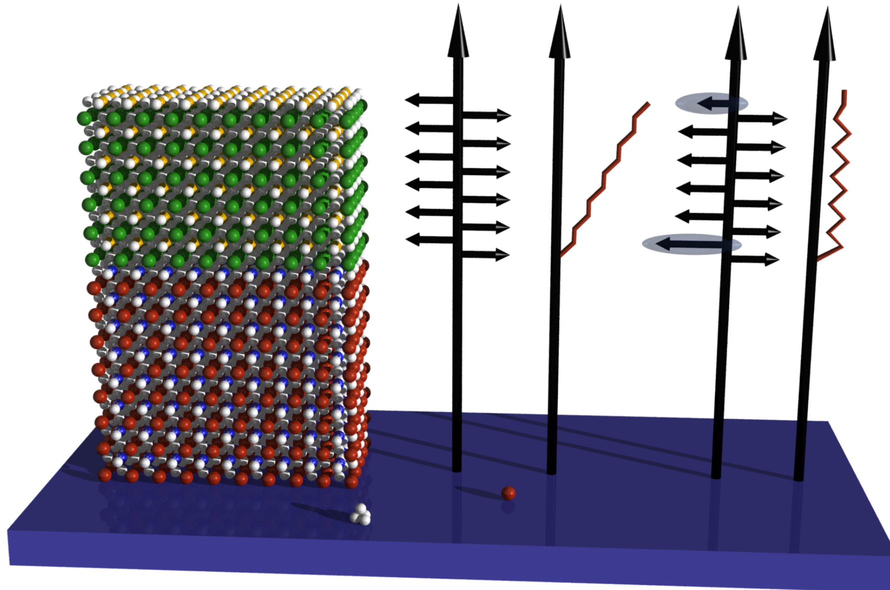

"The effervescent magic source of a seemingly inexhaustible flux of new and surprising properties is provided by a manifold of ways [1]."

Eingereicht am:

an der Fakultät für Physik und Astronomie

Gutachter der Dissertation:

1. Gutachter: Prof. Dr. R. Claessen

2. Gutachter: Prof. Dr. Ing. G. Rijnders

Prüfer im Promotionskolloquium:

1. Prüfer: Prof. Dr. R. Claessen

2. Prüfer: Prof. Dr. Ing. G. Rijnders

3. Prüfer: Prof. Dr. G. Sangiovanni

Tag des Promotionskolloquiums:

Doktorurkunde ausgehändigt am:

Contents

1 Introduction **1**

2 Growth and characterization of heterostructures **5**
2.1 Molecular beam epitaxy and pulsed laser deposition . . . 5
2.2 Thin film deposition and epitaxial growth . . . 7
2.3 Reflection high energy electron diffraction . . . 10
2.4 X-ray diffraction and reflectivity . . . 13
2.5 Photoelectron spectroscopy . . . 20

3 Fe_3O_4/ZnO – growth of a possible spin electrode **27**
3.1 Heterostructures for spin injection . . . 27
3.2 Physical properties and thin film growth . . . 29
3.3 Identification of different iron oxides by means of XPS . . . 31
3.4 Surface preparation of ZnO substrates . . . 33
3.5 Influence of the oxygen partial pressure on the iron oxide formation during PLD growth . . . 35
3.6 Comparison of Fe_3O_4 films grown by PLD and MBE . . . 38
3.6.1 Structure and morphology . . . 39
3.6.2 Electronic and chemical structure studied by XPS and HAXPES . 45
3.6.3 Magnetic properties . . . 47
3.6.4 Indications for a Verwey transition . . . 52
3.7 Tailoring the interface – pressure variation during growth . . . 54
3.8 Summary and outlook . . . 55

4 $LaAlO_3$/$SrTiO_3$ – growth conditions and interface electron system **57**
4.1 Introduction to perovskite oxides . . . 57
4.2 Conducting interface of $LaAlO_3$/$SrTiO_3$ . . . 59
4.3 $SrTiO_3$ substrate preparation . . . 63
4.4 Film growth and structural characterization . . . 64
4.5 Transmission electron microscopy and electron-energy loss spectroscopy . 66
4.6 Extrinsic and intrinsic interface effects . . . 71
4.7 Summary and outlook . . . 78

5 $LaVO_3$/$SrTiO_3$ – electrostatic doping of a Mott insulator **79**
5.1 Introduction . . . 79

5.2 Doping of a Mott insulator 81
5.3 Growth and characterization 83
5.4 Thickness-dependent transport properties 88
5.5 Charge transfer within the film 89
5.5.1 Analysis of core-level and valence band spectra 89
5.5.2 A more detailed view on the vanadium spectra 94
5.5.3 Band bending and band alignment 102
5.6 Summary and outlook 106

6 Summary **109**

Appendix **111**

Bibliography **113**

List of own publications **125**

Acknowledgement **127**

Curriculum vitae **129**

Erklärungen **131**

List of Figures

2.1 Sketch of an (a) MBE setup and (b) PLD growth setup. 6
2.2 Schematics of surface processes taking place during growth. 8
2.3 Possible growth modes derived from thermodynamic and kinematic considerations. 9
2.4 Ewald sphere construction for a 2D surface. 11
2.5 Film coverage and RHEED oscillations 13
2.6 Bragg scattering off a single crystal. 14
2.7 N-slit function, XRD pattern. 16
2.8 Possible XRD scan modes. 17
2.9 X-ray reflection and transmission from a slab. 19
2.10 Relation between the electronic structure of a crystal and the photoemission spectrum. 20
2.11 (a) Inelastic mean free path of electrons, (b) Schematics of HAXPES. . . 23

3.1 (a) Schematics of a spin-injection device. (b) Density of states for Fe_3O_4. 28
3.2 Lattice structure of (a) ZnO and (b) Fe_3O_4. 30
3.3 X-ray photoemission spectra of iron oxide single crystals. 32
3.4 AFM characterization of ZnO substrates. 33
3.5 Characterization of prepared ZnO substrates by RHEED and LEED. . . 34
3.6 AFM and RHEED of iron oxide films prepared at different O_2 pressures. 36
3.7 Film to substrate registry analyzed by off-axis RHEED. 37
3.8 XPS of the iron oxide thin films prepared at different O_2 pressures. . . . 38
3.9 (a) RHEED of a Fe_3O_4/ZnO film as a function of time. (b) Relaxation of the surface lattice constant during growth. (c) AFM image of a 19 nm Fe_3O_4/ZnO film 39
3.10 LEED pattern of a Fe_3O_4/ZnO thin film. 41
3.11 (a) XRR, (b) θ-2θ and ω-scan XRD of a Fe_3O_4/ZnO film. 42
3.12 Reciprocal space maps of Fe_3O_4/ZnO films. 44
3.13 XPS spectra of Fe_3O_4/ZnO and Fe_3O_4/MgO films grown by PLD and MBE: (a) Data fitted with single crystal reference and (b) Comparison of Fe $2p$ spectra. 46
3.14 XAS and XMCD spectra of Fe_3O_4/ZnO and Fe_3O_4/MgO films. 47
3.15 In-plane and out-of-plane magnetization curves measured by XMCD, MOKE and VSM for films on ZnO and MgO grown by MBE and PLD 50

3.16 Temperature dependence of coercivity for Fe_3O_4 films grown by PLD. . . 53
3.17 XPS and HAXPES depth profiling of Fe_3O_4/ZnO film of different thicknesses. 54

4.1 Perovskite lattice structure. 58
4.2 Schematics of the electronic reconstruction in LAO/STO. 60
4.3 Sheet resistance of LAO/STO: Dependence on the oxygen partial pressure. 62
4.4 AFM characterization of STO substrates. 63
4.5 RHEED characterization of LAO/STO film growth. 64
4.6 RHEED and AFM characterization for LAO/STO growth at HP. 65
4.7 XRR for LAO/STO prepared at different oxygen pressures. 66
4.8 HAADF-STEM for LAO/STO prepared at different oxygen pressures. . . 67
4.9 HAADF intensity cross-sections for LAO/STO films. 68
4.10 Spatial-resolved intensity cross-sections for LAO/STO grown at HP. . . . 69
4.11 EELS at the Ti, O, and La edges for LAO/STO samples. 70
4.12 EELS at the Ti $L_{2,3}$-edge for growth at medium pressure. 71
4.13 Sheet resistance of differently prepared LAO/STO films. 72
4.14 HAXPES of LAO/STO samples prepared under different conditions. . . . 73

5.1 Potential build-up in LAO/STO vs. LVO/STO 80
5.2 Band structure and phase diagram of a Mott insulator 81
5.3 Growth phase diagram of thick $LaVO_x$ films 84
5.4 RHEED and AFM characterization of LVO/STO films 85
5.5 XRR, XRD and reciprocal space map of LVO/STO films. 86
5.6 HAADF-STEM of a 10 uc LVO/STO film. 87
5.7 Transport properties of LVO/STO films 88
5.8 HAXPES V 2*p* spectra for a 6 uc and a 10 uc LVO/STO film. 89
5.9 HAXPES Ti 2*p* spectra for 6 uc and 10 uc LVO/STO films. 90
5.10 HAXPES valence band spectra for LVO/STO films. 91
5.11 Model of an electronic reconstruction scenario in LVO/STO. 93
5.12 XPS spectra of a 6 uc LVO/STO upon reduction and oxidation. 95
5.13 HAXPES V 2*p* spectra of vandium oxide single crystals. 97
5.14 Single crystal fit of LVO film data. 98
5.15 Multiplet simulations for the LVO films. 100
5.16 Band bending and band offset for the Sr 3*d* core-level and the valence band. 103
5.17 Possible band alignment in LVO/STO. 105

List of Tables

3.1 Roughness, surface lattice constant and film composition of differently prepared iron oxide thin films. 35
3.2 XRR analysis of Fe_3O_4 films. 43
3.3 In-plane and out-of-plane strain calculated from asymmetric Bragg peaks. 44
3.4 Off-stoichiometry parameters of $Fe_{3-\delta}O_4$ films derived from XPS, XAS and XMCD analyses. 48
3.5 Magnetic moments derived by sum-rule calculations (XMCD) and VSM analyses 49
3.6 Quantitative analysis of the anti-phase boundary density. 52

4.1 Comparison of sample properties of 6 uc LAO/STO films derived from transport and Hall measurements. 76

5.1 Reduction and oxidation series of the 6 uc LVO/STO film. 94
5.2 Average vanadium valence of 6 uc and 10 uc LVO/STO films 98
5.3 Average vanadium valence during reduction and oxidation. 99
5.4 Average vanadium valence derived from multiplet calculations. 101
5.5 Band offsets and band bending in the STO determined by XPS. 104
5.6 Band gap and electron affinities for STO and LVO bulk materials. 104

6.1 Table of investigated samples. 111

List of acronyms

2DES	two-dimensional electron system
AFM	atomic force microscopy
APB	anti-phase boundary
CBM	conducting band minimum
DOS	density of states
EELS	electron-energy loss spectroscopy
FWHM	full width at half maximum
HAADF	high angle annular dark field
HAXPES	hard x-ray photoelectron spectroscopy
HP	high pressure
IMFP	inelastic mean free path
LEED	low-energy electron diffraction
LHB	lower Hubbard band
LP	low pressure
MBE	molecular beam epitaxy
MIT	metal-insulator transition
ML	monolayer
MOKE	magneto-optical Kerr effect
MP	medium pressure
PES	photoelectron spectroscopy
PLD	pulsed laser deposition
RHEED	reflection high energy electron diffraction
rms	root mean square
RSM	reciprocal space map
SQUID	superconducting quantum interference device
STEM	scanning transmission electron microscopy
uc	unit cell
UHB	upper Hubbard band
UHV	ultra-high vacuum
VBM	valence band maximum
VSM	vibrating sample magnetometer
XAS	x-ray absorption spectroscopy
XMCD	x-ray magnetic circular dichroism
XPS	x-ray photoelectron spectroscopy
XRD	x-ray diffraction
XRR	x-ray reflectivity

Abstract

Oxide heterostructures attract a lot of attention as they display a vast range of physical phenomena like conductivity, magnetism, or even superconductivity. In most cases, these effects are caused by electron correlations and are therefore interesting for studying fundamental physics, but also in view of future applications. This thesis deals with the growth and characterization of several prototypical oxide heterostructures.

Fe_3O_4 is highly ranked as a possible spin electrode in the field of spintronics. A suitable semiconductor for spin injection in combination with Fe_3O_4 is ZnO due to its oxide character and a sufficiently long spin coherence length. Fe_3O_4 has been grown successfully on ZnO using pulsed laser deposition and molecular beam epitaxy by choosing the oxygen partial pressure adequately. Here, a pressure variation during growth reduces an FeO-like interface layer. Fe_3O_4 films grow in an island-like growth mode and are structurally nearly fully relaxed, exhibiting the same lattice constants as the bulk materials. Despite the presence of a slight oxygen off-stoichiometry, indications of the Verwey transition hint at high-quality film properties. The overall magnetization of the films is reduced compared to bulk Fe_3O_4 and a slow magnetization behavior is observed, most probably due to defects like anti-phase boundaries originating from the initial island growth.

$LaAlO_3/SrTiO_3$ heterostructures exhibit a conducting interface above a critical film thickness, which is most likely explained by an electronic reconstruction. In the corresponding model, the potential built-up owing to the polar $LaAlO_3$ overlayer is compensated by a charge transfer from the film surface to the interface. The properties of these heterostructures strongly depend on the growth parameters. It is shown for the first time, that it is mainly the total pressure which determines the macroscopic sample properties, while it is the oxygen partial pressure which controls the amount of charge carriers near the interface. Oxygen-vacancy-mediated conductivity is found for too low oxygen pressures. A too high total pressure, however, destroys interface conductivity, most probably due to a change of the growth kinetics. Post-oxidation leads to a metastable state removing the arbitrariness in controlling the electronic interface properties by the oxygen pressure during growth.

$LaVO_3/SrTiO_3$ heterostructures exhibit similar behavior compared to $LaAlO_3/SrTiO_3$ when it comes to a thickness-dependent metal-insulator transition. But in contrast to $LaAlO_3$, $LaVO_3$ is a Mott insulator exhibiting strong electron correlations. Films have been grown by pulsed laser deposition. Layer-by-layer growth and a phase-pure pervoskite lattice structure is observed, indicating good structural quality of the film and the interface. An electron-rich layer is found near the interface on the $LaVO_3$ side for conducting $LaVO_3/SrTiO_3$. This could be explained by an electronic reconstruction within the film. The electrostatic doping results in a band-filling-controlled metal-insulator transition without suffering from chemical impurities, which is unavoidable in conventional doping experiments.

Zusammenfassung

Oxidische Heterostrukturen besitzen verschiedenste physikalische Eigenschaften wie Leitfähigkeit, Magnetisums oder sogar Supraleitung. Diese Effekte, die meist von elektronischen Korrelationen verursacht werden, zu verstehen und ihren fundamentalen Ursprung zu erklären, machen diese Materialsysteme ebenso interessant wie ihr zukünftiges Anwendungspotential. Diese Arbeit beschäftigt sich mit verschiedenen prototypischen Schichtsystemen.

Fe_3O_4 könnte zukünftig als Spinelektrode im Bereich der Spintronik dienen. ZnO ist ein Halbleiter, der durch seinen oxidischen Charakter und einer hinreichenden Spinkohärenzlänge gut zur Spininjektion geeignet ist. Das Wachstum von Fe_3O_4 auf ZnO wurde erfolgreich mittels gepulster Laserdeposition und Molekularstrahlepitaxie durchgeführt. Dabei ist der Sauerstoffpartialdruck entscheidend und eine Variation des Drucks während des Wachstums wirkt der Bildung einer FeO-artigen Grenzschicht entgegen. Die Filme wachsen inselartig und ihre Gitterstruktur ist fast vollständig relaxiert. Trotz einer Sauerstofffehlstöchiometrie wird die hohe Qualität der Filme durch einen Verwey-Phasenübergang bestätigt. Im Vergleich zu Einkristallen ist die Magnetisierung der Filme reduziert. Durch das Inselwachstum verursachte Antiphasengrenzen könnten zu dieser Reduzierung führen.

Die leitfähige Grenzschicht, die in $LaAlO_3/SrTiO_3$ Heterostrukturen ab einer bestimmten $LaAlO_3$ Filmdicke auftritt, kann höchstwahrscheinlich durch eine elektronische Rekonstruktion erklärt werden. Im entsprechenden Modell wird der Aufbau eines elektrischen Potentials auf Grund der Polarität des $LaAlO_3$ Films durch eine Ladungsumordnung kompensiert. Die Eigenschaften dieser Heterostruktur sind jedoch von den Wachstumsparametern abhängig. Diese Studie zeigt erstmals, dass die makroskopischen Eigenschaften maßgeblich vom Gesamtdruck, die Anzahl der Ladungsträger dagegen stark vom Sauerstoffpartialdruck während des Wachstums abhängen. Leitfähigkeit auf Grund von Sauerstofffehlstellen wurde für sehr kleine Sauerstoffpartialdrücke beobachtet. Ein zu hoher Gesamtdruck hingegen verhindert die Leitfähigkeit der Grenzschicht. Dies ist vermutlich durch eine Änderung der Wachstumskinematik erklärbar. Ein Nachoxidieren der Proben führt überdies zu einem metastabilen Zustand, der die Vergleichbarkeit von Proben verschiedener Arbeitsgruppen gewährleistet.

$LaVO_3/SrTiO_3$ zeigt ähnliches Verhalten wie $LaAlO_3/SrTiO_3$ und Leitfähigkeit tritt ab einer gewissen $LaVO_3$ Schichtdicke auf. Im Gegensatz zu $LaAlO_3$ ist $LaVO_3$ ein Mottisolator, dass heißt, Korrelationseffekte spielen eine Rolle. $LaVO_3/SrTiO_3$ wurde mittels gepulster Laserdeposition hergestellt, Phasenreinheit und die strukturellen Eigenschaften mit verschiedenen Methoden überprüft. Zusätzliche Elektronen wurden für leitfähige Proben auf der $LaVO_3$-Seite der Grenzfläche nachgewiesen. Eine Erklärung hierfür wäre eine elektronische Rekonstruktion im Film selbst. Dieses elektrostatische Dotieren führt zu einem bandfüllungsinduzierten Mott-Phasenübergang, der nicht durch chemische Verunreinigungen, die in konventionellen Dotierexperimenten unvermeidbar sind, beeinflusst ist.

1 Introduction

Today's scientific work often proves to be a balancing act between technologically relevant research and fundamental research. Conceiving and developing new concepts for future applications and devices is for instance often seen as a basic prerequisite for granting a proposal. In contrast, research to explore and understand a physical effect may at first hand appear less attractive, nevertheless is undoubtedly essential and fundamental for technological progress. One great example of this is the discovery of the tunnel magnetoresistance effect. In less than a decade after its discovery it revolutionized the way of data reading and writing on a hard drive [2, 3].

Oxide heterostructures are a class of material systems that minimize this balancing act as they offer great potential for applications and at the same time are most interesting for studying fundamental physics. The palette of available oxides provides various possibilities to design and fabricate interfaces and heterostructures with functional properties. The vast zoo of physical properties that are found in transition metal oxides, for example, conductivity changing over several orders of magnitude, various forms of magnetism, or superconductivity, are caused by the interaction of the electrons in the d-shell. These electronic interactions distinguish the transition metal oxides from conventional semiconductors, where the electrons can be treated as free and barely interacting particles. Furthermore, the interfaces of these heterostructures exhibit physical properties that are not present in their bulk constituents. From a technological point of view this offers new prospects of engineering electronic devices that are faster, smaller and at the same time less power-consuming and might be capable of replacing conventional silicon-based electronics. The headlines of articles in relevant journals, like 'The interface is still the device', which is a reformulation of H. Kroemers statement in his Nobel laureate, 'Interface takes charge over Si', 'Oxide Electronics Emerge', and 'Oxide Interfaces - An opportunity for Electronics' point to that direction [4–7]. Although the understanding of these material systems is still in its infancy and the focus is to understand the underlying physical principles, first attempts to develop devices based on these interface effects are currently made [8].

The artificial fabrication of these heterostructures and the engineering of their interface is a basic prerequisite to analyze and afterwards also utilize these systems. The development of advanced growth techniques like molecular beam epitaxy (MBE) and pulsed laser deposition (PLD) makes it possible to grow complicated material compositions stoichiometrically. Precise interfaces and film growth with the precision of one atomic layer are achieved, as growth can be live-monitored using reflection high energy electron diffraction (RHEED). The capability of these growth methods is evidenced by

headlines like 'Oxide Electronics on Demand' or 'Build your own superlattices' [9, 10]. On the interplay of studying basic physical concepts and fabricating heterostructures suited for building devices, this thesis deals with three material systems:

The first one is the heterostructure formed by Fe_3O_4 and ZnO. This structure is highly ranked as a possible material system suitable for spin injection. While in conventional electronics the charge of the electron is exploited as a degree of freedom for manipulation, in so-called spintronics the spin degree of freedom is additionally used. This would, for instance, enable devices like a spin transistor proposed by Data and Das [11]. Both materials match the required properties for spin injection, namely a high degree of spin polarization in Fe_3O_4 as an injection electrode and well-defined semiconducting properties of ZnO [12–14]. Furthermore, the oxide character of ZnO makes it perfectly suitable for the combination with Fe_3O_4. Nevertheless, reports of successful growth of heterostructures are rare. The aim of this thesis is growing these heterostructures by means of MBE and PLD. A comparative study of structural, chemical, electronic and magnetic properties of these structures is presented. These findings can be seen as a first step towards device fabrication.

The second structure under investigation is composed of the two band insulators $LaAlO_3$ (LAO) and $SrTiO_3$ (STO). Finding conductivity in these perovskite structures above a critical LAO overlayer thickness by Ohtomo *et al.* attracted a lot of interest [15]. A detailed study of this system revealed the coexistence of both superconductivity and magnetism in the ground state, which is exceedingly interesting from a physical point of view [16]. Furthermore, the system did also prove its future device applicability as the interface conductivity could be controlled by a gate field [17]. Nevertheless, a conclusive explanation for the thickness-dependent conductivity is still missing. Among other considerations, there are strong indications for an electronic reconstruction owing to the polar character of LAO to avoid the so-called polar catastrophe to be the driving mechanism for the conductivity [18]. In this thesis, the influence of the growth conditions on the structural and electronic properties of these heterostructures is studied, especially addressing the influence of the growth kinetics, the oxidation potential during growth and a post-growth treatment. From this detailed analysis, a recipe to fabricate high-quality structures for a further study of the physical properties but also for device reproducibility is given.

The third structure might offer the most innovational, but also the most speculative perspectives for future applications, but provides already today a playground for studying the physics of correlated electron systems: $LaVO_3/SrTiO_3$ (LVO/STO). This structure is closely related to the LAO/STO system. However, in contrast to LAO, LVO is a Mott insulator. As in the case of LAO/STO, a thickness-dependent metal-insulator transition is observed, which may also be explained by an electronic reconstruction [19]. Additionally, correlation effects in the Mott insulating LVO may lead to new and striking physics. An example would be a band-filling-induced Mott transition without any impurity doping by pure electrostatics. Going further into the future, so-called 'Mottronic' devices may enable switching between two electronic states without the motion of charge

carriers on significant length scales [20, 21]. Leaving the latter point for dreams of the future, the physical properties of LVO/STO structures are analyzed within this thesis. Firstly, a thorough phase characterization and structural characterization is presented. Secondly, spectroscopic studies give insights into the electronic structure and correlation effects at play in these heterostructures.

This work is arranged as follows: The second chapter gives an introduction to PLD and MBE including the live-monitoring by RHEED. Furthermore, the basic principles of x-ray diffraction and photoelectron spectroscopy are discussed. The third chapter is concerned with a comparative study of Fe_3O_4/ZnO heterostructures grown by PLD and MBE. In chapter four, the influence of the growth conditions on the properties of $LaAlO_3$/$SrTiO_3$ heterostructures is presented, whereas the fifth chapter deals with the $LaVO_3$/$SrTiO_3$ hybrid system.

2 Growth and characterization of heterostructures

The growth of semiconductor heterostructures demands highest cleanliness, purity and epitaxial standards with a growth precision in the atomic monolayer (ML) regime. This led to the development of a deposition technique which can be carried out in ultra-high vacuum (UHV) and can be real-time monitored. Using molecular beam epitaxy (MBE), thin film growth can be achieved in highest epitaxial and stoichiometric quality. The invention of reflection high energy electron diffraction (RHEED) enables the direct monitoring of the film surface and thus the film growth. Examples of the success of MBE are the growth of GaAs heterostructures as well as AlGaAs quantum dots [22, 23]. More recently, MBE has been used for the fabrication of HgTe topological insulators [24].

The high-T_c days of superconductor research in the late 1980s led to the spread of a growth technique called pulsed laser deposition (PLD). This technique allowed the deposition of high-T_c materials like $YBa_2Cu_3O_7$ and $Bi_2Sr_2Ca_2Cu_3O_{10}$ in oxygen atmosphere [25, 26]. Using this method, it is possible to achieve the stoichiometric deposition of various compounds by the ablation from a single target only. Especially suited for oxide films, the deposition in a high oxygen background pressure counteracts the often-reported occurrence of oxygen deficiency in other growth methods. Naturally, both techniques have advantages and disadvantages, making them valuable in their particular application fields, which of course exhibit some overlap.

In the course of this thesis both methods were used for film deposition. In Chapt. 3, a comparative study of MBE and PLD grown Fe_3O_4/ZnO films is presented, while Chapt. 4 and 5 deal with films grown by PLD.

2.1 Molecular beam epitaxy and pulsed laser deposition

A sketch of an MBE growth setup is displayed in Fig. 2.1 (a). The UHV chamber, which allows a base pressure as low as 10^{-11} mbar, is equipped with individual evaporation sources and a heater which also serves as a substrate holder. Using radiative heating, substrate temperatures up to 1000 °C can be reached. The evaporation sources provide molecular beams of the desired elements. For this work, an electron beam evaporator is

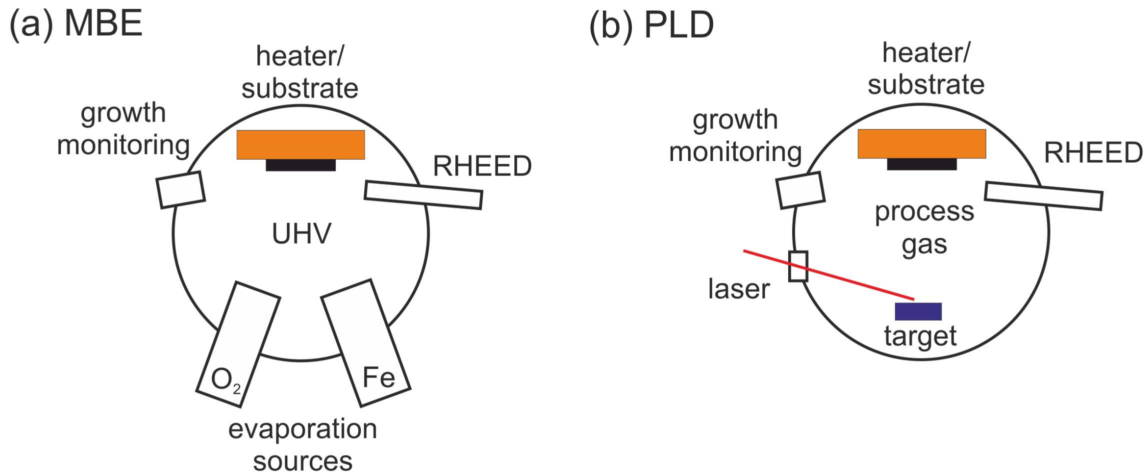

Figure 2.1: *(a) MBE growth setup with two individual evaporation sources for the respective materials. (b) PLD growth setup. A laser is used to ablate the material from a single target. Both setups are equipped with a RHEED system for growth monitoring.*

used to heat a high purity iron rod, whereas molecular oxygen is supplied in gaseous form via a needle valve. The heated substrate is placed directly in front of the evaporation sources. Growth is started by opening the shutters of the various individual sources, which enables for instance multilayer growth. During the simultaneous evaporation of the constituents, the flux of each evaporation source can be controlled separately. Thus, film composition can be tuned and stoichiometric film growth can be achieved. Furthermore, a RHEED setup is attached to study the growth mechanism and monitor the film thickness, which will be further explained in Sec. 2.3. Typical deposition rates are about 0.2-5 nm/min. These time scales are long enough to manually manipulate the shutters of the evaporators and in this way control the film growth in the sub-monolayer regime.

In comparison, a schematic drawing of a PLD growth setup is shown in Fig. 2.1 (b). The evaporation sources are replaced by *one* target which contains all constituents of the desired films in the right stoichiometry. A high density, homogeneity and purity of the target are essential for a uniform and stoichiometric ablation. Thus, single crystalline or ceramic targets are used preferably. For the ablation, a short high-energy laser pulse in the UV regime (λ=248 nm) is used. This pulse causes a sudden evaporation of the topmost layer of the target. Furthermore, the absorption causes the partial ionization of the vapor and the generation of the so-called plasma plume, which is composed of neutral atoms, positive and negative ions, and electrons. The adiabatic expansion results in a high anisotropy, which in turn results in the plume being strongly forward directed towards the substrate [27]. The plume particles exhibiting high kinetic energies are slowed down by collisions with the process gas. This causes a thermalization of the particles, and sputtering effects on the substrate are avoided at high enough background/process gas pressures. This means that plume kinetics can be influenced by changing the back-

ground gas pressure. Typically, the process pressure can be varied over a wide range between 0.5 and 10^{-6} mbar. The influence of the background gas pressure on the growth kinetics is described by several models [27, 28].* Besides the pressure, the background gas itself also has an effect on the plume constituents and the stoichiometry of the film. Argon and nitrogen, for instance, are inert gases and thus only affect the growth kinetics. On the contrary, oxygen changes the chemistry of the plume, as the particles in the plume are oxidized at sufficiently high background pressures. Moreover, the oxygen background gas provides a reservoir to refill oxygen vacancies in the grown film resulting from the non-stoichiometric oxygen ablation from the target. The average growth speed lies in the range of 1-10 nm/min. Thereby, the average growth rate is determined by the pulse repetition rate (mainly the time between the pulses), whereas the instantaneous deposition rate is determined by the laser energy per pulse. As the laser energy is not spatially constant over the laser spot profile, a mask is used to filter out the parts with the highest inhomogeneity. Furthermore, a lens system is used to image the mask on the target. This ensures a uniform ablation from the target and avoids splashing effects. These effects would be predominant, if the target was placed in the focal point of the lens. Additionally, the laser beam is scanned over the target for uniform ablation. The laser energy which determines the amount of ablated material is controlled by an attenuator consisting of a mirror-absorber system. The duration of the laser pulse is about 25 ns, while the laser pulse repetition rate lies between 0.5 - 2 Hz. This means that, the ablated material is provided on a comparably short time scale, whereas nucleation and growth mainly take place on longer time scales (1 μs) between the laser pulses. In the PLD setup as well, RHEED is used to monitor the growth, although special care must be taken to account for the high process gas pressure.

2.2 Thin film deposition and epitaxial growth

Thin film deposition in general can be described in a three step model, starting with the particle creation, the transport of these particles towards the substrate and finally the nucleation on the substrates. The film growth is called 'epitaxial', when film structure and film orientation are determined by the substrate. The particles are created by thermal heating in the case of MBE and laser-induced plasma formation in the case of PLD. In MBE the transport of the particles is determined by their thermal velocity, while in PLD, the fast particles of the plume undergo collisions with the process gas, which lead to a thermalization. Comparing the typical substrate-to-source distance with the mean free path of the particles, collisions play a dominant role only for growth pressures higher than 10^{-3} mbar [29]. For the growth of Fe_3O_4/ZnO by PLD and MBE (see Chapt. 3),

*Within the 'drag force' and the 'shockwave model', the attenuation of the kinetic energy of the plume particles is described for low and high background pressures, respectively [28]. The 'thermalization model' derives the so-called 'plasma range' as a characteristic length scale for a PLD setup [27].

molecular oxygen is supplied in both cases in the gaseous form and the oxygen partial pressure was chosen between 10^{-5} and 10^{-6} mbar. Although the oxidation states of the iron oxide films vary tremendously in this pressure regime, the oxidation of the particles on their way to the substrate can be neglected and the oxidation is essentially restricted to the nucleation and growth step. In contrast, the PLD growth of LAO/STO heterostructures (see Chapt. 4) was conducted at oxygen partial pressures between 10^{-1} and 10^{-5} mbar, where the oxidation of the particles on the way to the substrate cannot be neglected for all pressures and changes in the growth can be suspected. A high process pressure in PLD growth also influences the particle angular distribution and stoichiometry of the plume.

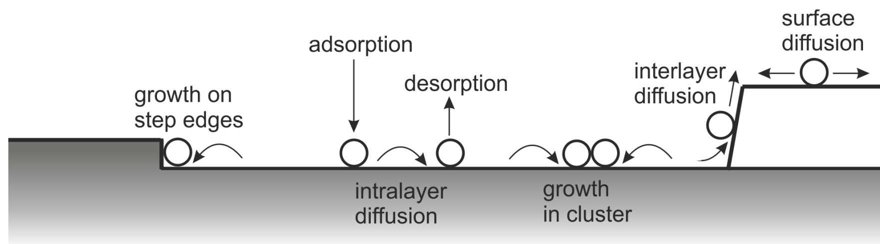

Figure 2.2: *Schematics of surface processes taking place during growth (adapted from [30]).*

The process of sub-monolayer particle nucleation and growth on a substrate can be viewed as an interplay between different physical and chemical surface processes as illustrated in Fig. 2.2 [30]. After the particles have arrived on the substrate, they are adsorbed by van der Waals forces. The bonds in this so-called physisorbed state are comparably weak, as no electrons are transferred between adsorbate and substrate. Thus, the surface diffusion length and the desorption rate are high. The kinetic energy for these processes is provided by the substrate. In the case of PLD the particles, too, have a certain kinetic energy due to the ablation process, which makes diffusion and desorption even easier. Chemisorption leads to the formation of chemical bonds and particles are preferably incorporated at step edges, island boundaries or they start to form clusters which are stable above a critical size. The ratio between the particles adhering to the substrate surface and the total number of arriving particles is called sticking coefficient. It strongly depends on the substrate temperature, the surface coverage and the kinetic energy of the adsorbed particles.

In homoepitaxy, where the film material and the substrate material are identical, three different growth modes, as displayed in Fig. 2.3 (a)-(c), can be defined. Assuming thermodynamic equilibrium, the relation of the free energies of the substrate surface (γ_s), the film surface (γ_f) and the free energy of the interface (γ_i) determine the growth mode [30]. According to this, two-dimensional (2D) layer-by-layer growth or Frank-van-der-Merwe growth occurs when the surface energy of the substrate is higher than the surface energy of the growing film plus the interface energy of the film and the substrate ($\gamma_s > \gamma_i + \gamma_f$). Inversely, three-dimensional (3D) island growth, also called Volmer-Weber

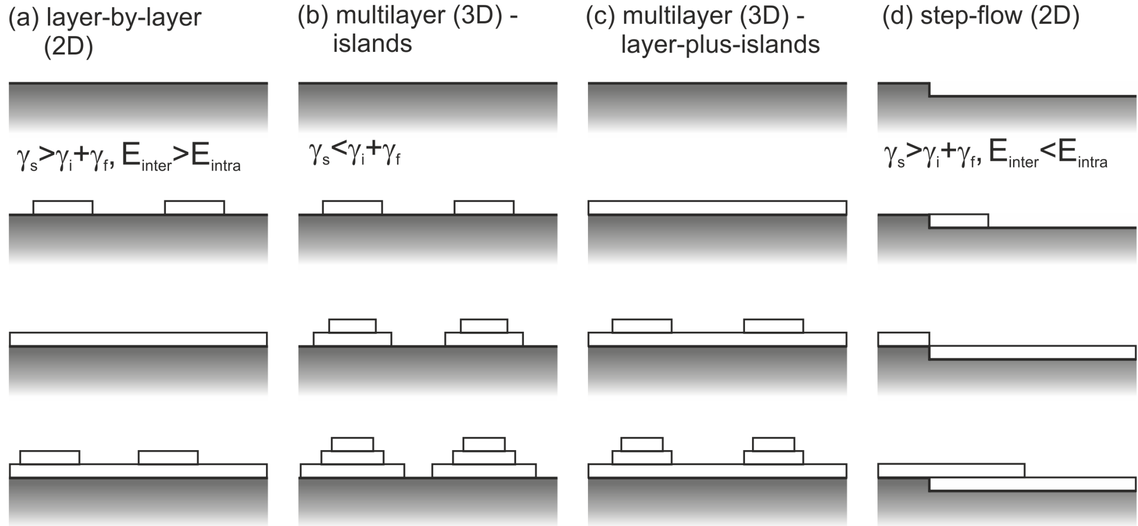

Figure 2.3: *Possible growth modes derived from thermodynamic and kinematic considerations. Depending on the free energies of the substrate surface γ_s, the film surface γ_f and the free energy of the interface γ_i as well as the interlayer E_{inter} and intralayer E_{intra} diffusion rates four different growth modes can be defined. For details see text.*

growth, can be found when the surface energy of the substrate is less than the surface energy of the film and the interface energy ($\gamma_s < \gamma_i + \gamma_f$). Finally, another mixed form is observed where initially a closed wetting layer is formed, on which 3D islands then start to grow. Here, the energy balance of the free energies depends on the film thickness. This is called layer-plus-island or Stranski-Krastanov growth.

However, also kinetic aspects have to be considered during epitaxial growth. Surface diffusion rates, for example, can be different on flat terraces (E_{intra}) compared to those across step edges (E_{inter}). For the 2D layer-by-layer growth mode, this leads to a distinction between a nucleation-coalescence mode (Fig. 2.3 (a)) and a step-flow mode (Fig. 2.3 (d)), whereas in the former mode, islands of the thickness of one ML are formed in the first place. The number of islands changes periodically during the formation of every ML, as nucleation takes place on the island edges. When islands coalesce, the number of edges changes as well and with this the step density. In the step-flow mode, nucleation only takes place at step edges already present on the substrate. Here, the step density is constant during growth as no new islands (and with this no new step edges) are formed. The time-dependent evolution of the step density is directly reflected by the RHEED intensity oscillations, which will be further discussed in Sec. 2.3.

In the case of heteroepitaxy, the growth mode also depends on the lattice parameters of the different materials. A 3D island growth mode can be observed in materials exhibiting a high lattice mismatch. Pseudomorphic growth, where the in-plane lattice constants are preserved, can be achieved up to a certain critical layer thickness [31]. Thereby, conserving the unit cell volume leads to the build-up of strain, which is compensated by

dislocations and crystalline defects. This destroys a desired 2D layer-by-layer growth.

Comparing deposition and growth in MBE and PLD, growth is determined in both methods by the kinetic energy of the particles, which is higher in the case of PLD. The main difference is that in MBE deposition and surface relaxation/organisation happens simultaneously, because the flux is continuous. In PLD, by contrast, a certain amount of material is deposited on a relative short time scale during the laser pulse and surface organisation mainly takes place *between* the laser pulses on a longer time scale. This can be seen as a recurring intermediate annealing step [32]. As concerns the growth of oxide compounds, special care has to be taken of the oxygen stoichiometry and the oxygen supply. For the MBE growth of Fe_3O_4/ZnO films this will be further discussed in Chapt. 3. For PLD ablation it is well known that oxygen is not transferred stoichiometrically from the target. Thus, a certain oxygen partial pressure background has to be supplied during growth. However, certain compounds do not form at too high oxygen growth pressures, e. g., $LaTiO_3$ overoxidizes to $La_2Ti_2O_7$. Nevertheless, stoichiometric $LaTiO_3$ can be achieved by post-annealing at a high oxygen partial pressure and at moderate temperatures. The influence of such a procedure on the properties of $LaAlO_3/SrTiO_3$ heterostructures will be discussed in Chapt. 4.

2.3 Reflection high energy electron diffraction

For the real-time monitoring of the thin film deposition and the atomic structure analysis of the substrate and the grown film, a RHEED system is used. This system consists of an electron gun, which provides electrons with an energy of 10-50 keV, and a phosphor screen to detect the diffracted electrons. The magnitude of the wavevector $|\mathbf{k}_0|$ for high-energy electrons is given by

$$|\mathbf{k}_0| = \frac{1}{\hbar}\sqrt{2m_0E + \frac{E^2}{c^2}}. \tag{2.1}$$

This formula includes relativistic corrections, which amount to about 3 % for 20 keV electrons. The wavevector of these electrons is about 70 Å^{-1}, which is approximately 60 times larger than the vector defining the reciprocal unit cell of the crystal [33]. The electron beam hits the sample surface with a low incidence angle of 0.2-3°. This makes the technique very surface sensitive with electron diffraction only occurring in the first atomic layers as $|\mathbf{k}_{0\perp}|$ corresponds to energies below 1000 eV [34]. The great advantage of this method is that due to the geometric arrangement it can be used during deposition. For application during a high-pressure PLD process, the phosphor screen has to be mounted as close as possible to the sample, as the electron mean free path decreases with increasing pressure [29]. Additionally, the electron gun has to be pumped efficiently to extend filament lifetime. From the pattern of the diffracted electrons one can determine film growth modes, in-plane lattice constants and terrace width of vicinal

substrates. Furthermore, the sensitivity to morphology and surface roughness allows a determination of the growth speed in the case of layer-by-layer growth.

RHEED pattern

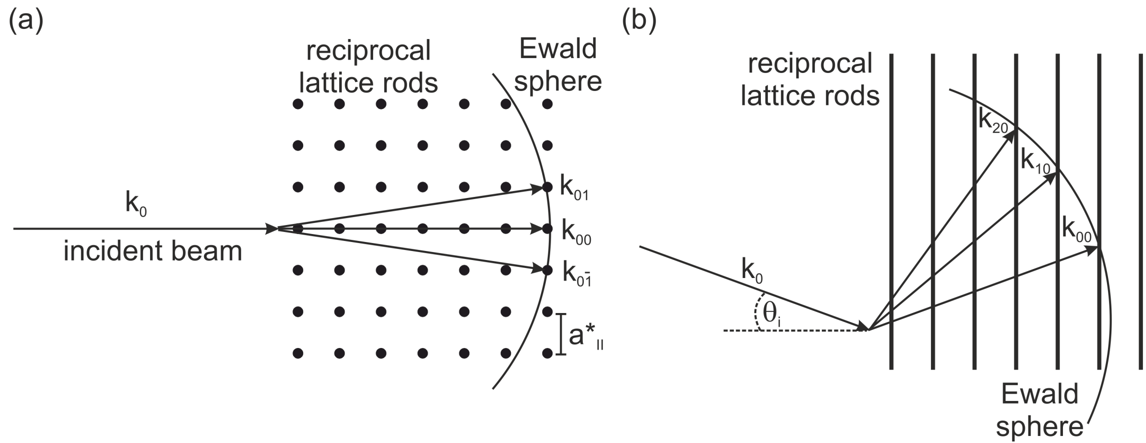

Figure 2.4: *Ewald sphere construction for a 2D surface: (a) top view and (b) side view. A 2D surface is represented by rods in reciprocal space. RHEED spots appear for every intersection of the Ewald sphere, whose radius is defined by the modulus of the wavevector* $\mathbf{k}_0$ *of the incident electron beam, with a reciprocal lattice rod.*

As the penetration depth of the electrons is extremely low, the periodic part of the sample perpendicular to the surface can be neglected and diffraction occurs only at the 2D surface. This is schematically shown in Fig. 2.4, assuming a perfectly flat surface. The 2D surface of a cubic lattice in reciprocal space is represented by semi-infinite long rods, which appear as dots in the left part of the drawing (top view). The incident electron beam is characterized by its wavevector $\mathbf{k}_0$. θ_i is the angle between the surface and the incident electron beam. By rotating the sample around the surface normal (azimuth), the incident electron beam can be adjusted along a crystalline direction with high symmetry. Assuming elastic scattering, i. e., $|\mathbf{k}_0|=|\mathbf{k}_{\text{scattered}}|$, all scattered vectors lie on the so-called Ewald sphere. The radius of this sphere is given by $|\mathbf{k}_0|$. Constructive interference will only occur for the intersection of the Ewald sphere with the reciprocal lattice rods. In other words, the difference of $\mathbf{k}_{\text{scattered}}$ and $\mathbf{k}_0$ has to match exactly a reciprocal lattice vector $\mathbf{G}$. This relation is known as the Laue condition. Due to the high energy of the electrons the radius of the Ewald sphere is so large that the scattering condition is only fulfilled for a small number of lattice points. The 0th-order Laue circle is formed by the $(0k)$ spots, with the so-called specular (00) spot being never forbidden as the Laue condition is always fulfilled for $\mathbf{G}=0$.

For non-perfectly flat surfaces, e. g., caused by an increased surface roughness, crystalline defects, or a high miscut angle, the lattice rods get broadened and modulated in their thickness. This results in a broadening of the spots and the pattern gets more and

more streaky. Furthermore, the spots are broadened by the finite coherence length of the electron beam, which also gives a limit for the study of long range order using this technique. In the case of a higher surface roughness or a 3D island formation during growth, transmission spots occur, which change the pattern completely, as the lattice rods are replaced by lattice spots in reciprocal space. Randomly oriented crystallites can be identified, since their 3D pattern is almost independent of both the incident angle of the primary electron beam and the azimuthal orientation of the sample.

Up to now, a kinematical theory has been used to give a qualitative description of RHEED. Within these considerations, only single elastic scattering, as is the case for weakly interacting diffraction techniques like x-ray diffraction, was assumed. Non-linear effects like multiple scattering are included in dynamic scattering theories that account for the strong interaction of the electrons with the periodic potential of the crystal surface in a RHEED experiment. From this a more quantitative description can be derived [33]. Furthermore, additional features are observed in the RHEED pattern. One example of this are the so-called Kikuchi lines that result from inelastic scattering with phonons and plasmons [34]. The appearance of these lines can be explained by a two step-model. The primary electrons undergo collisions in the crystal that randomize the direction of the wavevectors. If the energy loss resulting from these collisions is small, the scattered electrons can be seen as an isotropic electron source. This isotropic radiation is also diffracted by the crystal, which results in the Kikuchi line pattern [33]. However, as this scattering mechanism is comparably weak, these lines are only visible in the patterns of samples that exhibit a high crystalline quality. Performing a more sophisticated analysis of these lines, one can get further information on the average crystal potential and vicinal misorientation of the surface, which is beyond the scope of this thesis and the reader is referred to Refs. [33, 35].

RHEED oscillations

Intensity oscillations of the specular spot were first observed during growth of GaAs by means of MBE [36, 37]. These so-called RHEED oscillations only appear for well-ordered 2D layer-by-layer growth and can be linked to the completion state of a single monolayer.

A schematic illustration is shown in Fig. 2.5. Diffuse electron scattering occurs on surface steps and terrace edges and thus strongly depends on the density of these features. Surface roughening and smoothing periodically changes during growth, which comes along with a periodic variation in the step density. A fully grown monolayer exhibits the smallest amount of steps and thus the spot intensity is highest. In contrast, after the growth of half a monolayer the spot intensity is lowest. In practice, a recovery of the full intensity is only achieved for homoepitaxy and ideal growth conditions. In heteroepitaxy a small change in lattice constants already results in a drop of intensity for the very first

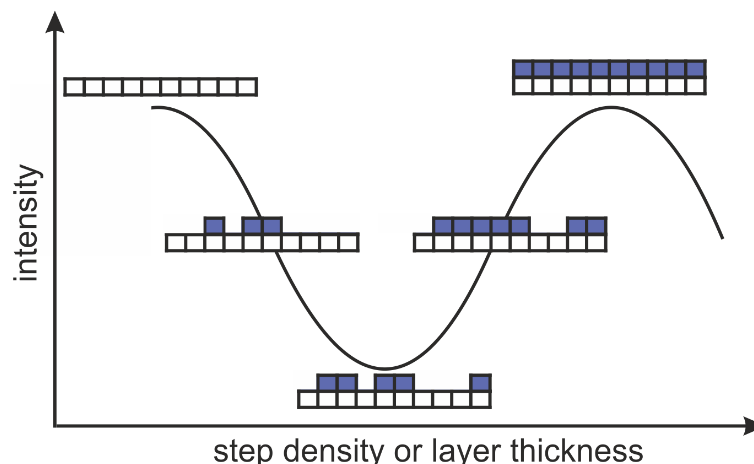

Figure 2.5: *Connection of surface coverage and RHEED oscillations: the intensity of diffuse scattering of the electron beam off the surface depends on the step density, which changes gradually during layer-by-layer growth. Maximum intensity corresponds to a fully closed layer.*

ML so that oscillations are damped. As a special case 2D, step-flow growth should be mentioned. Here, growth only takes place at step edges and thus the step density does not change. This results in a constant intensity of the RHEED spots.

Comparison to LEED

A closely related technique is low energy electron diffraction (LEED). In this case electrons with an energy between 10-500 eV are used to probe the sample surface. For these low energies the de Broglie wavelength is in the range of a few Ångströms. The beam is directed perpendicularly onto the surface and thus this technique cannot be applied during deposition. Electrons are detected by a phosphor screen in a backscattering geometry. This setup is perfectly suited to analyze crystalline symmetries and orientations, which is more complicated to observe in RHEED due to the geometrical setup. The enhanced surface sensitivity enables a detailed study of surface reconstructions. Furthermore, surface in-plane lattice parameters, which are derived in a similar fashion as in RHEED, can be obtained.

2.4 X-ray diffraction and reflectivity

Information on the 'bulk' structural properties of a sample can be obtained using x-ray diffraction (XRD) and x-ray reflectivity (XRR). For single crystalline samples and thin films the former method gives direct access to the bulk in- and out-of-plane lattice constants, the substrate-to-film orientation, epitaxial strain, and crystalline quality. From XRR measurements direct information on the film thickness, the surface roughness and the interface roughness are obtained. Contrasting XRD to RHEED, the mean free path

of photons is several orders of magnitude higher compared to electrons. Thus, measurements can be performed in ambient air. Furthermore, monochromizing x-rays is far more easily achieved, which allows the precise determination of the lattice constants.

Bragg's law

The scattering of x-rays off a periodic crystal is described by Bragg's law. Constructive interference is found for:

$$2 \cdot d_{hkl} \sin\theta = n\lambda, \tag{2.2}$$

where $n \cdot \lambda$ is a multiple of the x-ray wavelength. The angle θ is defined with respect to the surface of the crystal and d_{hkl} is the spacing of the lattice planes stacked along the $[hkl]$ direction, where h, k, l denote the Miller indices as sketched in Fig. 2.6. In a cubic

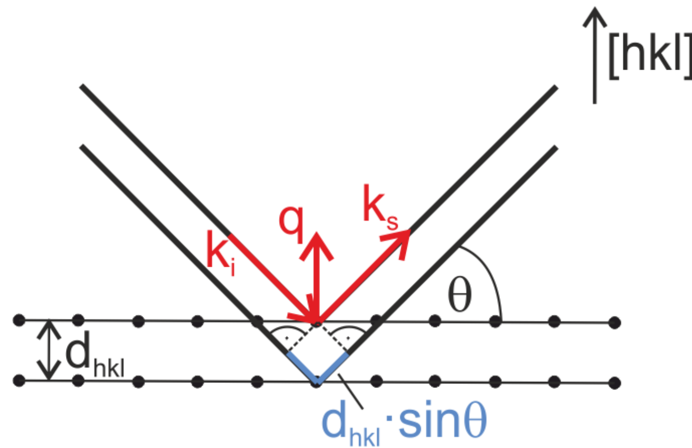

Figure 2.6: *Bragg scattering off a single crystal. The momentum transfer* $\mathbf{q}$ *is given by the difference of the scattered and the incident wavevectors* $\mathbf{k}_{i,s}$.

crystal their spacing is linked to the lattice constant a by

$$\frac{1}{d_{hkl}^2} = \frac{h^2 + k^2 + l^2}{a^2}. \tag{2.3}$$

In a simple diffraction experiment, a so-called θ-2θ scan, the incident angle of x-rays is changed simultaneously with the detection angle. This allows for a probing of the d_{hkl} planes perpendicular to the sample surface.

Theoretical description

One way of theoretically describing the interaction between x-rays and matter is to first consider the scattering of x-rays off a single electron and then to gradually expand this model to a crystalline solid [38]. The starting point is the Thomson formula that

describes the scattering of light off a single electron. Here it is assumed that the incident plane wave comes out as a spherical wave that is observed from a great distance from the scattering center. The amplitude of the wave A_{e^-} after the scattering process at the position $\mathbf{r}_e$ is given by

$$A_{e^-} = A_0 \frac{e^2}{mc^2} \frac{1}{R_0} \exp[i(\mathbf{k}_s - \mathbf{k}_i)\mathbf{r}_e], \tag{2.4}$$

where A_0 is the amplitude of the incident wave, R_0 is the distance to the observer and $\mathbf{k}_i$, $\mathbf{k}_s$ are the incident and scattered wavevectors, respectively.

By firstly summing over all electrons around an atom, taking their density distribution into account, secondly considering all atoms in a unit cell, and finally summing over all unit cells, the scattering amplitude is derived as follows:

$$A_{\text{cryst}} = A_0 \frac{e^2}{mc^2} \frac{1}{R_0} F(\mathbf{q}) \sum_{n_1=0}^{N_1-1} \sum_{n_2=0}^{N_2-1} \sum_{n_3=0}^{N_3-1} \exp[i\mathbf{q} \cdot \mathbf{R}_n]. \tag{2.5}$$

Here, N_1, N_2, N_3 denote the number of unit cells along the three crystal axes, which are given by $\mathbf{a}_1$, $\mathbf{a}_2$, and $\mathbf{a}_3$. The origin of each unit cell is given by $\mathbf{R}_n = n_1\mathbf{a}_1 + n_2\mathbf{a}_2 + n_3\mathbf{a}_3$. The momentum transfer $\mathbf{q}$ is defined by $\mathbf{k}_s - \mathbf{k}_i$. In the case of elastic scattering $|\mathbf{k}_s|=|\mathbf{k}_i|$, $\mathbf{q}$ is directly linked to the experimental scattering angle θ by $|\mathbf{q}|=2|\mathbf{k}_{i/s}|\sin\theta$ (see Fig. 2.6). $F(\mathbf{q})$ is the structure factor given by

$$F(\mathbf{q}) = \sum_{j=1}^{N_c} f_i(\mathbf{q}) \exp[i\mathbf{q} \cdot \mathbf{r}_j] \mathrm{d}^3 r, \tag{2.6}$$

where N_c is the number of atoms in one unit cell and $f_i(\mathbf{q})$ are the atomic scattering factors. $F(\mathbf{q})$ can be calculated for all Bravais lattices. Depending on the crystalline symmetry, the extinction of diffraction peaks or the resulting scattering intensity can be evaluated.

For a better understanding of how the scattered intensity would look like, we consider a one-dimensional crystal, disregarding the structure factors and all pre-factors of A_{cryst} for the moment. The intensity is proportional to the square modulus of

$$\left| \sum_{n_1=0}^{N_1-1} \exp[i\mathbf{q}_1\mathbf{R}_1] \right|^2 = \left| \sum_{n_1=0}^{N_1-1} \exp[i\mathbf{q}_1 n_1 \mathbf{a}_1] \right|^2 = \left| \frac{1-\exp[i\mathbf{q}_1\mathbf{a}_1 N_1]}{1-\exp[i\mathbf{q}_1\mathbf{a}_1]} \right|^2 = \left| \frac{\sin^2(N_1\mathbf{q}_1\mathbf{a}_1/2)}{\sin^2(\mathbf{q}_1\mathbf{a}_1/2)} \right|^2.$$

Due to its common use in optics, this function, which is plotted in Fig. 2.7, is called 'N-slit interference function'. The function is shown for N=10. For sufficiently big N, which is fulfilled for crystals, this function is sharply peaked for every $\mathbf{q}_1 = 2\pi m/\mathbf{a}_1$ with m being an integer number. Side maxima lose intensity with increasing N. Going

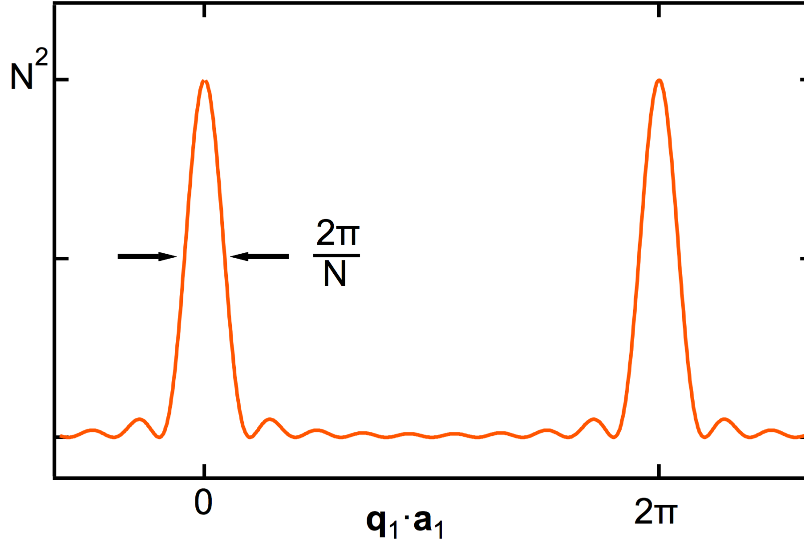

Figure 2.7: *1D-XRD pattern: N-slit interference function. The function exhibits maxima for every 2π in units of $\mathbf{q}_1\mathbf{a}_1$. The peak width scales inversely with N, which here is the number of unit cells.*

back to three dimensions a maximum in the scattering intensity can be found for all non-vanishing structure factors $\mathrm{F}(\mathbf{q})$ and

$$\begin{aligned}\mathbf{q}\cdot\mathbf{a_1} &= 2\pi h\\ \mathbf{q}\cdot\mathbf{a_2} &= 2\pi k\\ \mathbf{q}\cdot\mathbf{a_3} &= 2\pi l,\end{aligned} \tag{2.7}$$

where h, k, l are the Miller indices. These are the so-called Laue equations, which are equivalent to Bragg's law.

XRD measurements

In practice, the change of the momentum transfer $\mathbf{q}$ is realized by a change of the angle θ. Various scan modi, which are indicated in blue in Fig. 2.8 are possible. The figure shows the lattice points in reciprocal space in the upper part and the sample in the lower part. Note that only the black lattice points within the white area are accessible by the experiment. The lattice points outside the big circle cannot be reached as the momentum transfer is too small and limited by the wavelength of the x-ray source. The points within the small circles cannot be reached due to technical reasons of the XRD goniometer.

For a θ-2θ-scan the source and the detector are simultaneously moved with respect to the sample surface. This results in a momentum transfer $\mathbf{q}$ perpendicular to the sample surface, changing only the modulus of $\mathbf{q}$, i. e., the scan probes the Bragg spots in the

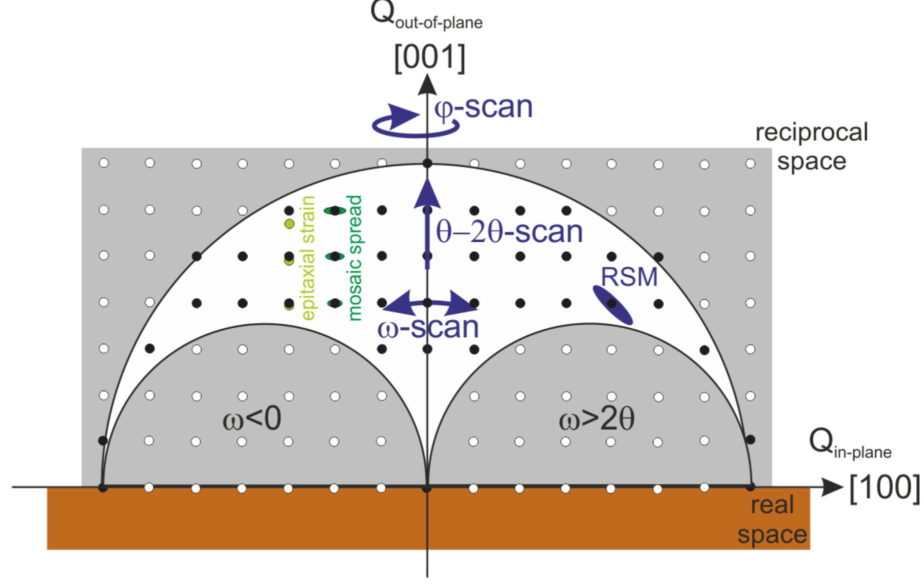

Figure 2.8: *Possible XRD scan modes: a θ-2θ-scan probes the Bragg peaks perpendicular to the sample surface; an ω-scan probes the width of a Bragg peak, which is determined by the mosaic spread of the film as indicated in dark green. Epitaxial strain can be analyzed by recording a so-called reciprocal space map (RSM), which is a 2D map of a Bragg peak. Epitaxial strain results in a shift of the Bragg peaks of the film with respect to the substrate in the out-of-plane direction as indicated in light green (adapted from [39]).*

[001] direction. From this, the lattice constant, or more precisely the spacing of the lattice planes perpendicular to **q**, are probed.

An ω-scan is carried out at constant positions of the source at θ and the detector at constant 2θ. By changing the angle of the sample with respect to the detector and the source, the length of **q** is kept constant, only changing its direction. This probes the width of the Bragg peaks, which is a direct measure for crystallinity and the mosaic spread of the sample. In the left part of Fig. 2.8, peak broadening due to mosaic spread is shown, which becomes stronger for higher-indexed Bragg peaks. Another scan mode is the recording of so-called reciprocal space maps (RSM). For this purpose, several ω-scans are taken at different θ-2θ positions of the source and the detector. In this way, a two-dimensional map of a Bragg peak is obtained. As it is most convenient to express these Bragg peaks in terms of the out-of-plane momentum transfer $Q_{\mathrm{out-of-plane}}$ and the in-plane momentum transfer $Q_{\mathrm{in-plane}}$, the following formulas are used to convert from ω and θ angles [39]:

$$\begin{aligned} Q_{\mathrm{out-of-plane}} &= 2|\mathbf{q}| \cdot \sin\theta \cdot \cos(\theta - \omega) \\ Q_{\mathrm{in-plane}} &= 2|\mathbf{q}| \cdot \sin\theta \cdot \sin(\theta - \omega). \end{aligned} \tag{2.8}$$

RSMs allow to analyze in-plane and out-of-plane strain effects in detail. To give an example, epitaxial strain of a film grown on a substrate with a small lattice mismatch

results in a conservation of the in-plane lattice constant, but in a change of the out-of-plane lattice constant. This is also sketched in the left part of Fig. 2.8. The light green dots indicate diffractions spots of a film with a slightly larger lattice constant. Although the in-plane lattice constant is the same for the film and the substrate and hence peaks are at the same $Q_{in-plane}$ values, differences in the out-of-plane component are observed. This can be only discriminated in the asymmetric Bragg peaks as a standard θ-2θ scan is only sensitive to the out-of-plane component.

Reflectivity of x-rays

Another useful property of x-rays is their reflection off sample surfaces and interfaces. The interference of these scattered beams leads to oscillations in the reflected intensity, so-called thickness fringes or Kiessig fringes [40]. Considering a film-on-substrate system, the position and period of these fringes can be directly related to the film thickness. The surface and interface roughness can be estimated by modelling the fringe pattern. These models can also be extended for multilayer systems.

For x-rays the refractive index is smaller than unity as most resonance frequencies of a solid lie below the frequency of x-rays. In general for x-rays, the refractive index of a material can be expressed as

$$n = 1 - \delta + i\beta, \tag{2.9}$$

where δ and β are given by

$$\delta = \frac{2\pi\rho_{el}r_0}{k^2}, \tag{2.10}$$

$$\beta = \frac{\mu}{2k}. \tag{2.11}$$

Here, ρ_{el} is the number density of the electrons, r_0 the Thomson scattering amplitude per electron, μ the absorption coefficient of the material and k the wavevector of the x-rays. Similar to the escape of visible light from an optically denser medium, like water to air, a critical angle α_c can be defined for the penetration of x-rays from vacuum to the material. This angle is given by

$$\alpha_c = \sqrt{\frac{4\pi\rho_{el}r_0}{k^2}} \tag{2.12}$$

and is in the order of one milli-radian. This relation is commonly used to determine the stoichiometry of a material [41].

The reflectivity of a system consisting of a film and a substrate is determined by single and multiple reflections at the two interfaces vacuum (v) to film (f) and film to substrate (s), and their separation d. This separation leads to a phase shift of the waves reflected off the interface between vacuum and film and the waves reflected off the interface between film and substrate. The amplitude of the reflectivity can be calculated by summing over

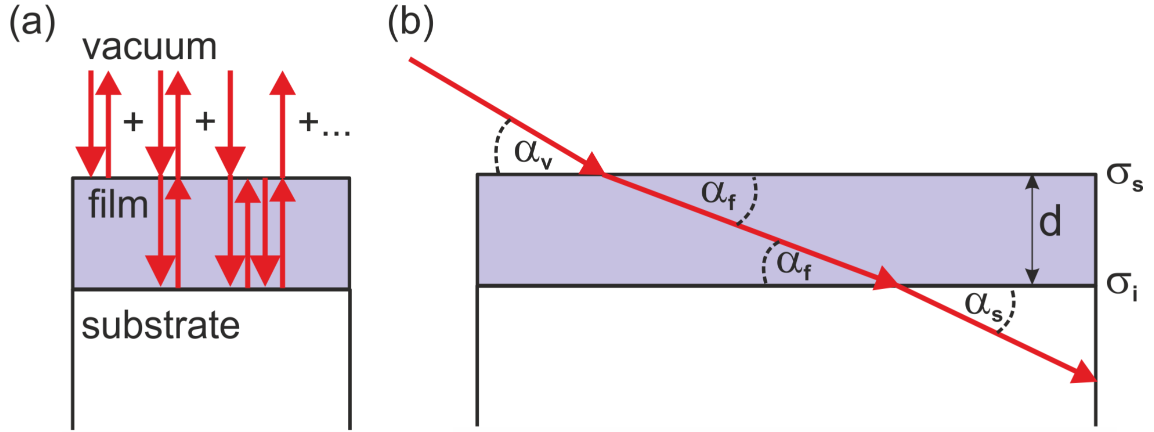

Figure 2.9: *X-ray reflection and transmission from a slab consisting of a film and a substrate. (a) The total reflectivity is the sum of the infinite number of reflections off the interfaces. (b) Refractions at the interfaces between vacuum and film and between film and substrate. The angle α_v of the incident x-rays determines the angles α_f in the film and α_s in the substrate according to Snell's law. The film thickness d as well as the surface roughness σ_s and the interface roughness σ_i can be obtained by modelling the total reflectivity (adapted from [41]).*

the infinite number of reflections at the interfaces as indicated in Fig. 2.9 (a). The total reflectivity of the x-rays can be expressed as follows:

$$R = |r^2| = \left| \frac{\tilde{r}_\mathrm{vf} + \tilde{r}_\mathrm{fs} p^2}{1 + \tilde{r}_\mathrm{vf} \tilde{r}_\mathrm{fs} p^2} \right|^2. \tag{2.13}$$

Here, p^2 is the phase factor. It depends on the angle α_f in the film and is directly related to the film thickness d:

$$p^2 = \exp[i2k \cdot \sin\alpha_\mathrm{f} \cdot d]. \tag{2.14}$$

$\tilde{r}_\mathrm{ij}$ are the Fresnel coefficients of the respective interfaces, accounting especially for the roughness $\sigma_\mathrm{s/i}$ of each interface as proposed by Névot and de Boer [42, 43]:

$$\tilde{r}_\mathrm{ij} = \frac{\sin\alpha_\mathrm{i} - \sin\alpha_\mathrm{j}}{\sin\alpha_\mathrm{i} + \sin\alpha_\mathrm{j}} \cdot \exp\left[\frac{-k^2\sigma_\mathrm{s/i}^2 \sin\alpha_\mathrm{i} \sin\alpha_\mathrm{j}}{2}\right]. \tag{2.15}$$

In practice, reflectivity is measured for small x-ray incident angles in a standard θ-2θ measurement geometry. The film thickness is derived by measuring the angular positions θ_m and θ_n of the interference maxima m and n of the Kiessig fringes, which can be directly derived from Eq. 2.13 and 2.14:

$$d = \frac{(m-n)\lambda}{2 \cdot (\sin\theta_m - \sin\theta_n)}. \tag{2.16}$$

2.5 Photoelectron spectroscopy

Valuable information on the electronic and chemical properties of a sample can be obtained from photoelectron spectroscopy (PES). This technique has to be performed in UHV to ensure a high enough mean free path of both photoelectrons and photons. Furthermore, clean sample surfaces are desirable as the probing depth is only a few nm. The valence sensitivity of PES bares information on the chemical surroundings of an atom and its chemical state, i. e., the oxidation state. Furthermore, quantitative spectra analysis yields the stoichiometric composition of the samples. Non-destructive depth profiling can be performed by tuning the surface-sensitivity. A great advantage especially for the analysis of thin film properties is that small amounts of material can be probed in contrast to other techniques like x-ray diffraction.

Another huge application field is angle-resolved PES (ARPES). This technique can be used to analyze the dispersion relation of valence band electrons and will be touched only briefly in the following as it is not subject of this work.

Basic principle

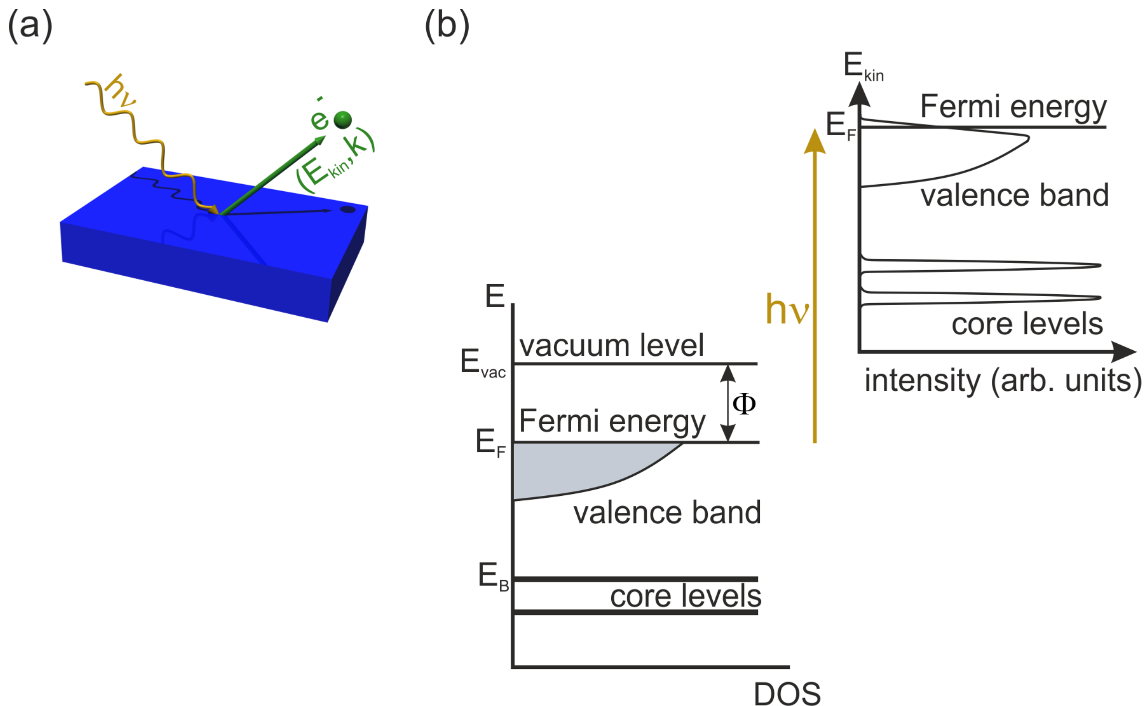

Figure 2.10: *(a) Schematics of the photoemission process. Due to the photoelectric effect electrons are generated within the sample by incident photons and emitted into the vacuum off the sample surface. (b) Mapping of the electronic structure of a solid in a photoemission experiment. The kinetic energy of the photoelectrons is directly related to their binding energy in the solid.*

The schematic drawing in Fig. 2.10 (a) illustrates the basic principle of PES. Monochromatic photons with an energy $h\nu$ are directed on a sample. Within the sample photoelectrons are generated due to the photoelectric effect [44]. These photoelectrons can leave the sample and can be analyzed in terms of their kinetic energy, momentum and spin orientation.

Einstein's equation describes the energy conservation of this process and relates the kinetic energy of the photoelectron E_{kin} to its binding energy E_b in the solid [45]:

$$E_{kin} = h\nu - E_b - \Phi. \tag{2.17}$$

Here, $h\nu$ is the energy of the photon, while Φ represents the work function which is defined as the difference between the chemical potential μ and the vacuum level (see Fig. 2.10 (b)). The figure shows the connection of the energetics in a solid, namely the electronic structure and the photoemission spectrum, where the electrons are discriminated according to their kinetic energy. The photoemission spectrum directly reflects the density of occupied states (DOS) in a solid. The core-levels in the solid are assumed to have a sharp energy. In the photoemission spectrum they are broadened, exhibiting a Voigt lineshape which results from the convolution of a Lorentzian and a Gaussian lineshape. The latter reflects the broadening due to the finite energy resolution of the measurement system, whereas the former accounts for the finite lifetime of the core-hole. The valence band shape strongly depends on the density of states and is thus material-specific. Metallic samples exhibit a Fermi cut-off at the chemical potential $\mu(\hat{=}\mathrm{E}_F)$, which is formed by the occupied states with the lowest binding energy. The photoemission spectrum of a real solid, however, can be more complicated, as the photoelectrons are emitted from a system with a large number of interacting electrons.

The information that can be obtained from a photoemission spectrum depends among others on the utilized photon energy. Using low energies in the ultra-violet range, loosely defined between 10-100 eV, the valence band region and shallow core-levels are probed. In this energy range the momentum transfer between the photon and the electron can be neglected. In the emission process the parallel component of the photoelectrons' momentum $\mathbf{k}$ is conserved. This gives access to the momentum-energy dispersion $E(\mathbf{k})$ of the valence band region and thus makes ARPES a powerful tool to map the band structure and Fermi surface of materials [46]. Using higher energies (100 to 1500 eV) one gets access to core-levels with higher binding energies. The energetic position of these core-levels is not only element-specific, but also depends on the chemical surrounding of the atoms, resulting for instance in an energy shift (chemical shift) of an oxidized species with respect to a pristine one. This is exploited in so-called electron spectroscopy for chemical analysis (ESCA) [47]. Using photons up to an energy of 10 keV in hard x-ray photoemission spectroscopy (HAXPES), the bulk sensitivity is increased, which enables depth profiling and the analysis of buried interface layers [48].

Theoretical description

To describe the features in a photoemission spectrum on a more theoretical level, Fermi's golden rule can be taken as a good starting point [46, 49, 50]. It describes the light field as a first order perturbation of a system with N electrons and gives a transition rate of

$$w_{f,i}(h\nu) = \frac{2\pi}{\hbar}|\langle\Psi_f^N|H_{int}|\Psi_i^N\rangle|^2 \cdot \delta(E_f^N - E_i^N - h\nu) \tag{2.18}$$

between the initial state $|\Psi_i^N\rangle$ and the final state $|\Psi_f^N\rangle$. The latter is composed of a photoelectron with an energy $E_{\mathbf{k}}$=$(\hbar^2k^2)/2m$ and the momentum $\hbar\mathbf{k}$, and the remaining $(N-1)$ electron system. The δ-function fixes the energy conservation. The first order perturbation Hamilton operator is given by

$$H_{int} = \frac{e}{2mc}(\mathbf{A}\cdot\mathbf{p} + \mathbf{p}\cdot\mathbf{A}) \approx \frac{e}{2mc}\mathbf{A}\cdot\mathbf{p}. \tag{2.19}$$

Within the latter formulation, the commutator relation $[\mathbf{p},\mathbf{A}]$=-$i\hbar\nabla\cdot\mathbf{A}$ and the dipole approximation was used. This approximation is applicable, if $\mathbf{A}$ is constant over interatomic distances and thus $\nabla\cdot\mathbf{A}$=0. To describe now the photocurrent $J(h\nu)$ produced by this process one has to sum over all possible final states s, which then include also phonons, plasmons, electron-hole pairs and multiple excitations:

$$J(h\nu) = \frac{2\pi}{\hbar}\sum_s |\langle\Psi_{f,s}^N|H^{int}|\Psi_i^N\rangle|^2\delta(E_f^N - E_i^N - h\nu). \tag{2.20}$$

Within the 'sudden approximation' it is assumed that (i) the excitation of the photoelectron happens instantaneously, (ii) the kinetic energy of the photoelectron is high enough to leave the solid and (iii) interactions with the solid can be neglected. Thus, a final state $|\Psi_f^N\rangle$ can be factorized by

$$|\Psi_f^N\rangle = c_{\mathbf{k}}^\dagger|\Psi_f^{N-1}\rangle, \tag{2.21}$$

with $c_{\mathbf{k}}^\dagger$ being the creation operator of the photoelectron with the quantum number $\mathbf{k}$ and $|\Psi_f^{N-1}\rangle$ being the $(N-1)$ final state. The photocurrent may now be re-formulated assuming the initial state being the ground state $|\Psi_0^N\rangle$ of the system

$$J(\mathbf{k}, h\nu) = \frac{2\pi}{\hbar}\sum_j |M_{\mathbf{k}j}|^2 \cdot \sum_s |\langle\Psi_{f,s}^{N-1}|c_j|\Psi_0^N\rangle|^2 \cdot \delta(E_{\mathbf{k}} + E_{f,s}^{N-1} - E_0^N - h\nu) \tag{2.22}$$

$$= \frac{2\pi}{\hbar}\sum_j |M_{\mathbf{k}j}|^2 \cdot A_j^<(\epsilon_{\mathbf{k}} - h\nu) \tag{2.23}$$

with $|M_{\mathbf{k}j}|^2$ being the one-particle dipole transition matrix element and $A_j^<$ the one-electron spectral function.

The transition matrix element depends on the element, the atomic subshell and the photon energy. For core-levels these dependencies can be seen in the photoionization cross-section. Typically, so-called asymmetry parameters connected to the experimental geometry are used to parametrize its behavior [51–53]. The spectral function is by definition connected to Green's function which contains the complex self-energy. This includes contributions from many-body processes like electron-electron and electron-phonon interactions. In Eq. 2.22, the energetic positions of single transitions are fixed by the δ-functions. $|\langle\Psi_{f,s}^{N-1}|c_j|\Psi_0^N\rangle|^2$ is the probability that the (N-1) electron system is in the excited state s after the photoemission process. For uncorrelated systems with one distinct final state s this results in one line at $E_{\mathbf{k}}$. In general, one has to sum over all possible final states and thus several lines can appear in the photoemission spectrum. An example of this is the multiplet splitting of the V 2p core-level in $LaVO_3/SrTiO_3$ (see Sec. 5.5.1).

From surface to bulk sensitivity - HAXPES depth profiling

The limiting factor of the probing depth in PES is not the penetration depth of the photons, but the inelastic mean free path of the photoelectrons (λ). As the electrons interact strongly with the solid, the probability of a scattering event is enhanced for electrons that escape from deeper layers of the solid. Thus, the photoemission signal is strongly damped and the probing depth is restricted to the first few nm of the material. However, λ depends on the kinetic energy of the photoelectrons and can be enhanced up to ~10 nm using hard x-rays, which allows for bulk sensitive measurements and the analysis of buried interfaces.

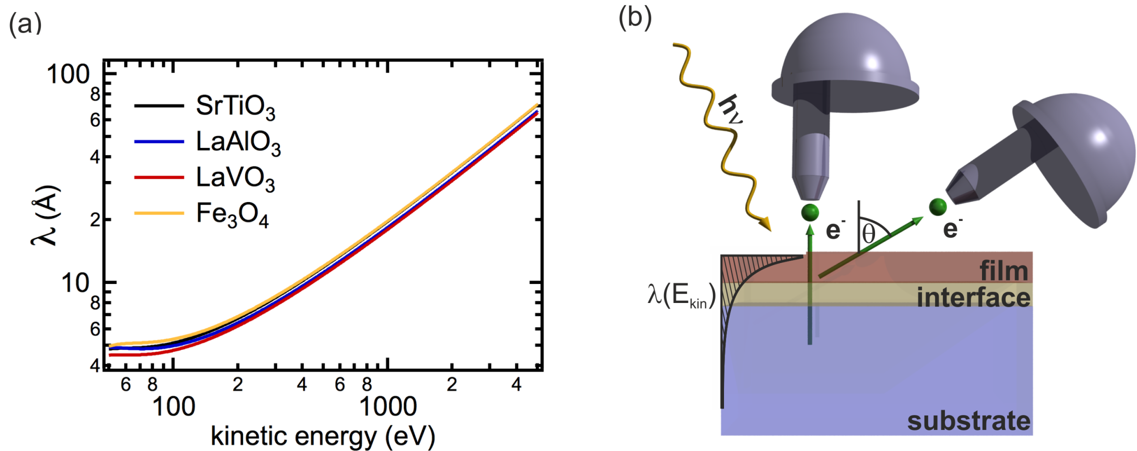

Figure 2.11: *(a) Inelastic mean free path (λ) of photoelectrons calculated according to Eq. 2.24. λ increases with higher kinetic energies resulting in an increased bulk sensitivity. (b) Schematics of HAX-PES depth profiling. By changing the photon energy and/or the detection angle θ of the photoelectrons, λ_{eff} can be tuned to probe the vertical composition of a sample.*

The dependence of λ on the kinetic energy of the photoelectrons is shown in Fig. 2.11 (a). While λ is about 5-10Å when conventional Al K_α is used as an excitation source, it increases up to 40-50Å for electrons excited by hard x-rays. Although this curve is often referred to as 'universal', i. e., material independent, differences between materials are in the percentage region. The predictive 'TPP-2M' equation, which is named after S. Tanuma, C. J. Powell and D. R. Penn, can be used for a proper material-dependent determination of λ. It is given as a function of the kinetic energy E_{kin} by [54]

$$\lambda(E_{kin}[eV]) = \frac{E_{kin}}{E_p^2(\beta \ln(\gamma E_{kin}) - (C/E_{kin}) + (D/E_{kin}^2))} \quad [\text{Å}]. \tag{2.24}$$

Here, E_p is the plasmon energy and β, γ, C and D specify material-dependent properties like density, atomic weight, number of valence electrons per atom and band-gap energy. Essentially, this equation was developed and tested for energies from 50 eV to 2 keV, but it seems to be suitable for energies up to 30 keV [54]. λ was calculated for each material system and utilized photon energy relevant within this thesis.

Besides tuning the photon energy, varying the detection angle represents a second possibility to change the effective mean free path of the photoelectrons:

$$\lambda_{\text{eff}} = \lambda(E_{kin}) \cdot \cos\theta \tag{2.25}$$

The detection angle θ is measured with respect to the surface normal as indicated in Fig. 2.11 (b). In general, the overall information depth is defined by $3{\cdot}\lambda_{\text{eff}}$ as about 95% of the measured signal emerge from this region of the sample. Thus, by choosing a high enough photon energy, the substrate, the interface and the film layer can be probed. The schematic picture of Fig. 2.11 (b) also illustrates the non-destructive depth profiling of a hybrid structure. Note that for substrate core-levels high photon energies and small detection angles give the highest (substrate) bulk sensitivity, whereas low photon energies and high detection angles provide the highest (substrate) interface sensitivity. In contrast, for a film core-level, the highest (film) interface sensitivity is achieved for high photon energies and low detection angles, whereas low photon energies and high detection angles are most (film) surface sensitive.

Valenceband offsets and band bending in heterostructures

Photoemission can also give insight into the band alignment and a possible band bending at surfaces and interfaces of heterostructures [56–59]. Thus, a band diagram can be derived. Band bending, which in other words is a gradual energetic shift of the bands towards, e. g., an interface, is also reflected by the core-levels. Here, band bending results in an asymmetric broadening, assuming the probing depth being larger than the spatial extension of the band bending. If this is not the case, a shift of the core-levels may be observed. One fingerprint of this effect is its presence at all core-levels of the material. For instance, a band bending in STO will show up at both Ti and Sr

core-levels. Furthermore, a quantification can be attempted by simulating the core-level spectra using reference data of materials that do not exhibit this effect.

The valence band offset in heterostructures can be determined using the method proposed by Kraut *et al.* and Chambers *et al.* Accordingly, the valence band offset $\Delta E_{\mathrm{vb}}^{\mathrm{AB}}$ in a heterostructure AB is given by [60, 61]:

$$\Delta E_{\mathrm{vb}}^{\mathrm{AB}} = (E_{\mathrm{cl}}^{\mathrm{A}} - E_{\mathrm{vb}}^{\mathrm{A}}) - (E_{\mathrm{cl}}^{\mathrm{B}} - E_{\mathrm{vb}}^{\mathrm{B}}) - \Delta E_{\mathrm{cl}}^{\mathrm{AB}} \tag{2.26}$$

with $\Delta E_{\mathrm{cl}}^{\mathrm{AB}} = (E_{\mathrm{cl}}^{\mathrm{A}} - E_{\mathrm{cl}}^{\mathrm{B}})^{\mathrm{AB}}$. This method relies on the availability and the precise measurements of reference samples of the respective materials A and B.

However, for the thin films under investigation in this thesis, HAXPES offers a second possibility. Assuming the probing depth is larger than the film thickness, the valence band spectrum is composed of substrate and film. Thus, by deconvolving the data using reference spectra and taking the respective damping into account, the valence band offset can be measured directly. One problem, however, is the precise determination of the energetic position of the valence band, which is not as easily defined as in the case of a core-level. Chambers *et al.* proposed the so-called 'linear method' to determine the onset of the valence band. In this method the position of the valence band is defined by its onset, which in turn is determined by the intersection of a linear fit to the leading edge of the valence band and the background signal at the lower binding energy side of a spectrum.

Although this method has been successfully applied for semiconductor heterostructures, care has to be taken when interpreting the data, as charging effects as well as surface and interface photovoltage effects may distort the measurements, especially for materials with large band gaps [62–64].

3 Fe_3O_4/ZnO – growth of a possible spin electrode

Abstract

Fe_3O_4/ZnO heterojunctions are prominent candidates for spin injection devices. Both constituents exhibit sufficiently high spin coherence lengths. The oxidic character of ZnO makes it preferable in contrast to other semiconductors for a combination with Fe_3O_4. In this study, the influence of the oxygen partial pressure on the iron oxide phase formation was analyzed. Furthermore, a comparison of samples grown by PLD and MBE showed that both methods can be used to grow high-quality heterostructures, when an adequate oxygen background pressure is applied. A pressure variation during growth minimized a FeO-like interface layer improving the interface quality. Structural properties were found to be almost identical. For the samples grown by PLD hints for the Verwey transition were observed. Independent of the growth method, all samples exhibited a reduced magnetic moment most probably due to the formation of anti-phase boundaries caused by an island-like growth mode.

3.1 Heterostructures for spin injection

The ongoing miniaturization and the dire need for higher computing powers require the development of new concepts in semiconductor physics. Apart from the exploration of new materials to develop faster conventional devices, also new effects have been exploited for data storage and processing. Usually, only the charge degree of freedom is used to process data in a CPU, while data storage is done magnetically on a hard drive. New concepts, for example, involve both the charge degree of freedom and the spin degree of freedom, which in general enable data storage and processing in one device and may pave the way for feasible quantum computing. Spin polarization, however, is usually not a property of a semiconductor. The realization of so-called spintronic (spin-electronic) devices, such as spin transistors or spin valves, strongly depends on the availability of materials that combine both ferromagnetic and semiconducting properties [65]. Beside the incorporation of magnetic impurities into a semiconducting host in so-called diluted magnetic semiconductors, the controlled injection of a spin-polarized current into a semiconductor using ferromagnet-semiconductor heterojunctions is a promising approach [66, 67].

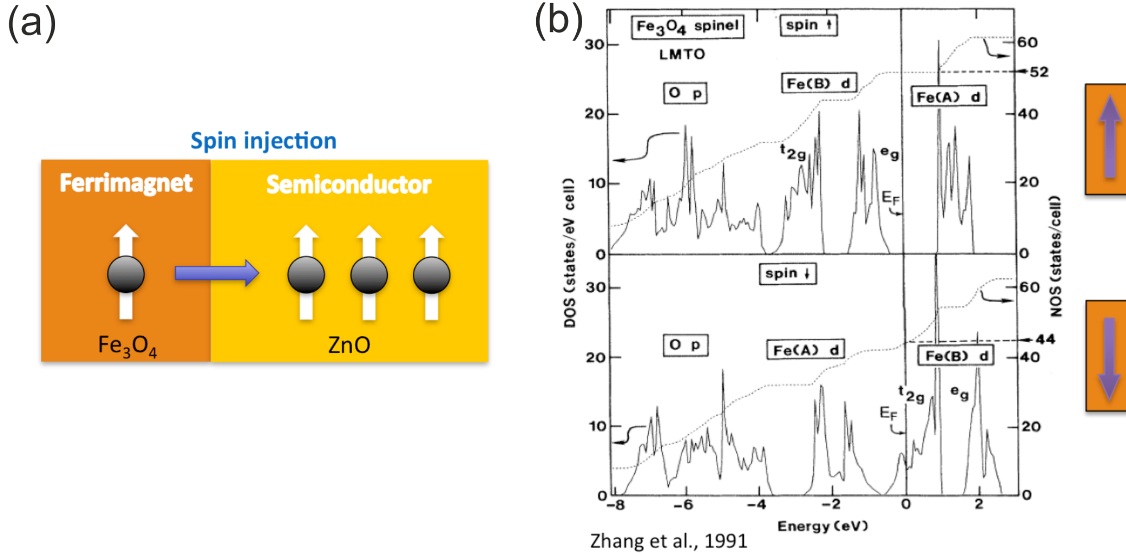

Figure 3.1: *(a) Schematics of a spin injection device. A spin-polarized current is injected from a magnetic material into a semiconductor. (b) Calculated density of states near the Fermi-level for Fe_3O_4 exhibiting a -100% polarization [68].*

The basic concept of the latter approach is illustrated in Fig. 3.1 (a). Here, a spin-polarized current is generated in the ferro-/ferrimagnetic material and injected into a conventional semiconductor. Applications in this field are, e. g., spin-polarized light-emitting diodes and lasers [69, 70]. A possible material system that would suit this purpose especially well is the hybrid system of magnetite (Fe_3O_4) and zinc oxide (ZnO).

Although ZnO is not ranked among the most common semiconductors, it is currently attracting much attention for its application in transparent opto-electronics, since it exhibits a wide direct band gap (E_{gap}=3.37 eV) and provides the possibility of n- or p-doping [71, 72]. Possible applications are UV light emitters, spin-functional devices and transparent electronics, but also the combination with wide band gap materials such as AlInGaN are discussed [14]. Long spin coherence lengths, which are also preserved at room temperature, make this material suitable for spin transport [73]. As far as interfacial stability with Fe_3O_4 is concerned, the oxidic character of ZnO is one of the crucial advantages compared to Si or GaAs.

Magnetite is a material that has been known for a long time as one of the magnetic materials existing in the earth's crust. Here, it is of special use for birds as they use magnetic sensors for orienting. First technological relevance was gained when Fe_3O_4 was used for data storage and magnetic tape recording. In spintronics, Fe_3O_4 has attracted interest as spin-aligning material, as it stands out with a theoretical -100 % spin polarization at the Fermi energy. The density of states, which is plotted in Fig. 3.1 (b), exhibits a band gap for the spin-up channel of about 0.5 eV at the Fermi-level. In contrast, the spin-down states cross E_F, which causes the half-metallic, ferrimagnetic properties. The

density-functional theory calculations were done by Zhang *et al.* using local spin-density approximation [68]. The ferrimagnetism is conserved up to a Curie temperature as high as T_C=858 K. This is a major advantage compared to other spin-polarized materials like EuO or GaMnAs, since room temperature devices seem to be feasible [74–78]. However, depending on the crystal quality and surface orientation, experiments show a spin polarization between -55 % and -80 % only [12, 13]. A further property of Fe_3O_4 that should be mentioned is the Verwey transition at T_V=120 K [79]. Besides a structural transition, a drop of the conductivity by two orders of magnitude and a change in the magnetic properties as well as in the heat capacitance is observed. Although the origin of this transition has not yet been fully understood, electron correlation effects have been discussed as a possible origin of the phase transition [80]. Since already for small off-stoichiometries the transition temperature drops or vanishes completely. it can be used as a sign for crystal/film quality [81].

Turning back to spintronic devices, there are some basic requirements for ferromagnet-semiconductor heterostructures that need to be met. In addition to a maximum spin polarization in the ferromagnet, the impedance mismatch of both materials must be as small as possible to accomplish efficient spin injection [82]. The electrical conductivity of Fe_3O_4 at room temperature is about $2.5{\cdot}10^{-4}\,(\Omega\mathrm{cm})^{-1}$ and thus reasonably well within the required range for spin injection into a semiconductor [83]. Spin scattering lengths will be sensitive to the intrinsic properties of each compound, to the device geometry, and to the crystalline quality of the heterostructure [69]. For bulk Fe_3O_4, the spin diffusion length is reported to be as high as 100 nm [84, 85]. However, extrinsic factors such as homogeneous film formation strongly depend on growth parameters like temperature, background pressure, and lattice mismatch. The interface sharpness and chemical quality are of special interest. A frequently encountered problem is the formation of unwanted phases near the interface such as Fe or FeO, when Fe_3O_4 is grown on GaAs or Al_2O_3, respectively [86, 87]. Furthermore, the properties of thin films can vary dramatically in comparison to those of the bulk (e. g., through the formation of a magnetically dead interface layer or strain effects). For devices, single phase formation and interface properties are most important and thus will be focused upon.

3.2 Physical properties and thin film growth

Models of the crystal structure of both ZnO and Fe_3O_4 are displayed in Fig. 3.2. ZnO crystallizes in the hexagonal wurtzite structure with lattice constants of $a_{\mathrm{ZnO}} = 3.25$ Å and $c_{\mathrm{ZnO}} = 5.206$ Å (Fig. 3.2 (a)). Schematically it can be described as alternating planes of fourfold-coordinated O^{2-} and Zn^{2+} ions, stacked along the *c*-axis with alternating distances of 0.69 Å and 1.99 Å, respectively. Cutting the crystal perpendicularly to the *c*-axis always creates a Zn-terminated (0001) surface on one side of the crystal and an O-terminated $(000\bar{1})$ surface on the other side. A further consequence of the polarity is an unavoidable reconstruction of the surface [88].

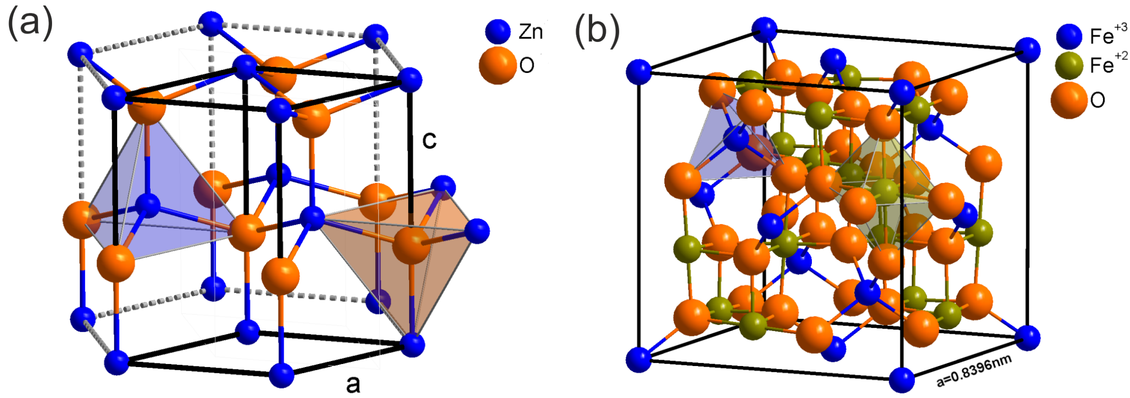

Figure 3.2: *(a) Hexagonal lattice structure of ZnO. (b) Inverse spinel structure of Fe_3O_4, space group Fd3m.*

Fe_3O_4 exhibits a cubic inverse spinel structure (Fig. 3.2 (b)) with a lattice constant of $a_{Fe_3O_4}$=8.3941 Å above the Verwey transition. The slightly distorted face-centred unit cell contains 32 oxygen anions, 8 Fe^{2+} and 16 Fe^{3+} cations. Half the Fe^{3+} cations, so-called *A*-sites, reside on eight of the 64 available tetrahedral interstices of the oxygen lattice. The remaining Fe cations (*B*-sites) occupy 16 of the 32 octahedral interstices. The ferrimagnetic behavior results from anti-ferromagnetic coupling of the spins in the *A*-site and *B*-site Fe sublattices. Theoretical and experimental analyses derive a net magnetization of 4.0 μ_B per formula unit [68, 89]. However, usually this value is reduced due to temperature effects and off-stoichiometry [81, 89]. The mixed-valent *B*-sites (Fe^{2+}/Fe^{3+}) couple via double exchange across the oxygen anions. This allows a delocalization of the electrons and results in the comparably high conductivity of Fe_3O_4 compared to other oxides. For the growth on the hexagonal ZnO surface, the Fe_3O_4 (111) surface with a surface lattice constant of 5.92 Å is crucial as it exhibits hexagonal symmetry [90]. Nevertheless, the lattice mismatch of -8.6 % with respect to a doubled ZnO surface lattice constant is still large.

Growing magnetite was attempted on various substrates by different methods [91–96]. Magnetic tunnel junctions were realized using the band insulator MgO as a substrate [78, 97]. The very low lattice mismatch of only -0.32 % makes it a perfect model and reference system for thin film characterization [98–100]. For direct spin injection into a semiconductor Fe_3O_4 films were grown on Si, GaAs or InAs [92, 101–104]. However, interface chemistry seems to be quite complicated. There are reports of a dead layer formed by the oxides of the semiconductor material being accompanied by a reduction of the magnetite film [86]. Growth and detailed characterization of films on ZnO are rare. Nielsen *et al.* reported on PLD grown films on ZnO and showed epitaxial growth by means of XRD. Furthermore, magnetic measurements give an indication for the Verwey transition [105]. Li *et al.* measured the spin polarization of sputtered Fe_3O_4/ZnO/*c*-Al_2O_3 and determined this to be 28.5 % using four probe transport measurements [106].

Nearly independent of the growth method, the key parameter to accomplish Fe_3O_4 growth is the precise dosing of oxygen during or after growth. Besides Fe_3O_4, other iron oxide phases exist, like the purely divalent FeO and the purely trivalent Fe_2O_3. Since Fe_3O_4 is a mixed-valent phase, the growth window is narrowed dramatically. While PLD requires a certain background pressure to run the process properly, MBE can be done (at least in theory) under perfect ultra-high vacuum conditions. In this case, pure iron thin films can be grown on substrates, followed by post-oxidation at the appropriate temperatures and oxygen partial pressures. This procedure is favored if substrate oxidation has to be avoided. For growth on ZnO, reactive growth *in* an oxygen atmosphere is preferred. The desired oxidation is already achieved during growth and a more uniform film is expected. Furthermore, oxygen vacancies in the substrate, caused by reduction during heating in vacuum or by oxygen diffusion from substrate to film, are avoided [107]. In the literature, various *forms* of oxygen have been applied. Alongside molecular oxygen, atomic oxygen or NO_2 has been used due to an elevated reactivity [108–110]. The main advantage of molecular oxygen is that it is cheap and easily applicable. Furthermore, Chambers *et al.* pointed out that the oxidation potential of O_2 should be sufficiently high to form Fe_3O_4 [111].

3.3 Identification of different iron oxides by means of XPS

A suitable tool to distinguish the iron oxides is XPS, because it is particularly sensitive to the valence state of an element. The similarities of the iron oxides in lattice constant and structure make a detailed phase characterization quite challenging. Most structural methods like XRD, which probes the lattice structure, fail for an unambiguous determination of the iron oxide phase and can only be used to provide additional information. XPS studies of iron oxides were carried out by Brundle *et al.* and McIntyre *et al.* in the late 1970s [112, 113]. They both find the satellite structure of the Fe $2p$ core-level being highly sensitive to the iron valence state, although minor effects also depend on the surface preparation of the iron oxide single crystal. In contrast, the binding energy of the O $1s$ core-level remains unaffected for all of these compounds and can thus be used as energy reference for the photoemission spectra. More recently, Yamashita *et al.* did a quantitative XPS study to deconvolve the Fe^{2+} and Fe^{3+} parts in the different iron oxides [114].

For a qualitative analysis of the iron oxide thin films, XPS reference spectra of FeO, Fe_3O_4, and Fe_2O_3 single crystals were recorded within the present thesis. The Fe $2p$ core-level of the corresponding crystals are shown in Fig. 3.3. Single crystals were filed *in situ* and spectra were taken using a monochromated Al K_α source. For all materials, the most pronounced peaks of the spectra arise from the spin-orbit split Fe $2p_{3/2}$ and Fe $2p_{1/2}$ core-levels at binding energies of about 710-712 eV and 723-725 eV, respectively.

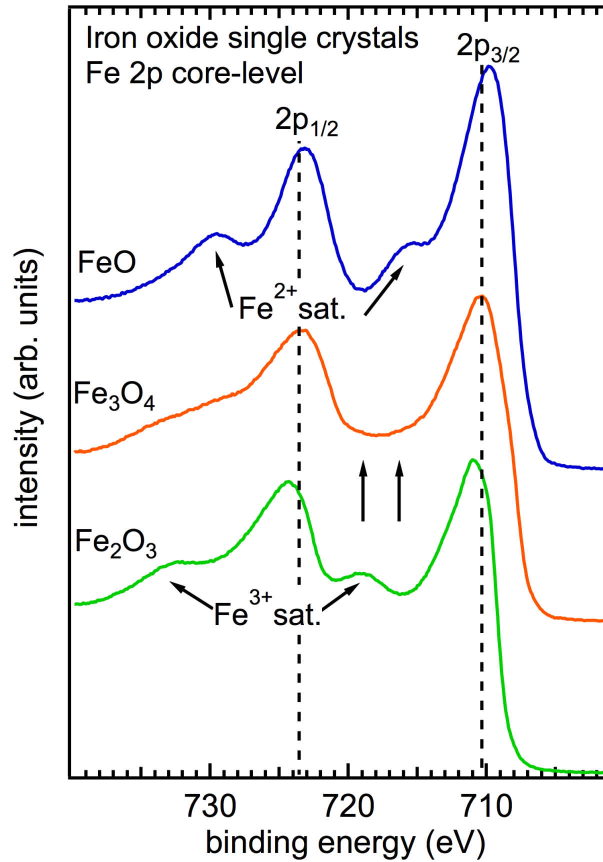

Figure 3.3: *XPS Fe 2p core-level spectra of different iron oxide single crystals taken as reference for thin film characterization. The spectra strongly differ in their satellite structure as indicated by the arrows.*

In all cases the peaks are broadened, resulting from multiplet splitting. Despite this broadening a small shift of these peaks is visible among the different iron oxides, i. e., the Fe $2p_{3/2}$ peak is located at a binding energy of 709.7 eV for FeO and for Fe_2O_3 it is at 710.9 eV. Besides this small difference, the spectra clearly differ in the satellite structure present at the higher binding energy side of the respective spin-split peak. These charge transfer satellites, which are labelled by the arrows in Fig. 3.3, originate from a charge transfer between the Fe $3d$ shell and an oxygen ligand's shell L with the transfer energy depending on the ligand field. For example in the case of the FeO single crystals, the Fe^{2+} satellites occur at 715.6 eV and 729.5 eV, whereas in the case of Fe_2O_3, the satellites are shifted to 719.2 eV and 732.7 eV. For the mixed valence of Fe_3O_4, the Fe^{2+}:Fe^{3+} ratio of 1:2 leads to a virtually identical intensity of these satellites, which in turn results in the smeared-out, nearly feature-free region between the main peaks. The relative chemical shift of 1.2 eV of the main Fe $2p_{3/2}$ peak, which is due to the different Fe valences 2+ and 3+, is visible in the FeO and Fe_2O_3 spectra and results in a shoulder at the lower

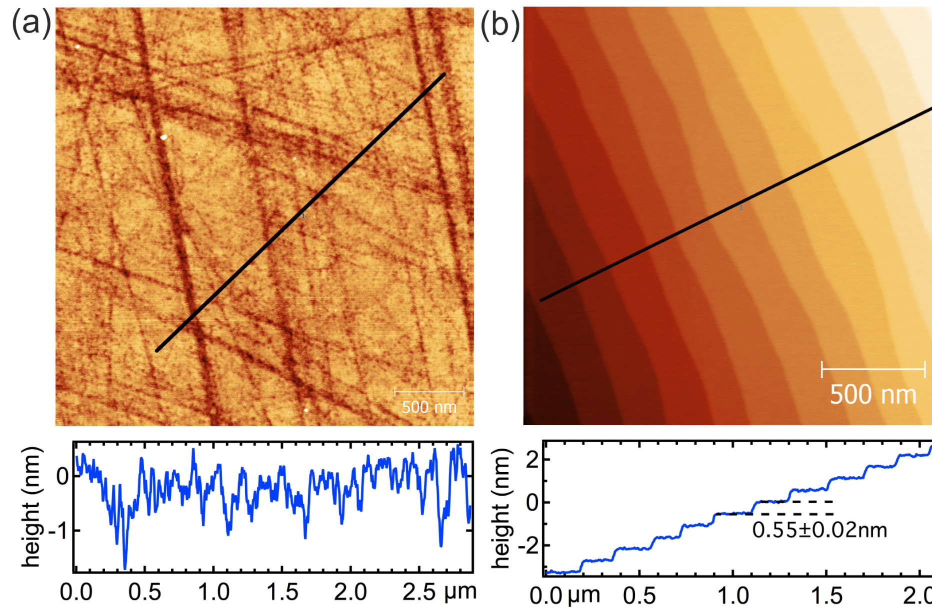

Figure 3.4: *AFM images of ZnO substrates with respective height profiles: (a) as-received and (b) after cleaning with organic solvents and annealing in oxygen atmosphere at 1000 °C. After this treatment flat terraces with a step height of about 1 uc are observed.*

binding energy side of Fe_3O_4. Based on its absolute position and its relative shift with respect to the main line, this shoulder can be clearly attributed to Fe^{2+}, whereas the main peak corresponds to Fe^{3+}. All these findings are in accordance with the literature [112–115].

3.4 Surface preparation of ZnO substrates

For all films, commercially available substrates were used (Crystec or Mateck, Germany). However, as-received substrates had to be prepared for the growth of Fe_3O_4. Two different approaches were chosen for surface preparation; both included cleaning *ex situ* with organic solvents. The first method encompasses several cycles of *in situ* ion-etching (Ar^+, 1 kV) and annealing up to 700 °C. Finally, the substrates were annealed at 400 °C in an oxygen partial pressure of $5 \cdot 10^{-7}$ mbar for 15 min. In this case, quality was checked *in situ* by LEED and XPS. The second method is based on reports in the literature [116, 117]. Substrates were annealed *ex situ* for 5 h at a temperature of 1000 °C under oxygen flow in a furnace. This results in atomically flat substrate surfaces. *In situ* the substrates were heated for a short period of time before film growth to temperatures of about 290 °C to dissolve remaining carbon contaminations.

Atomic force microscopy (AFM) is capable of imaging the morphology of a surface *ex situ*. Images of ZnO substrates before and after annealing (method 2) are shown in Fig. 3.4 (a) and (b), respectively. The as-received substrates exhibit trenches up to

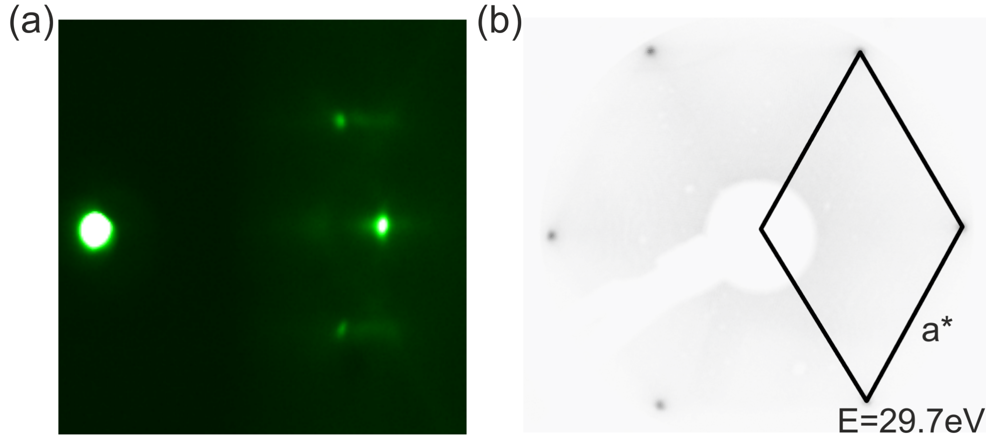

Figure 3.5: *(a) RHEED and (b) LEED images of treated ZnO substrates indicating a well-ordered 2D surface. The hexagonal reciprocal unit cell is sketched in (b). From this the surface lattice constant is derived to be a=(3.3±0.2) Å.*

1 nm deep and a rms roughness of (0.39±0.05) nm, while after annealing the substrates are perfectly flat showing steps that correspond to the miscut of the sample and a rms roughness of (0.14±0.05) nm. Analyzing the height profile shown in Fig. 3.4 (b) in more detail, an average step height of (0.55±0.02) nm is derived. This corresponds to the c-axis lattice constant of ZnO, which means that the substrate is mono-atomically flat.

A typical RHEED pattern of the substrate is shown in Fig. 3.5 (a). On the left side, the primary beam of the electron gun can be observed. On the right side, three spots are visible: the specular (0,0) main spot and the two side spots corresponding to the (0,1) and the $(0,\bar{1})$ reflections. This pattern is characteristic of a two-dimensional surface. The slight elongations of the spots in the horizontal direction result from the energy spread of the primary electrons. For comparison, the LEED pattern of a ZnO substrate, which was prepared using method 1, is shown in Fig. 3.5 (b). The image is taken at an electron energy of E=29.7 eV. Additionally, the reciprocal surface unit cell is sketched. Similar patterns could be obtained over a wide energy range. Although ZnO is a wide band gap semiconductor, charging effects were only visible at very small energies, hinting at a minor oxygen deficiency or some impurities in the bulk. The pattern exhibits a six-fold symmetry with sharp main spots and a low background intensity. This, together with the absence of additional spots, indicates a clean (1x1) surface with a low defect density and a little surface roughness. A lattice constant of a=(3.3±0.2) Å was derived, which corresponds very well to literature values for the unreconstructed ZnO surface lattice constant [14]. On the basis of the RHEED and LEED pattern analyses both methods seem to be suitable for the preparation of clean ZnO surfaces.

3.5 Influence of the oxygen partial pressure on the iron oxide formation during PLD growth

All films analyzed in this section were grown by PLD in the MESA+ laboratory at the University of Twente. As commercially available target materials, Fe_2O_3 and pure Fe were used. Attempts were made to synthesize a Fe_3O_4 target on the basis of reports by Chinnasamy *et al.* and Wang *et al.* [118, 119]. However, this was not accomplished successfully as the last step of the production involves sintering the material, which led to a full oxidation to Fe_2O_3. If this last step is not carried out, the density of the pellet is too low to use it as a PLD target. Both the sintered and the commercial Fe_2O_3 target contained too much oxygen. Although the PLD process always causes a loss of oxygen from the target during deposition, even deposition in an inert background gas (Ar) resulted in the growth of Fe_2O_3 [32]. Therefore, the metallic Fe target was used for the films grown by PLD, even though the use of metal targets involves drawbacks like low ablation rates and splashing effects [32]. To counteract the low ablation rate, a fluency of $4\,\mathrm{J/cm^2}$ and a laser repetition rate of 2 Hz was chosen. The substrate temperature was set to 390 °C and controlled via a thermocouple. The oxygen partial pressure was varied between $1.1\cdot 10^{-6}$ mbar and $8.7\cdot 10^{-5}$ mbar. The growth parameters are given in Tab. 3.1. Note that for samples C and D a certain pressure variation during growth was applied, i. e., for the first minute the pressure was set to $2.4\cdot 10^{-5}$ mbar and reduced to $9.5\cdot 10^{-6}$ mbar for the remaining growth time. This will be explained in more detail in Sec. 3.7.

Table 3.1: *Iron oxide films prepared in different oxygen partial pressures. Roughness, surface lattice constant and relative spectral weight derived by AFM, RHEED and XPS, respectively.*

	pressure [mbar]	deposition time [min]	roughness [nm] (AFM)	a_{film} [nm] (RHEED)	Fe 2p/Zn 2p (XPS)
sample A	$1.1\cdot 10^{-6}$	4	0.7±0.1	2.9±0.1	5.2
sample B	$5.6\cdot 10^{-6}$	5.5	0.8±0.1	3.1±0.1	2.0
sample C	$(2.5\cdot 10^{-5}$–	1+	1.1±0.1	5.9±0.1	5.1
	$9.5\cdot 10^{-6})$	3			
sample D	$(3.3\cdot 10^{-5}$–	1+	0.8±0.1	6.0±0.1	—
	$9.8\cdot 10^{-6})$	20			
sample E	$8.7\cdot 10^{-5}$	4	0.4±0.1	6.2±0.1	4.7

The AFM images together with a corresponding height profile as well as RHEED images taken *in situ* after growth are shown in Fig. 3.6. RHEED oscillations could not be found for any growth pressure. This is a direct indication that growth is not

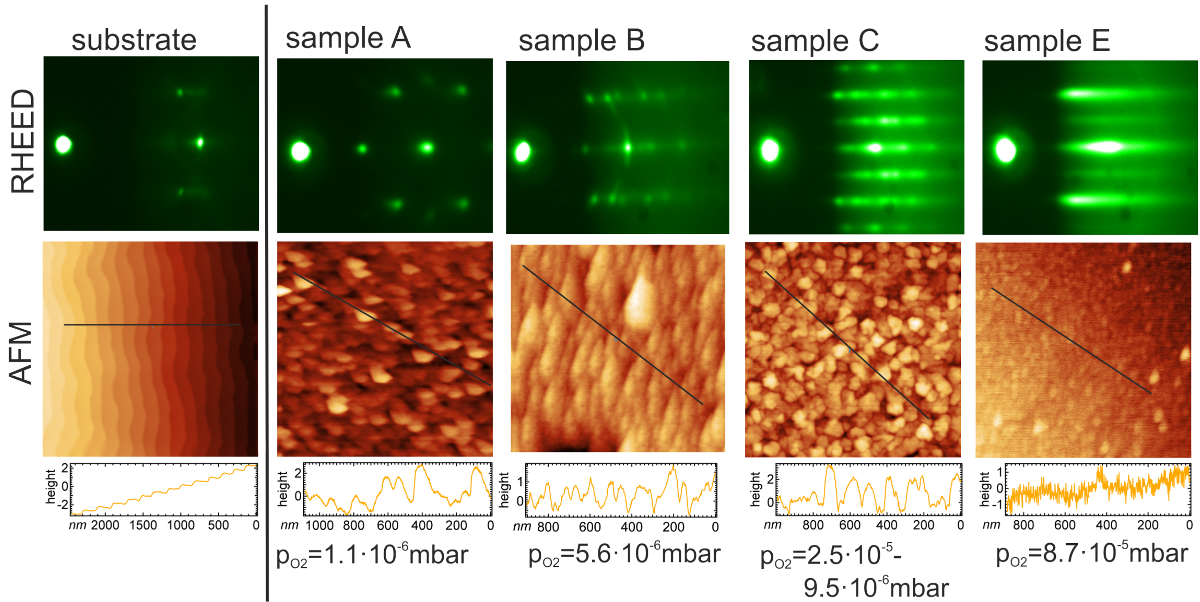

Figure 3.6: *In situ RHEED pattern and AFM images with corresponding height profiles of the ZnO substrate and the iron oxide films grown by PLD. Surface roughness as well as island size and island shape strongly depend on the oxygen partial pressure.*

layer by layer. Nevertheless, RHEED patterns could be obtained permanently during and after growth indicating crystalline growth. Starting for all growth pressures with a 2D RHEED pattern shown on the left side (substrate), all films show more or less 3D-like growth, which is most pronounced at low growth pressures for samples A and B. For these two films new transmission spots appear resulting from 3D diffraction in bulk crystallites. For sample C there are also spots visible, but the pattern is more streaky compared to samples A and B. In the case of the highest growth pressure, the pattern is completely streaky (sample E). For samples D and E, new spots appear on the Laue circle for instance between the substrate (0,0) and (0,1) spot. This can directly be interpreted as a doubling of the lattice unit cell. The lattice constant of the film can be calculated by measuring the shift of the spots with respect to the distance of the (0,0) and for instance the (0,1) spot of the ZnO substrate. The calculated values are listed in Tab. 3.1. For samples A and B, the lattice constant is smaller compared to the substrate and falls within the range of the bulk values of either pure Fe (a=2.87 Å) or FeO (a_{111}=3.0 Å) [120]. This gives a first indication for a metallic or a divalent Fe phase formation. For samples C and E, the lattice constant is smaller, if compared to the double substrate lattice constant, and is comparable to the values of bulk Fe_3O_4 or Fe_2O_3. The AFM images confirm the 3D growth of the iron oxide thin films. Both the line profile in Fig. 3.6 and the rms roughness given in Tab. 3.1 indicate that the surface of sample E is the flattest, while the other samples exhibit a higher surface roughness. Although island growth is most pronounced for sample C, the crystallites exhibit sharp

edges that are regularly aligned. This could be caused by some registry given by the substrate and it could also explain why the RHEED pattern is more streaky compared to sample B, which in contrast is smoother in AFM.

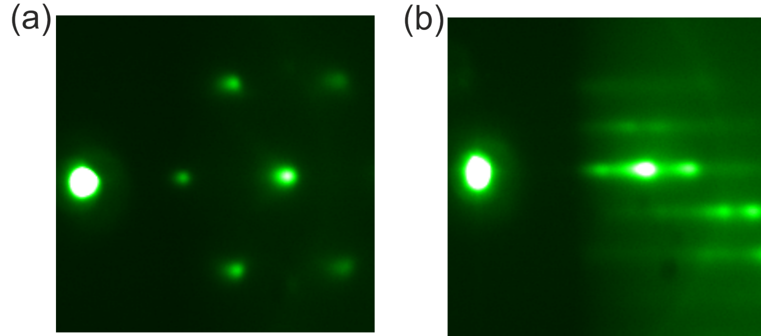

Figure 3.7: *Film-to-substrate registry analyzed in an off-axis RHEED geometry for (a) sample A (p_{O_2}=1.1$\cdot$ 10^{-6} mbar) and (b) sample C (p_{O_2}=3.3$\cdot$ 10^{-5}-9.8$\cdot$ 10^{-6} mbar). The latter shows a strong dependence on the in-plane orientation of the incident electron beam.*

Further indication for film registry can be found when the RHEED beam is tilted out of the high symmetry direction of the substrate. For 2D film growth, but also for oriented islands, this results in a change of the pattern. This is due to the 'rocking' of the Ewald sphere with respect to the reciprocal lattice rods. For randomly orientated crystallites or 3D transmission spots, no changes are observed in the pattern. This is the case for samples A and B, as shown in Fig. 3.7 (a) exemplarily of sample A for an azimuthal tilt of 5°. In contrast, as far as samples C and E are concerned, the pattern changes with respect to the azimuthal angle as shown in Fig. 3.7 (b).

The XPS (*in situ*, Al K_α) Fe $2p$ core-level spectra are shown in Fig. 3.8. For all spectra the O $1s$ core-level at 530.1 eV was used as an energy reference, as the binding energy for this particular core-level is the same in all iron oxides and well documented in the literature [121]. Clear differences are found in those spectra when compared to the single crystal spectra in Fig. 3.3. Sample A shows, in combination with the FeO-like peak structure, two additional peaks exhibiting a narrow line width at a binding energy of about 706.8 and 720.1 eV. The peaks can be identified as the Fe $2p$ core-levels of pure iron [86, 122], which means that sample A is a combination of FeO and Fe. By increasing the oxygen growth pressure, the iron oxide state can be tuned, starting with purely divalent for sample B to purely trivalent for sample E. Both sample C and sample D, which differ in film thickness, show the characteristic line shape of Fe_3O_4. To give a rough estimate of the ablated material, the intensity ratio of the Zn $2p$ and Fe $2p$ core-levels was calculated and is listed in Tab. 3.1. Note that these values are no absolute measure of the deposited material and can only give a relative ratio for this growth series. Apparently, for all samples, except for sample B, the deposited material is in the same range. For sample B, the ratio is reduced, which may be caused by some misalignment during deposition. Apart from this, sticking and nucleation rates seem to

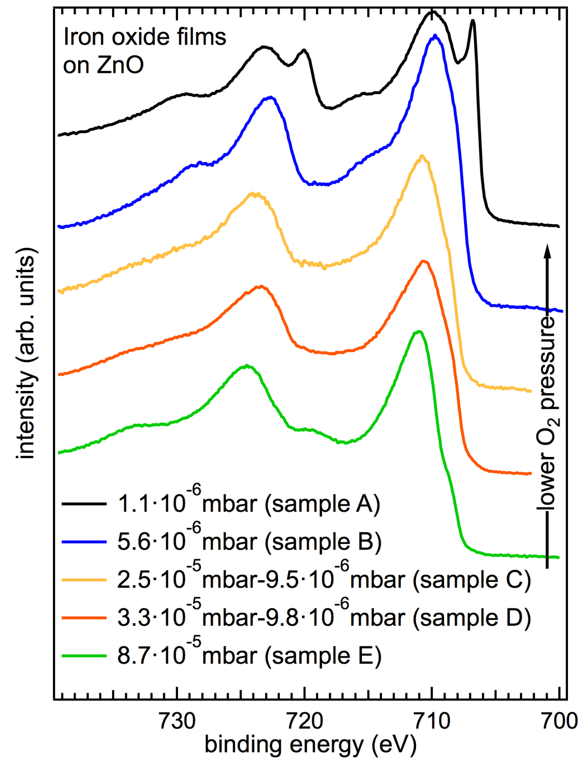

Figure 3.8: *In situ XPS Fe 2p spectra of the iron oxide films prepared at different O_2 pressures. The oxidation state of iron increases with increasing oxygen growth pressure, clearly identified by the charge transfer satellites (cf. Fig. 3.3).*

be independent of the iron oxidation state and the applied background pressure.

From this study it has become evident that PLD can be used to grow Fe_3O_4 films on ZnO substrates by choosing the appropriate oxygen partial pressure. This is in line with Nielsen *et al.* [105]. Most probably due to the high lattice mismatch, films grow in an island-like growth mode, with some in-plane orientation.

3.6 Comparison of Fe_3O_4 films grown by PLD and MBE

This section deals with a comparative study of Fe_3O_4 films grown by PLD at the University of Twente and by reactive oxygen MBE in Würzburg. Film quality and film properties will be compared for the growth on MgO and ZnO substrates. Additionally, the results will be contrasted to findings of M. Paul, who studied Fe_3O_4/ZnO films grown by MBE in Würzburg and at the University of British Columbia [123].

For the films grown on ZnO by PLD, the same growth settings were used as described in Sec. 3.5 (cf. samples C, D). In the case of films grown on MgO substrates, the oxygen

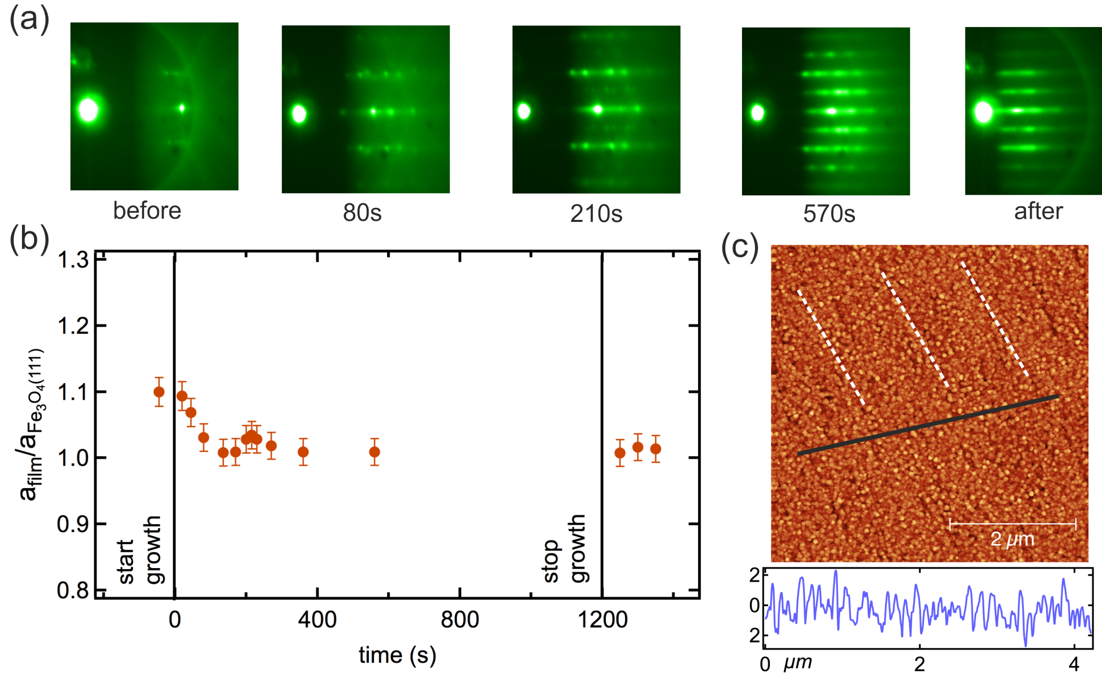

Figure 3.9: *(a) Development of the RHEED pattern during growth of Fe_3O_4 films as a function of growth time. (b) Development of the surface lattice constant with respect to the growth time points to a nearly fully relaxed surface after growth. (c) The AFM image taken on a 19 nm film exhibits an island height of about 2 nm only, indicating the coalescing of the islands.*

partial pressure was set to $1.0{\cdot}10^{-6}$ mbar, leaving all other parameters unchanged.

For the films grown by MBE, the growth temperature was set to 310 °C, which was monitored *ex situ* by a pyrometer. A certain pressure variation was applied for MBE growth, as was also the case for PLD. The oxygen pressure was kept at $5{\cdot}10^{-6}$ mbar for 10 min and reduced to $1{\cdot}10^{-6}$ mbar for the remaining growth duration of 30 min. For details see Sec. 3.7. All films were cooled down to room temperature without any oxygen dosing. In the case of MgO, no pressure variation was applied and an oxygen partial pressure of $2.5{\cdot}10^{-5}$ mbar was used. As RHEED was not available in the MBE setup, LEED was used to structurally characterize films *in situ* after growth.

3.6.1 Structure and morphology

RHEED and AFM

RHEED and AFM studies were carried out for Fe_3O_4 films grown by PLD (sample D). As already pointed out in Sec. 3.5, RHEED oscillations could not be observed at any growth pressure, suggesting an island-like growth mode. However, diffraction spots were visible throughout the entire growth time denoting epitaxial growth. Thus, RHEED images taken during growth were used to characterize the growth mechanism. These images

are shown in Fig. 3.9 (a), starting from the 2D substrate RHEED pattern on the left to the streaky film pattern on the right. Note that after growth the RHEED geometry was optimized, which resulted in a lower distance between the primary spot and the reciprocal diffraction pattern. During the first 100 s one can observe the appearance of new spots in [1,0] direction, but no new spots appeared in [0,1] direction. This points at the formation of islands. As no unit cell doubling is present during this first period, the layer may have a Fe-type or, more likely, a FeO-type character, which is more favorable due to a smaller lattice mismatch of -5.6 %. After about 200 s, which corresponds to a film thickness of about 2 nm (calculated from XRR analysis, see Sec. 3.6.1), new (0,1/2), $(0,\overline{1/2})$ Laue spots appear in the vertical direction indicating unit cell doubling, which is characteristic of the iron oxide spinel structure. For increasing growth times, the 3D-like pattern seems to smooth out and end in a streaky, almost 2D-like pattern after growth. This hints at a growth mode, where first crystalline islands oriented with respect to the substrate start to form. Later on, these islands coalesce, leading to a smoother surface and resulting in the streaky pattern after growth.

In Fig. 3.9 (b) the in-plane lattice constant derived from RHEED analyses is shown. Starting at the bulk lattice constant of ZnO, i. e., $1.1 \cdot a_{111}$, where a_{111} is the fully relaxed surface lattice constant of Fe_3O_4, it relaxes within the first 100 s to roughly the bulk value of the Fe_3O_4. This corresponds to the time interval, in which the additional spots occur, indicating the unit cell doubling. This gradual relaxation towards the bulk lattice constant suggests a gradual strain relaxation most probably due to the formation of vacancies and crystalline imperfections. However, registry to the substrate is preserved. A thickness of about 2 nm, at which the lattice constant seems to be nearly relaxed, is in line with findings for MBE grown films by M. Paul and the theoretical prediction within the model of Fischer *et al.* [31, 123]. In this model, strain relaxation in metastable heteroepitaxial semiconductor structures are calculated including the elastic interaction between straight misfit dislocations. The properties of this strained interlayer can be quite different from those of the bulk film.

The hypothesis of coalescing islands is manifested by the AFM image shown in Fig. 3.9 (c). The film thickness of 19 nm derived from XRR is higher compared to the average island height of about 2 nm. Also the surface roughness is smaller for thicker Fe_3O_4 films (see Tab. 3.1). Both findings support the coalescence of the islands formed in the initial growth state. Furthermore, one can still see some fingerprints of the substrate which causes a certain orientation of the islands, visible as trenches going from the upper left to the lower right corner of the image and corresponding to the substrate steps (indicated by the white lines in the images). A zoom in the image reveals the same oriented islands as were observed for sample C (see Fig. 3.6). Weiss *et al.* found similar regularly oriented islands for Fe_3O_4 films on Pt(111). Both the values for the surface roughness and the observation of oriented islands were also observed for films grown by MBE [123].

LEED

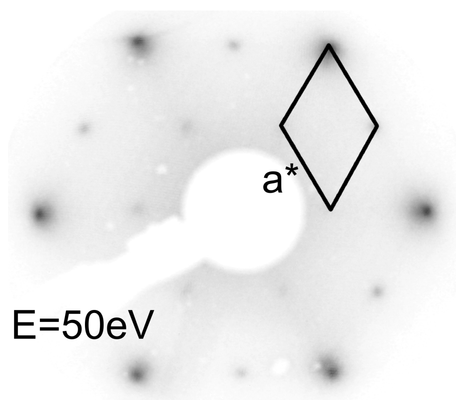

Figure 3.10: *LEED pattern of a Fe_3O_4 thin film taken at E=50.7 eV. The pattern exhibits a hexagonal symmetry which implies growth in [111] direction. No surface reconstructions are observed and the sharp spots as well as a low background intensity hint at a high crystalline quality.*

A LEED pattern of a MBE grown Fe_3O_4 film on ZnO (sample G) is shown in Fig. 3.10. In comparison to the substrate LEED pattern shown in Fig. 3.5 (b), new spots appear that are less intense. Similarly to RHEED, this suggests the doubling of the unit cell, which is only present for the spinel structures of Fe_3O_4 and Fe_2O_3, but not for FeO or ZnO. The hexagonal symmetry indicates epitaxial growth in [111] direction. As a guide to the eye the reciprocal unit cell is sketched in the pattern. The variation in spot intensity, which was not present in the substrate pattern, is commonly ascribed to the unreconstructed $Fe_3O_4(111)$ surface [124, 125]. Indeed, the lattice constant a can be determined to be (5.96±0.2) Å. This compares well to values found in the literature for the (111) surface, indicating a nearly fully relaxed film surface which is not pseudomorphically strained to the ZnO(000$\bar{1}$) surface and which is in line with the RHEED analyses of the PLD grown films (see Sec. 3.6). The low background intensity and comparably sharp spots that can be obtained all over the sample indicate epitaxial growth and atomic long range order. Furthermore, no evidence for reconstructions was found for the Fe_3O_4 films on ZnO [99, 100].

XRR and XRD

X-ray reflectivity and x-ray diffraction measurements were carried out at the University of Twente using a Bruker D8 Discover diffractometer. This was equipped with a monochromated Cu K_α source (λ=1.541 nm) and an optional 1D detector for recording reciprocal space maps. XRR and XRD are suitable tools to probe the structural properties of the 'bulk' film. From these measurements information on the out-of-plane and in-plane lattice constants as well as the layer thicknesses and roughnesses can be derived.

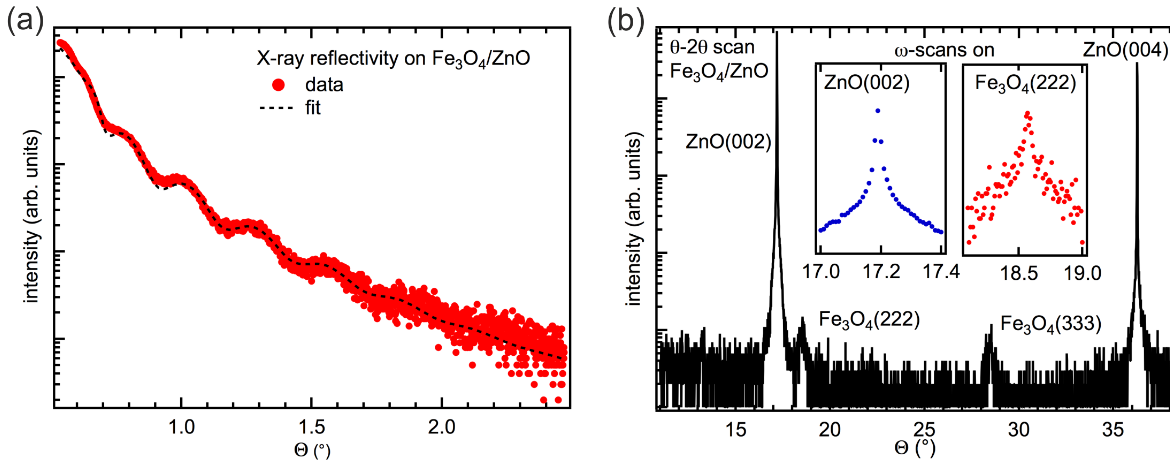

Figure 3.11: *(a) XRR of a Fe_3O_4/ZnO film. From a fit to the data, film thickness, surface and interface roughness are derived and listed in Tab. 3.2. (b) Wide-range θ-2θ XRD scan exhibits only ZnO(00n) and Fe_3O_4(lll) peaks in the out-of-plane direction. The inset shows the ω-scans (rocking curve) of the ZnO(002) and Fe_3O_4(222) reflections.*

The XRR scan of the range between about 0.05° and 2.50° is displayed in panel (a) of Fig. 3.11 (sample I). Additionally, a fit curve generated by a standard x-ray reflectivity fit routine is shown. The software *Bocfit* produces a least square fit to the data, using the electron densities as given parameters for both film and substrate and varying the layer thickness, interface and surface roughness to fit the data. The numbers derived are listed in Tab. 3.2 for samples D, I and F, the latter sample was grown on MgO. Note that sample I was grown without pressure variation during growth. The values of the surface roughness are within the same range comparing the AFM and XRR data and are determined by the average size of the partially coalesced crystallites. Compared with the roughness of the ZnO substrate, which is very low for annealed substrates (0.1-0.5 nm), the interface roughness is tremendously enhanced for the grown films. The film on MgO exhibits a lower interface, but a higher surface roughness. Note that MgO substrates can be prepared in a quality comparable to ZnO [126]. When magnetite is grown on MgO at moderate temperatures to avoid a $MgFe_2O_4$ layer, the formation of a strained FeO-like layer is not observed and comparable values for the interface roughness as for the films on MgO derived in this thesis are obtained [127, 128]. The increased surface roughness may be related to the large film thickness and a possible change in growth mode for such films. The increased interface roughness in the case of the films grown on ZnO could be related to the 2 nm thick interlayer that exhibits a higher degree of disorder as the strain relaxation causes lattice defects. Controversially, the fit quality could not be enhanced by introducing a third layer into the model representing this strained interlayer, which is due to only slight differences in the optical properties of the iron oxides [123]. M. Paul did XRR fits for slightly thicker Fe_3O_4/ZnO films grown by MBE and calculated interface roughness values. These are slightly smaller, but a

comparable surface roughness was found, indicating that the growth mode of coalesced islands is at play for both growth methods. Interfacial properties are slightly better for MBE grown films, which is probably caused by the different growth kinetics of PLD and MBE.

Table 3.2: *Thickness, interface and surface roughness of Fe_3O_4 films on ZnO and MgO derived by XRR. For the films on ZnO, surface roughness was also measured by AFM.*

	Fe_3O_4/ZnO		Fe_3O_4/MgO
	sample D	sample I	sample F
thickness [nm]	20.5±0.5	29.7±0.5	56.4±0.5
interface roughness [nm]	1.3±0.3	1.8±0.3	0.5±0.3
surface roughness [nm]	0.5±0.3	0.9±0.3	1.8±0.3
surface roughness (AFM) [nm]	0.8±0.2	1.0±0.2	—

In Fig. 3.11 (b), a θ-2θ wide-range scan is shown for the 29.7 nm thick film (sample I). The two main peaks at 17.19° and 36.26° originate from the substrate Zn0(002) and ZnO(004) Bragg reflections, respectively. In between, two smaller peaks can be observed at angles of about 18.56° and 28.52°. These peaks, which are much weaker in intensity and broadened compared to the main substrate peaks, can be attributed to the Fe_3O_4(222) and Fe_3O_4(333) film peaks. This confirms the growth of magnetite in the (111) direction as no other peaks are observed in this scan which is sensitive only to the out-of-plane direction. A more detailed analysis of a high-resolution scan of the Fe_3O_4(222) peak of sample D revealed an out-of-plane strain of -0.36±0.05 %. This compressive strain is in line with a slight tensile strain of the in-plane component of 0.6±0.5 % derived by the RHEED analysis of this film.

In the insets of Fig. 3.11 (b), ω-scans on the ZnO(002) and Fe_3O_4(222) peaks are displayed. The widths of these so-called rocking curves depend on the mosaic spread of crystalline materials. High-purity single crystalline substrates, for instance, exhibit a lower line width compared to grown films with crystalline imperfections. The full width at half maximum (FWHM) of the fitted Gauss peak is 0.01° for the substrate and 0.13° for the film peak. The former is in a range which is commonly observed for high-quality substrates [117]. For the film FWHM, M. Paul found slightly larger values for MBE grown films, while Nielsen *et al.* found even smaller values for films grown by PLD [105, 123].

More detailed information on the in- and out-of-plane strain components can be gained from the reciprocal space maps shown in Fig. 3.12. These are representations of the asymmetric ω-2θ-scans as functions of $Q_{in-plane}$ and $Q_{out-of-plane}$ reciprocal lattice components of the respective Bragg reflections. For this sample (sample I), scans were taken for both the (840) and the (951) peak at φ-angles of 30°, 90°, and 150° and for the (844) peak at φ-angles of 0°, 60°, and 120°. The appearance of these asymmetric Bragg

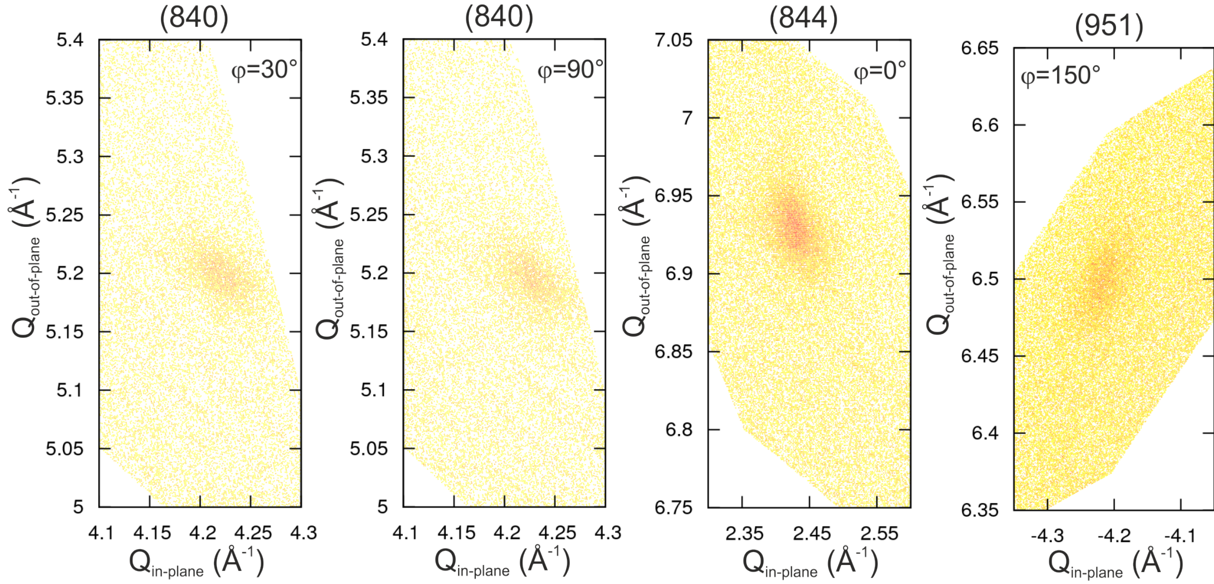

Figure 3.12: *Reciprocal space maps of the (840), (844), and (915) Fe_3O_4 Bragg peaks measured for different φ-angles for Fe_3O_4 on ZnO confirm in-plane registry and epitaxial growth. The lattice strain given in Tab. 3.3 was derived using these Bragg peaks.*

peaks at distinct φ-angles gives another indication for an in-plane orientation of the film, or more precisely, for the initially growing islands. The average values of the in- and out-of-plane strain derived from all peaks at different φ-angles are listed in Tab. 3.3. For the Fe_3O_4/ZnO films, strain values are rather small and the film is nearly completely relaxed. The values are in the same range for the Fe_3O_4/MgO films. Here, the lattice mismatch to the substrate is only -0.32% and hence film growth can be expected to be nearly relaxed with slight compressive out-of-plane strain. This is supported by the RSM data for MgO. Moreover, the data of the films on ZnO supports the findings by RHEED of a nearly relaxed growth for film thicknesses >2 nm. Nevertheless, slight distortions can be observed, which are most probably due to the remaining registry to the substrate.

Table 3.3: *In-plane and out-of-plane strain calculated from asymmetric Bragg peaks. Only marginal strain effects are found in the Fe_3O_4 films.*

	Fe_3O_4/ZnO		Fe_3O_4/MgO
	sample D	sample I	sample F
$\text{strain}_{\text{out-of-plane}}$ [%]	-0.32±0.02	-0.20±0.02	-0.17±0.02
$\text{strain}_{\text{in-plane}}$ [%]	0.38±0.02	0.37±0.02	0.31±0.02
$\text{strain}_{\text{volume}}$ [%]	0.4±0.1	0.5±0.1	0.4±0.1

In summary, the RHEED and LEED analyses show crystalline film growth with comparable qualities for films grown using MBE and PLD. X-ray reflectivity confirms the roughness estimate given by AFM and supports an interface layer that exhibits different properties compared to the 'bulk' film. The enhanced interface roughness is most probably due to dislocations and crystalline imperfections which are caused by strain relaxations. Furthermore, the in- and out-of-plane lattice strain derived by XRD is rather small compared to the high lattice mismatch to ZnO and the 'bulk' film structure is nearly fully relaxed.

3.6.2 Electronic and chemical structure studied by XPS and HAXPES

X-ray photoelectron spectroscopy was used to characterize the chemical and electronic properties of the Fe_3O_4 films grown by PLD and MBE on MgO and ZnO substrates. For a quantitative analysis, the Fe $2p$ core-level spectrum was recorded for all samples. After a Shirley background subtraction, the spectra were fitted with single crystal spectra of FeO, Fe_3O_4 and Fe_2O_3 as a reference. From this the off-stoichiometry parameter δ was calculated. The parameter describes the iron off-stoichiometry in the form $[Fe^{3+}]_{tet}$ $[Fe^{2+}_{1-3\delta}\ Fe^{3+}_{1+2\delta}\ Vac^{Fe}_{\delta}]_{oct}\ O^{2-}_4$ and thus the transition from Fe_3O_4 towards γ-Fe_2O_3 [129]. The tetrahedrally coordinated Fe^{3+}-sites remain unchanged, whereas the octahedrally coordinated Fe^{2+}-sites are substituted by Fe^{3+}-sites and iron vacancies.

A typical fit is shown in Fig. 3.13 (a). The data was well reproduced using Fe_3O_4 and Fe_2O_3 spectra, which are shown as dotted lines in the graph. It can be seen that the film is slightly overoxidized and a δ of 0.047 is derived. Panel (b) of Fig. 3.13 shows the comparison of Fe $2p$ core-level spectra taken for PLD and MBE grown films on MgO and ZnO substrates. The films fabricated by PLD (samples D, F) were measured *in situ* at the University of Twente using an Al K_α source. The measurements of the MBE grown samples (samples G,H) were performed at the KMC-1 beamline at the Helmholtz Zentrum Berlin (BESSY II) using the HIKE endstation [130]. Here, the samples were transferred under argon atmosphere between the vacuum systems, with exposure to ambient atmosphere being kept as short as possible to minimize surface contamination. The main difference between these two measurements is the increased probing depth of the HAXPES measurements. This allows for a more precise study of thicker films and interface properties as well as depth profiling of the film. The HAXPES measurements were done at a photon energy of 3 keV and an emission angle of 5°, resulting in an effective electron mean free path of 38 Å, whereas for the XPS measurements (θ=0°) it amounts to 16 Å for this core-level. Comparing the mean free path to the film thicknesses, in the case of the HAXPES measurements the bulk film properties are probed, while for the thicker PLD grown films conventional XPS probes only about the first 5 nm. Nevertheless, as the measurements were done *in situ* these measurements as well give a reasonable estimate for the sample composition. Note that

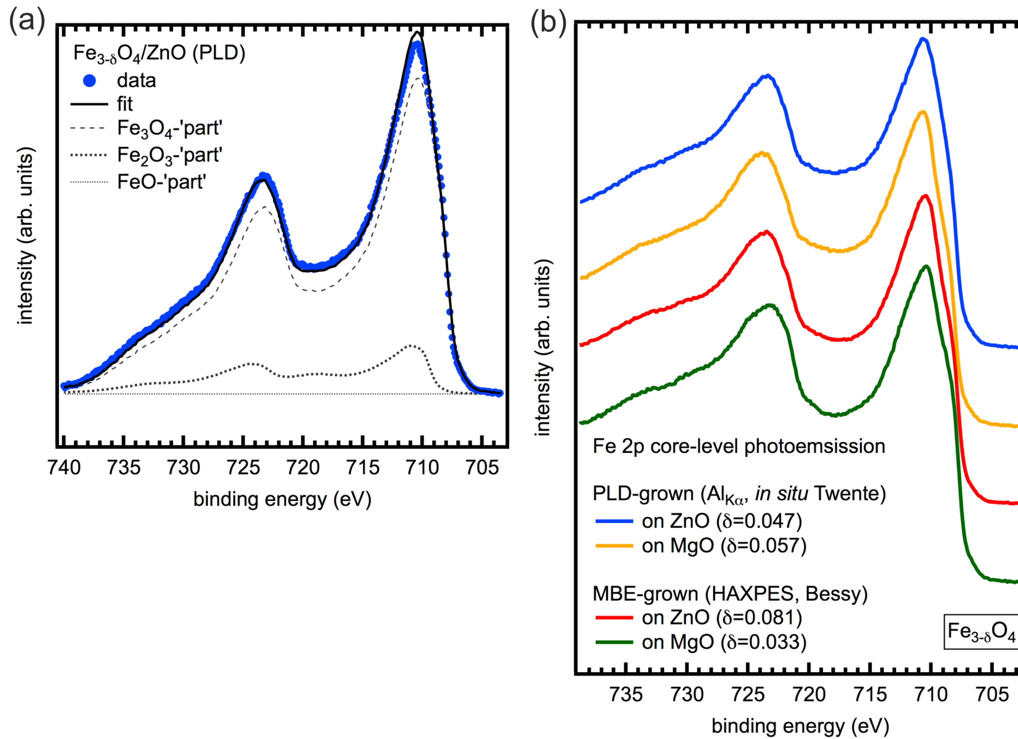

Figure 3.13: *Fe 2p core-level spectra of films prepared by PLD and MBE. (a) Fitting Shirley background corrected data with single crystal reference spectra leads to an off-stoichiometry of 0.047. (b) Comparison of films grown on MgO and ZnO substrates. By choosing an adequate oxygen pressure, nearly stoichiometric Fe_3O_4 thin films can be obtained by PLD and MBE growth.*

for the MBE grown samples, too, conventional *in situ* XPS measurements were used to analyze the precise off-stoichiometry, as only single crystal spectra recorded by XPS were available and differences in, e. g., spectral resolution hindered a quantitative comparison to the HAXPES results.

Already a qualitative analysis of these spectra, namely the smeared-out area between the two main lines and the shoulder at the lower binding energy side of the main Fe $2p_{3/2}$ peak, which has been described before, shows that both methods can be used to grow Fe_3O_4 films. In terms of chemical composition and oxidation state, the magnetite films on ZnO show the same level of quality compared to the films on MgO. However, growth pressure has to be chosen adequately for the selected growth method and substrate. The derived off-stoichiometry ranges from 0.033 to 0.081 being highest for the film grown on ZnO by MBE. M. Paul derived values between 0.028 and 0.11 for Fe_3O_4/ZnO grown by MBE, i. e., the off-stoichiometry is in the same range and independent of the substrate [123]. Values for δ are given in Tab. 3.4 and will be further discussed in Sec. 3.6.3 as the off-stoichiometry can also be derived by means of x-ray absorption spectroscopy (XAS) and x-ray magnetic circular dichroism (XMCD).

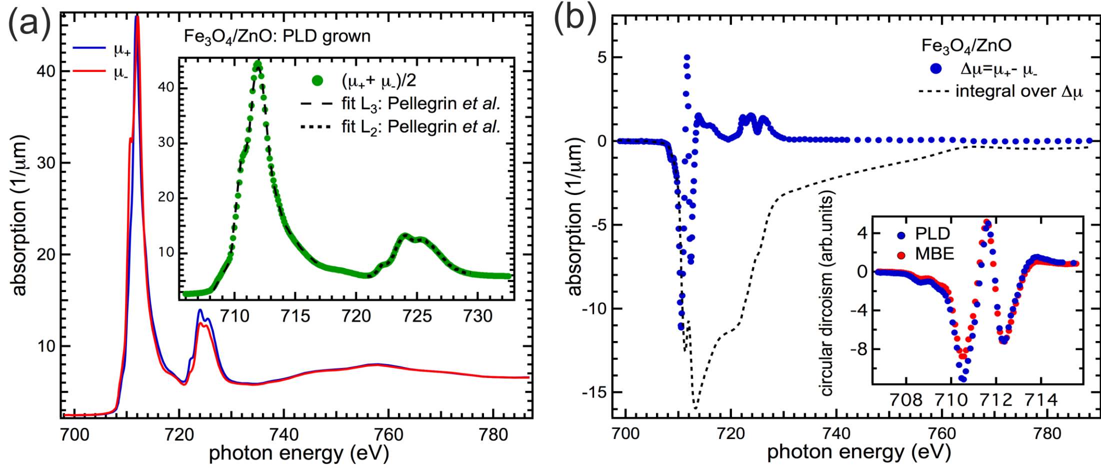

Figure 3.14: *Fe_3O_4/ZnO grown by PLD: (a) XAS recorded in a magnetic field of ±3T showing a clear dependence on the applied field. Inset: Fit to the magnetization-averaged XAS spectra using reference data taken from Pellegrin et al. to determine the off-stoichiometry [129]. (b) XMCD intensity and integrated intensity to derive spin and orbital moments from sum-rule calculations. Inset: Comparison of the XMCD spectra of Fe_3O_4/ZnO films grown by PLD and MBE. The difference in the spectral line shape is due to variations in δ.*

3.6.3 Magnetic properties

To compare the magnetic properties of the Fe_3O_4 films (samples F, G, H, I) grown by PLD and MBE, XMCD was used as a spectroscopic method, since it is sensitive to the magnetic moment of the individual species of atoms. A detailed description of both methods and sum-rule calculations that allow for an estimation of the magnetic moment can be found in Refs. [131, 132]. Details on the calculations and spectra processing of this material system are best given in Refs. [123, 133]. XAS and XMCD reference spectra are used for an independent determination of the off-stoichiometry parameter δ [129].

XAS and XMCD

XAS and XMCD experiments were conducted at the PM 3 bending magnet beamline for circular polarization at the Helmholtz Zentrum Berlin (BESSY II) using the 'superconducting 3T UHV magnet' endstation. Normal incidence XAS spectra were recorded at room temperature in the total electron yield mode (TEY, sample drain current) at a constant helicity with a polarization degree of about 0.93 and applied magnetic fields of $\mu_0 H = \pm 3\,\mathrm{T}$.

The XAS Fe $L_{3,2}$ absorption spectra taken in a magnetic field of ±3 T are shown for a PLD grown Fe_3O_4 film in Fig. 3.14 (a). The difference between these spectra is caused by different densities of final states in the majority- and minority-spin bands. The so-called x-ray magnetic circular dichroism, which is shown in Fig. 3.14 (b), is a direct measure

for the net magnetization. Turning back to panel (a), the inset shows the polarization-averaged absorption spectra of this film and a fit of the data using reference spectra taken from Pellegrin *et al.* [129]. The XAS fine structure depends on the precise iron valence state as is also the case for the XPS spectra (cf. Sec. 3.3), and thus it can be used to distinguish the iron oxides. For instance the shoulder ($h\nu$=710.6 eV) of the main peak at $h\nu$=712.0 eV decreases strongly with decreasing Fe^{2+} fraction, resulting in a higher value for the off-stoichiometry parameter δ. In Tab. 3.4, the δ values derived by XPS, XAS and XMCD are presented for films grown by either method and on either substrate. In general, the off-stoichiometry is higher in the case of XAS and XMCD. This is due to surface overoxidation caused by short air exposure of the samples, which was not present for the *in situ* XPS measurements. The discrepancy between the XAS and XMCD data is most likely due to differences in the XAS and the XMCD reference spectra. However, except for the finding that all films seem to be slightly overoxidized, no trends can be seen regarding the growth method or the choice of the substrate. Thus, it can be concluded that it is mainly the oxygen partial pressure during growth and a further oxidation of the surface in ambient air that determines the stoichiometry of the thin films.

Table 3.4: *Off-stoichiometry parameters of $Fe_{3-\delta}O_4$ films derived from XPS, XAS and XMCD analyses. A general overoxidation of the films is found. Values derived by XAS and XMCD are higher, because measurements were not carried out in situ.*

	substrate/growth method	δ (XPS)	δ (XAS)	δ (XMCD)
sample D	ZnO_{PLD}	0.047	—	—
sample F	MgO_{PLD}	0.057	0.088	0.118
sample G	ZnO_{MBE}	0.081	0.094	0.061
sample H	MgO_{MBE}	0.033	0.096	0.077
sample I	ZnO_{PLD}	0.020	0.044	0.020
		$\Delta\delta$=30 %		

Figure 3.14 (b) shows the dichroic signal of the Fe_3O_4/ZnO film grown by PLD together with the integrated intensity which is necessary for sum-rule calculations to derive the magnetic moments. The integration range strongly influences the value of the derived orbital moment m_{orb} and is controversially discussed in the literature [134, 135]. The dichroism spectrum is in good agreement with the one published by Goering *et al* [134]. The inset shows the L_3 dichroic spectra of films grown by MBE and PLD on ZnO. The dichroic signal is particularly sensitive to the ionic Fe stoichiometry, including the repartition of the ions over the sublattices [129, 136]. The first negative extremum is reduced in the case of the MBE grown film, which is due to the higher off-stoichiometry. From the dichroic spectra the spin moment m_{spin} and orbital moment m_{orb} were derived (see Tab. 3.5). Additionally, the overall magnetic moment of the films grown by PLD was

measured using a vibrating sample magnetometer (VSM). For the VSM measurements the external field was swept up to $\mu_0 H_{max} = \pm 1.0\,T$. In a VSM, the sample is moved sinusoidally in an external magnetic field. Probing-coils measure the induced magnetic field, which is used to determine the magnetic moment [137]. From the saturation magnetization the magnetic moment per formula unit (f. u.) is calculated with respect to the precise film volume.

Table 3.5: *Magnetic moments derived by sum-rule calculations (XMCD) and VSM analyses of Fe_3O_4 films. The values are reduced in comparison to bulk Fe_3O_4 independently of the measurement technique.*

	substrate/ growth method	m_{spin} (μ_B/f.u.) (XMCD)	m_{orb} (μ_B/f.u.) (XMCD)	m (μ_B/f.u.) (VSM)
sample I	ZnO_{PLD}	2.52	0.02	2.73
sample F	MgO_{PLD}	3.27	0.12	3.36
sample G	ZnO_{MBE}	—	—	—
sample H	MgO_{MBE}	2.55	0.09	—
		Δ=0.15 μ_B/f.u.	Δ=0.06 μ_B/f.u.	Δ=0.5 μ_B/f.u.

Compared to the theoretical value of the overall magnetic moment of 4.0 μ_B/f.u. the values derived for all films are much smaller. The formation of a magnetically dead layer at the surface, which would explain the reduced value measured by XMCD due to its surface sensitivity is unlikely, because the values are confirmed by volume-sensitive VSM measurements. However, the error margin for the VSM measurements is quite high, since the VSM signal has to be corrected by the diamagnetic background and films may not be completely saturated at $\pm 1\,T$. A further source of error is the precise determination of the film volume.

M. Paul found comparable values in similar XMCD analyses, but larger values for the ‘bulk’ magnetic moment by means of SQUID measurements, which in general probe the same sample properties as VSM [123]. Nevertheless, the SQUID measurements were performed in magnetic fields up to $\pm 6\,T$, what might support the assumption of an incomplete saturation of the films reported here. M. Paul discussed errors in the sum-rule calculations as a possible explanation for the discrepancy of the XMCD and SQUID measurements [123]. Kallmayer *et al.* also found reduced values for films on MgO and Al_2O_3 by means of XMCD, but derived nearly the theoretical value by VSM [135]. They mention errors in the VSM measurements and the finite x-ray polarization as possible reasons. Besides an incomplete saturation, intrinsic effects as well might cause the reduced values. It is known from the literature that the magnetic moments are reduced at room temperature to about 3.83 μ_B/f.u. [89]. Off-stoichiometry, too, results in a reduction of the magnetic moment [81, 89]. However, both effects are small and cannot fully account for this large reduction [123]. Defects in the film such as anti-

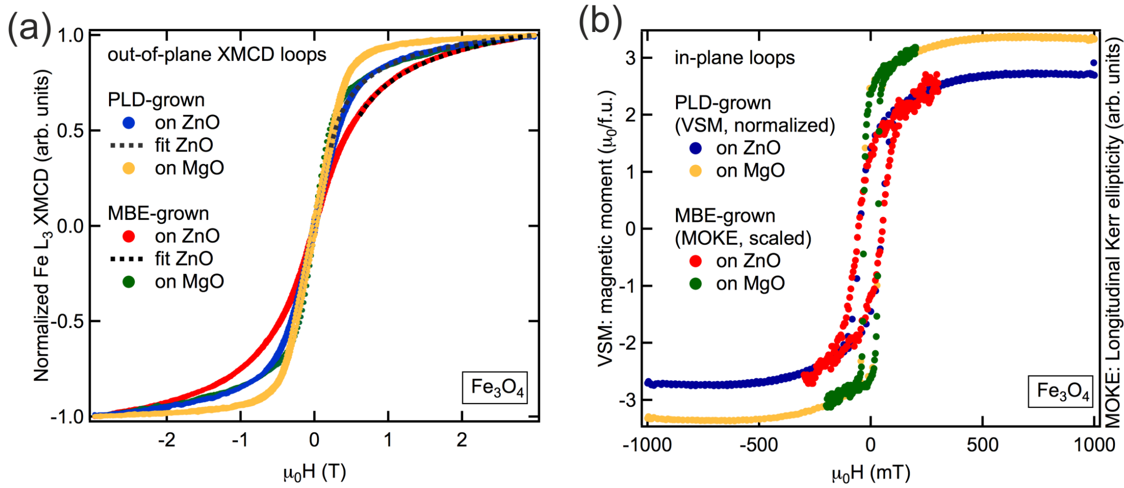

Figure 3.15: *Magnetization curves of differently prepared Fe_3O_4 films on ZnO and MgO: (a) Out-of-plane curves measured by XMCD showing different magnetization behavior, i. e., films on ZnO exhibit a higher anisotropy field. (b) In-plane curves measured by VSM and MOKE. Independent of the growth method films on ZnO show a large coercivity.*

phase boundaries or effects originating from the initial island growth might also influence the overall magnetic moments. This will be further discussed in the next section. The orbital moment m_{orb} seems to be almost completely quenched in these films. However, as already discussed, the values strongly depend on the integration range, which was chosen similarly to Goering *et al.* and hence, the values are comparable [134].

Magnetization curves

The normalized out-of-plane magnetization curves were measured at room temperature for all films in the TEY mode at the first (negative) extremum (Fe^{2+}) of the Fe L_3 XMCD spectrum (see Fig. 3.15 (a)). The in-plane loops were probed using VSM for the PLD grown films (sample F, I) and magneto-optical Kerr effect (MOKE) measurements for the MBE grown films (sample G, H). MOKE experiments were conducted at a photon energy of $h\nu$=1.85 eV and in applied fields up to $\mu_0 H_{max} = \pm 0.3$ T. As a comparison, the MOKE curves were normalized to the respective VSM measurements and displayed in Fig. 3.15 (b). MOKE measurements utilize intensity variations and rotations of the polarization of linearly polarized light occurring upon reflection on a magnetic material. The rotation is directly related to the magnetization of the material within the probing region of the light and is thus an indirect measure of the magnetization behavior [138].

Turning to the out-of-plane loops, films differ in the squareness of the loops, which means that, for instance, Fe_3O_4/ZnO grown by MBE is much harder to magnetize and thus has a higher anisotropy field than the film grown by PLD. Moreover, both films grown by PLD exhibit a more square-like behavior than films grown by MBE. A comparison of the in-plane loops and the out-of-plane loops reveals that the surface normal

corresponds to a hard magnetization axis. Furthermore, in-plane MOKE loops were recorded at different azimuthal angles. Their shape is nearly independent of the azimuthal angle. Thus, irrespective of the substrate the Fe_3O_4 films display little, if any, in-plane magnetic anisotropy. At the quantitative level the in-plane loops of the films on the same substrate grown by PLD and MBE show only marginal differences in terms of coercivity and overall hysteresis shape. However, comparing films on different substrates, ZnO based films possess larger coercive fields ($\mu_0 H_C^{ZnO} \approx 50\,\mathrm{mT}$, $\mu_0 H_C^{MgO} \approx 31\,\mathrm{mT}$) and, at the same time, a reduced squareness of the hysteresis cycles. Thus, Fe_3O_4 grown on ZnO is less easily saturated than is Fe_3O_4 on MgO. The overall magnetization values given in Tab. 3.5 were calculated from the present VSM loops.

Defects of various kinds are generally prime candidates for acting as domain wall pinning centers during magnetization reversal and are also known to be local sources of potentially strong magnetic anisotropy in magnetite, what could be the reason for the slow saturation behavior and the reduced magnetic moment [139]. Anti-phase boundaries (APB) were already named as possible defects [140]. APBs are structural defects caused by a shift of the cation sublattice with respect to the unperturbed O sublattice. Shifts in magnetite on ZnO can occur along the $\frac{1}{2}\langle 100 \rangle$ or $\frac{1}{4}\langle 110 \rangle$ directions, whereas on MgO, shifts are along $\frac{1}{4}\langle 100 \rangle$ or $\frac{1}{4}\langle 110 \rangle$. Considering a growth mode of coalescing islands, these APBs can easily be formed when islands coalesce, which are half a unit cell out of phase regarding the stacking sequence of the spinel structure. Despite this shift, samples are still monocrystalline due to the continuous O sublattice. The shift, however, changes the local magnetic coupling at an APB. In bulk magnetite, the antiferromagnetic behavior results from the antiferromagnetic superexchange of the *A*- and *B*-sites, which in turn are ferromagnetically coupled among themselves. Margulies *et al.* proposed a strong antiferromagnetic coupling of the *B*-sites across an APB, which would act as an immobile magnetic domain wall [93]. This can lead to superparamagnetic fluctuations in the limits of very thin films and high APB densities [140–142]. An alignment of the magnetic moments only occurs in comparably large fields. This leads to a slow approach to saturation and an overall decreased saturation magnetization at finite fields. Margulies *et al.* described this slow magnetization behavior with a one-dimensional model of ferromagnetically ordered spins that couple antiferromagnetically at an APB [93]. Although this model is highly simplified, Hibma *et al.* used the following formula to quantitatively describe the reduction of the magnetization M in an external field H due to the density b of the APBs [141]:

$$M = M_s(1 - b \cdot H^{1/2}) \tag{3.1}$$

Here, M_s is the saturation magnetization. Magnetization curves obtained from XMCD were recorded up to sufficiently high fields to yield satisfying fit results. Nevertheless, M_s could not be determined, as absolute values for the saturation were not available for all films. The fits are shown as dotted lines for films on ZnO in Fig. 3.15 (a). The parameter b, which is proportional to the density of the APB in this model, is given in Tab. 3.6. For

both growth methods, the APB density is higher for films on ZnO substrates compared to MgO. In the literature slow saturation behavior was found for Fe_3O_4 films grown on MgO and Al_2O_3 substrates [141, 143]. In the latter case, Fe_3O_4 grows also in the [111] direction with a comparable lattice mismatch of about 8 % as is the case for growth on ZnO. Compared to the growth in [100] direction on the perfect lattice matching MgO, a higher densities of APBs was found. It can be concluded that due to the higher lattice mismatch, the density of the initially formed islands is different. An increased number of individually growing islands also enhances the probability of the formation of an APB, which may lead to the different saturation behavior on MgO and ZnO substrates.

Table 3.6: *Density of anti-phase boundaries in Fe_3O_4 films. A higher density is found for films on ZnO.*

	substrate/ growth method	b $\propto$ APB
sample I	ZnO_{PLD}	0.31
sample F	MgO_{PLD}	0.17
sample G	ZnO_{MBE}	0.45
sample H	MgO_{MBE}	0.27

Although a slow saturation and a reduced magnetization indicate the presence of the APBs, further proof of this hypothesis could be obtained by directly imaging these boundaries. M. Paul could identify APBs for the MBE grown films on ZnO by means of STEM. However, a detailed study of their density by STEM remains complicated as representative studies have to include a multitude of STEM lamellae analyses, which in practice is not applicable.

In summary, the XAS/XMCD confirm the slight off-stoichiometry of the films and thus confirm the XPS results. The magnetic moment of the films is reduced; however, temperature and off-stoichiometry effects cannot fully account for this. Both the reduced magnetic moment and the slow magnetization behavior point to the presence of ABPs. An increased APB density in films grown on ZnO substrates compared to MgO substrates might result from the higher lattice mismatch.

3.6.4 Indications for a Verwey transition

Figure 3.16 shows the temperature dependence of the coercivity for the PLD grown films on MgO and ZnO (samples H, I). For this purpose hysteresis loops were recorded by VSM at various temperatures. For both films, the coercivity increases at low temperatures, exhibiting a kink between 100-140 K. In the case of MgO, a slight reduction can be seen from room temperature to this point, which is not present for the film on ZnO. However, in the latter case, the kink is shifted to lower temperatures.

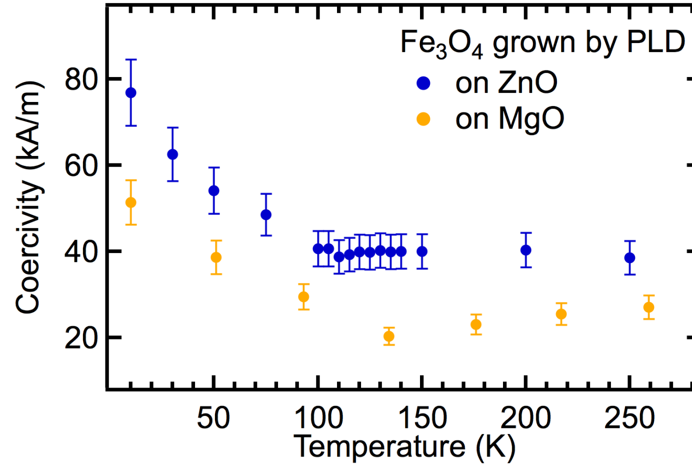

Figure 3.16: *Temperature dependence of the coercivity for films grown by PLD. The kink at about 120 K indicates a Verwey transition.*

Similar behavior was found for magnetite single crystals, nanoparticles, and films grown on fused quartz crystals by PLD [144–146]. Absolute values for both the coercivity and the increase of the coercivity strongly differ among the measured samples and depend on the sample size, the crystallinity, and the stoichiometry. Nevertheless, all groups observe a jump of the coercivity near the isotropic point (T_I=130 K) and the Verwey temperature (T_V=114-135 K). The Verwey transition is accompanied by a structural phase transition from cubic to monoclinic symmetry. The latter exhibits a higher magnetocrystalline anisotropy, which results in a higher coercivity. At the isotropic point the magnetocrystalline anisotropy vanishes as it changes signs. This might explain the slight drop in this temperature region for the film on MgO [144]. Furthermore, other groups find a relatively sharp increase of the coercivity followed by a plateau at low temperatures, which the films in this study do not exhibit. A Verwey transition is only found in samples with good crystalline quality. Defects like APBs or oxygen off-stoichiometry lower the Verwey temperature; for instance a T_V of 81 K was found for a δ of 0.016 [93, 147]. A shift of the temperature and thus the kink in coercivity might explain the broadening of the jump and the absence of a plateau in these films. The off-stoichiometry determined by XPS and XAS for these films is comparatively high, so it is surprising to observe a Verwey transition at all. One possible explanation is the comparably high surface sensitivity of both measurements. It could be the case that the off-stoichiometry in the 'bulk' film is smaller compared to the off-stoichiometry of the film region probed by XPS and XAS. Such inhomogenities in the off-stoichiometry, but also in the APB density, might explain the broadening of the kink. Although the film surface might exhibit a higher off-stoichiometry, the presence of the Verwey transition manifests the high quality of the 'bulk' films on both substrates.

3.7 Tailoring the interface – pressure variation during growth

To analyze the interface and the possible formation of an FeO-like interlayer more thoroughly, films of different thicknesses and prepared under various oxygen partial pressures were studied using XPS and HAXPES depth profiling.

The films under investigation in this study were grown on ZnO substrates using MBE (samples G, J, K, L). Comparable results were found for PLD grown films (see Sec. 3.5). Photoemission (Al K_α) was used to determine the iron oxidation state of these thin films. The data is shown in Fig. 3.17 (a). Note that the film thickness was derived by XPS and iron flux measurements. The determination by XPS is based on the assumption of a closed film layer and will have an increased error margin for films growing in an island-like growth mode.

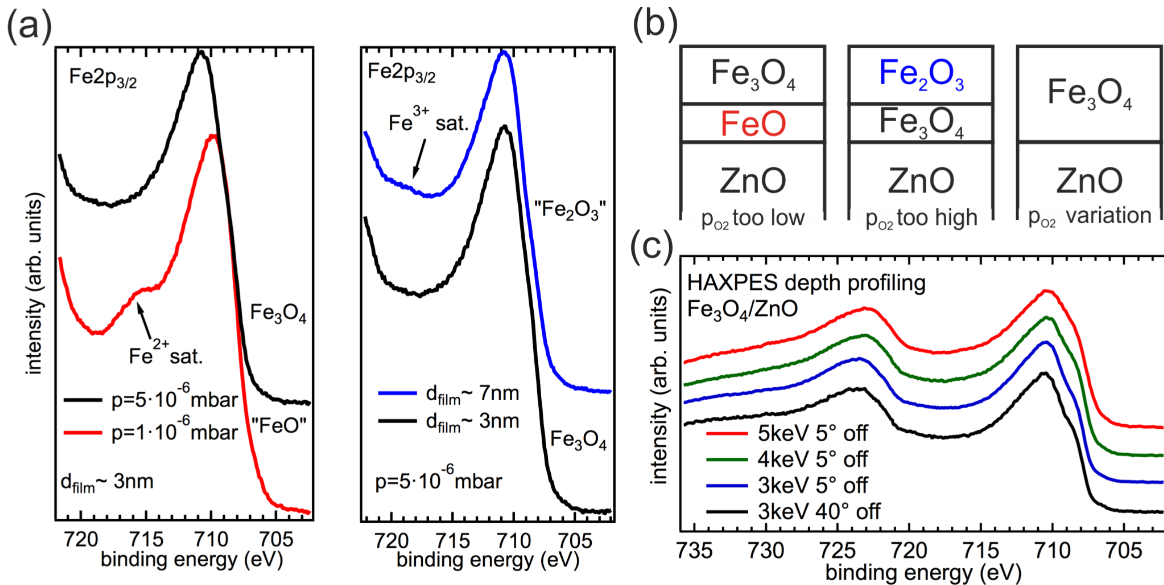

Figure 3.17: *(a) XPS spectra of the Fe 2p core-level of iron oxide films grown on ZnO by MBE. The spectra show that oxygen partial pressure and film thickness play an essential role in the formation of various Fe oxide phases. (b) Sketch of possible film growth depending on the oxygen pressure during growth. (c) HAXPES depth profiling (λ_{eff}=6.3-2.9 nm) of a 12 nm thick Fe_3O_4/ZnO film grown by MBE.*

For thin iron oxide films (∼3 nm), a too low oxygen partial pressure leads to the formation of FeO, indicated by the Fe^{2+} charge transfer satellite in the left panel of Fig. 3.17 (a). It can be assumed that at low pressures the formation of FeO is favored due to the smaller lattice mismatch. Thus, the oxygen pressure must be sufficiently high to force the formation of Fe_3O_4. However, the very same oxygen pressure leads to an overoxidation and to the formation of Fe_2O_3 for thicker films identified by the Fe^{3+} satellite peak (see right panel Fig. 3.17 (a)). For clarification a sketch of the different

growth scenarios is presented in the upper panel of Fig. 3.17 (b). A too low growth pressure leads to an interfacial FeO-like layer, whereas the same pressure leads to the formation of Fe_3O_4 for thicker films. In turn, if the pressure is chosen adequately to form Fe_3O_4 near the interface, Fe_2O_3 is formed in the 'bulk' film. To prevent the formation of Fe_2O_3 as a bulk film material, a certain pressure variation has to be applied.

HAXPES depth profiling of a 12 nm thick film (sample G), which was fabricated using a pressure variation during growth, is shown in Fig. 3.17 (c). For all probing depths the spectra are virtually identical, which confirms a homogeneous film composition in vertical direction. This is positively influenced by varying the growth pressure. Note that the intensity difference at the higher binding energy side is due to inelastically scattered background electrons that depend on the measurement geometry.

From this study it can be concluded, that a pressure variation during growth reduces a FeO-like interface layer, which forms otherwise due to a smaller lattice mismatch.

3.8 Summary and outlook

The successful growth of Fe_3O_4/ZnO was accomplished by both MBE and PLD. By tuning the oxygen pressure correctly, HAXPES depth profiling clearly indicates a uniform Fe_3O_4 film phase. The absence of RHEED oscillations indicates an island-like growth mode with an in-plane registry of the individual islands that tend to coalesce for thicker films. Structurally the films are nearly completely relaxed as probed by XRD. Although the films show a slight off-stoichiometry, the Verwey transition could be identified for PLD grown films. The island-like growth mode most probably produces a high density of anti-phase boundaries that lower the overall magnetic moment and lead to a slow magnetization behavior. STEM studies by Paul *et al.* and x-ray magnetic reflectivity studies by Brück *et al.* showed that the interfaces of these heterostructures exhibit only minor disorders and should not hinder spin injection [148, 149].

Future work should include attempts to raise the magnetic moments of these films. One way of accomplishing this could be a post-oxidation and annealing procedure to heal out possible defects. However, a more detailed STEM study is required to, e. g., map the densities of the APBs altered by these procedures. Furthermore, the influence of the ZnO surface termination was disregarded completely. However, spin diffusion across the Fe_3O_4/ZnO interfaces may depend on the termination of ZnO. Most important is to test the spin injection capability of these heterostructures. As a starting point, photoemission could give valuable information on the band alignment of these structures and will reveal whether spin injection is feasible at all. For this, doping of ZnO might be a crucial parameter. The degree of spin polarization of the film material, too, can be probed by spin-resolved HAXPES, as this is strongly influenced by strain and depends on crystalline directions. Furthermore, four-probe transport measurements similar to those done by Li *et al.* [106] or spin-dependent MOKE measurements can give insight to the degree of spin polarization achievable in ZnO.

4 $LaAlO_3/SrTiO_3$ – growth conditions and interface electron system

Abstract

Heterostructures consisting of the two band insulators LAO and STO exhibit a conducting interface above a critical LAO overlayer thickness. An explanation for the thickness dependence of the conductivity is given by the so-called electronic reconstruction. The transfer of half an electron per unit cell counteracts the potential build-up owing to the polarity of LAO. However, also extrinsic effects like oxygen vacancies, intermixing and off-stoichiometry play a certain role and may even dominate depending on the preparation conditions. In this study, the influence of the growth conditions on the structural and interfacial properties is analyzed. A change of the growth kinetics was observed for high background pressures, which resulted in macroscopically insulating samples originating most probably from a higher degree of disorder within the film. The amount of charge carriers and the spatial extension of the conducting layer strongly depend on the amount of oxygen provided during growth. Post-growth oxidation proved to be essential for a further study of intrinsic sample properties.

4.1 Introduction to perovskite oxides

Perovskite oxides show a vast variety of different physical phenomena including insulating or conducting behavior, various forms of magnetism, or even superconductivity. Nonetheless, they all exhibit the same crystal lattice structure, which is known as the perovskite structure and is displayed in Fig. 4.1. The unit cell of the ABO_3 structure is formed by two different types of cations A and B, and oxygen as the anion, which is located on the face center position of the cube. The A-site cations are at the cube corners and the B-site cations are at the body center position. Alternatively, this structure can be described as a layered system formed by alternating AO- and BO_2-planes, which directly leads to the possibility of two surface terminations depending on the first layer being the A-cation or the B-cation layer.

The physical properties depend on different factors and can be influenced in various ways: (i) For both cations, A- and B-sites, various elements can be chosen, mostly

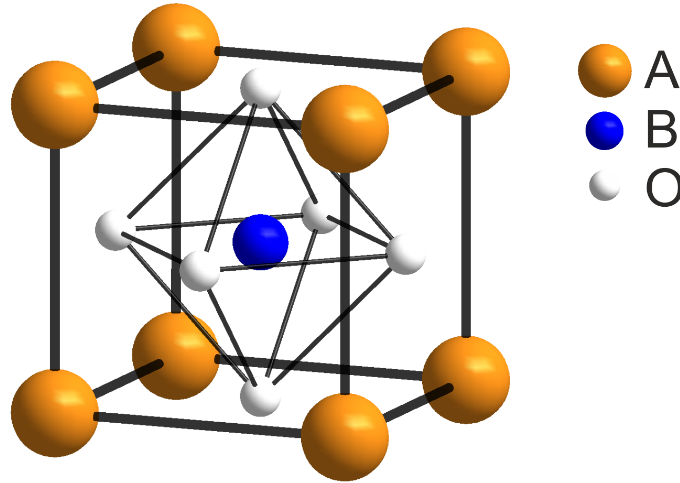

Figure 4.1: *Perovskite lattice structure of type ABO_3. Space group: $Pm\bar{3}m$.*

group II or group III elements for the A-site and period 3 to 6 elements for the B-sites. Although charge neutrality of the ABO_3 compound must be fulfilled, a multitude of combinations can be realized and the physical properties vary tremendously. (ii) Due to different cation sizes, distortions can arise between the AO- and BO_2-planes. Those can lead to electric dipole moments, which can result, e. g., in ferroelectricity, as is the case for $BaTiO_3$ [150]. (iii) While the charge neutrality of our world demands a charge-neutral unit cell (uc), this does not have to be the case for the individual AO- and BO_2-planes. Thus, non-polar and polar perovskites can be defined. The polar structures were classified by Tasker *et al.* according to their dipole moment and a resulting stability or possible required reconstruction [88]. In this context, e. g., STO, which is formed by neutral $(SrO)^0$ and $(TiO_2)^0$ planes, can be described as a *type* 1 structure, whereas LAO, which consists of charged $(LaO)^+$ and $(AlO_2)^-$ layers, is classified as *type* 3 with charged planes and a net dipole moment perpendicular to the surface, requiring surface reconstructions.*

Changing the composition of a material system or combining two materials is one way to artificially manipulate their physical properties. An example is doping of $LaTiO_3$. The successive substitution of La by Sr leads to a metal-insulator transition (MIT) [151]. For the combination of materials with different properties the perovskite oxides provide an excellent playground, since the likewise lattice structure comes along with only small differences in the lattice constants (∼3.7 Å-4.2 Å). Symmetry breaking at interfaces is another effect that may lead to new physical phenomena.

The materials under investigation in this chapter are LAO and STO. The former is a wide band gap material (E_{gap}=5.6 eV) with a rhombohedrally distorted pervoskite structure (a, b=5.366 Å; c=13.112 Å). The distortions are caused by an antiphase rotation

*Within this classification, single crystals were assumed to exhibit a (001)-oriented surface.

of the oxygen octahedra. At about 813 K a phase transition occurs to an ideal cubic structure [152]. Pristine STO exhibits a band gap of 3.2 eV and a lattice constant of 3.905 Å. Its cubic crystal structure, an easy control of its surface termination and not least its vast availability make it often used as a substrate for oxide heterostructures. At 110 K, STO undergoes a phase transition from cubic to tetragonal caused by a tilt in the oxygen octhahedra [153].

4.2 Conducting interface of $LaAlO_3/SrTiO_3$

One of the most striking observations in this field has been the discovery of a conducting interface between the two band insulators LAO and STO by Ohtomo and Hwang in 2004 [15]. Conductivity only occurs, if more than three unit cells of LAO are grown on TiO_2-terminated STO (n-type), whereas films grown on SrO-terminated STO (p-type) remain insulating independent of their thickness [15, 17]. This finding triggered tremendous efforts to explain this behavior from a theoretical and an experimental point of view. Further experiments showed that the ground state could exhibit either superconducting or magnetic behavior, strongly depending on the growth conditions and the after-growth treatment [154, 155]. Most recently it was reported that in the ground state both superconductivity and ferromagnetism coexist [16, 156]. Post-oxidation was found to trigger superconductivity, independently of the growth conditions [157]. To explain the thickness-dependent MIT an electronic reconstruction caused by the polar character of LAO was proposed [18, 158].

As shown in Fig. 4.2 the successive stacking of the polar $(LAO)^+$ and $(AlO_2)^-$ planes leads to a potential build-up, if no reconstruction is assumed. In this unreconstructed scenario, the potential diverges for infinitely thick LAO films. To overcome this effect, the model proposes the transfer of 0.5 e^- per 2D unit cell from the surface to the interface, which avoids the potential build-up. The charge transfer is highlighted in grey in the drawing and is here realized as additional charge in the first TiO_2 layer of the STO. This results in a vanishing potential outside the crystal. However, this will only happen, if hosting of extra electrons at the interface is energetically more favorable than the potential build-up. Hence, in the ideal case, the states at the valence band maximum of LAO have to be shifted towards the Fermi energy by the potential gradient across the LAO overlayer until charge can be transferred to empty states at the conduction band minimum of STO at the interface.

Density functional theory (DFT) was used by serveral groups to investigate this phenomenon [159–162]. However, care has to be taken when comparing theory to experiment. In general, periodic boundary conditions are used for DFT calculations. These do not allow for a potential built-up over the entire supercell. One approach is to construct the supercell in such a way that it exhibits two n-type interfaces by assuming $(m+1)$ LaO and m AlO_2 layers as well as $(n+1)$ SrO and n TiO_2 layers. This approach suffers from the drawback that an additional electron is automatically put into the system.

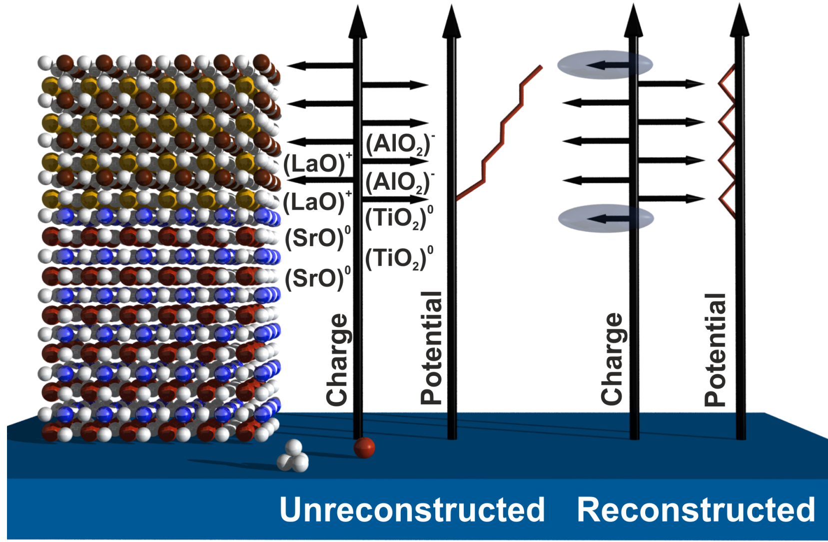

Figure 4.2: *Schematics of the electronic reconstruction adopted from Hwang et al. [18]. The transfer of half an electron from the surface to the interface avoids the potential build-up.*

Nonetheless, information can be gained on the spatial distribution of this electron. Another approach is to include a vacuum space within the supercell and account for the potential by either a dipole correction or a mirror plane. By this means, the potential build-up and the electronic re-construction can be simulated. Using a vacuum space in the supercell, Pentecheva *et al.* calculated the layer-resolved density of states for LAO/STO [161]. They found a crossing of the valence band maximum in LAO and the conduction band minimum in STO at around five monolayers. Their calculations derive a shift of 0.4 eV per layer of the LAO bands. From simple electrostatics, a potential build-up of 0.9 eV per layer is calculated. By contrast, in experiments such a potential gradient, i. e., a shift of the bands, has not been observed. Core-level photoemission studies showed shifts below 0.1 eV and thus much smaller as assumed in the electronic reconstruction model [163, 164].

In principle, the electronic reconstruction scenario should be applicable for both n-type and p-type interfaces, resulting in the former case in electron-mediated, in the latter case in hole-mediated conductivity at the interface. However, p-type interfaces are insulating. Extending the picture of the electronic reconstruction by taking oxygen vacancies into account, the vanishing band gradient and the insulating behavior of the p-type interface may be explained. p-type interfaces would acquire stabilizing holes within the first STO layers to screen the dipole moment, but the electron-hole asymmetry makes other reconstructions like intermixing or oxygen vacancies energetically more favorable [15, 165, 166]. Zhong *et al.* calculated the formation of oxygen vacancies to be more favorable in the interface for p-type interfaces, whereas for n-type interfaces, formation

energies were smallest at the LAO surface. Li *et al.* calculated the spatially resolved density of states for LAO/STO assuming oxygen vacancies at the LAO surface [167]. They found flat band behavior of the LAO bands in the case of 0.25 oxygen vacancies per unit cell area. Furthermore, it was found that the formation energy of these vacancies strongly depends on the LAO overlayer thickness itself, which may explain the thickness dependence of the conductivity.

A completely different explanation deals with the activation of in-gap states at the interface by an induced polarization in the STO caused by the LAO overlayer [168]. As LAO is a 'pseudo'-perovskite with a rotation of the oxygen octahedra, this rotation could be induced in the STO above a certain LAO overlayer thickness. These induced rotations might result in a polarization of the STO. First hints for an induced polarization are given by experiments using second harmonic generation [169, 170]. Such a polarization in the STO might change the local band structure at the interface and lead to conductivity. Both explanations, the induced polarization and the electronic reconstruction, can be seen as intrinsic effects to avoid the polar catastrophe.

However, extrinsic effects caused by the fabrication process are also discussed and have to be taken into account at least for samples grown at certain growth conditions. Heating of STO in vacuum causes the formation of oxygen vacancies, which are discussed as a possible explanation for conductivity in LAO/STO by several groups [171–173]. Moreover, sputtering processes during growth can lead to interface intermixing, i. e., La-Sr interdiffusion which would form a $La_xSr_{1-x}TiO_3$ layer. For a high enough intermixing ratio conductivity can be expected [174–177]. Neither of the two latter explanations can account for the presence of a critical film thickness and therefore they are not conclusive.

From an experimental point of view, several efforts have been carried out to further characterize the conductive layer in LAO/STO. From Hall effect measurements the charge carrier density is determined to be about $10^{13}\,e^-/cm^2$, which is smaller than expected from the electronic reconstruction model. The Ti $3d$ character of the charge carriers and the thickness of the conducting layer of only a few unit cells is measured using HAXPES and resonant inelastic x-ray scattering [178, 179]. The carrier density derived by HAXPES is higher compared to the one derived from Hall measurements, suggesting the presence of two types of carriers, namely localized and delocalized. Localized carriers are not accessible in transport. The existence of different subbands is also derived in DFT calculations [160]. Bert *et al.* link these two types of carriers to the coexistence of superconductivity and ferromagnetism [156]. Resonant PES and soft x-ray PES find in-gap states with a Ti $3d$ character in the STO [180, 181]. XAS measurements show that the degeneracy of the Ti $3d$ states is removed, making the Ti $3d_{xy}$ levels the first available states for conducting electrons [182].

However, care has to be taken when interpreting and comparing results of different groups. Small changes in the preparation conditions like substrate temperature or background pressure seem to have a tremendous influence on the sample properties. Brinkman *et al.* showed the influence of total oxygen pressure on the sheet resistance [155]. As shown in Fig. 4.3, the sheet resistance varies by several orders of magnitude.

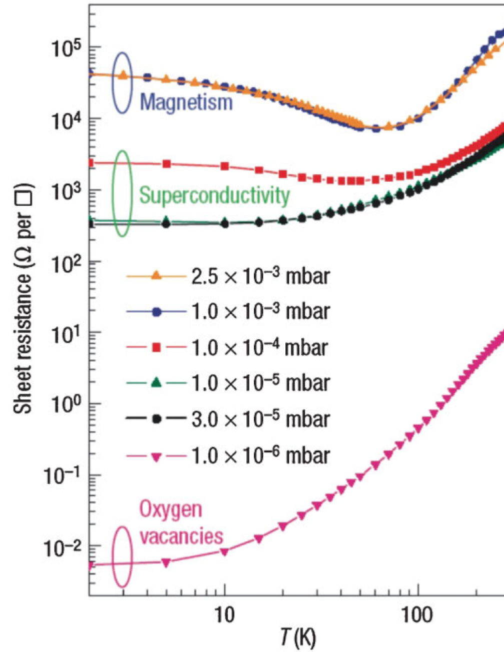

Figure 4.3: *Sheet resistance of LAO/STO: Dependence on the oxygen partial pressure taken from Brinkman et al. [155]. Accordingly, sample properties like magnetism or superconductivity strongly depend on the preparation conditions.*

For low resistances, the conductivity mechanism seems to be oxygen-vacancy-mediated as the same behavior can be found for oxygen-deficient STO [183]. For a higher growth pressure, sample properties tend to show magnetic or superconducting behavior. Dikin *et al.* reported the coexistence of ferromagnetism and superconductivity in their samples which were grown at a oxygen pressure of 10^{-3} mbar [16]. The ferromagnetism, they attribute to the Ti ions, the superconductivity to oxygen vacancies. Note that they did not apply any post-oxidation procedures.

Aruta *et al.* studied the changes in the plasma plume composition at different background pressures during the ablation of LAO and $LaGaO_3$ [184]. They find a dramatic drop in the kinetic energy of all plume constituents for a background pressure of 10^{-1} mbar at a target-to-sample distance of 50 mm. Furthermore, the plume particles start to react with the background gas at pressures higher than 10^{-1} mbar, which leads to the oxidation of the La atoms in the plume. Oxygen supply is not only given by the background gas, but also by the substrate as was discussed by Schneider *et al.* [107]. They used substrates containing ^{18}O and find high in- and out-diffusion rates for STO, while the diffusion rates in LAO were comparably low.

In this context, the influence of the total background pressure during the PLD process, which mainly determines the growth kinetics, and influence of the oxygen partial pressure, which primarily affects the oxygen stoichiometry, on the electronic interface properties, are studied in this thesis. To this end, samples were grown at different oxy-

gen partial pressures and additionally in a mixed O_2/Ar atmosphere. As some reports emphasize the importance of a post-oxidation procedure, the influence of this procedure was analyzed as well. Structural analysis was done by RHEED, AFM and XRD to verify the quality of the samples. Furthermore, STEM and EELS measurements were carried out to check for differences between the samples on a microscopic scale. HAXPES was applied to analyze the microscopic chemical and electronic structure of the interface and the results were contrasted with standard electric transport measurements providing information on the macroscopic interface properties.

4.3 $SrTiO_3$ substrate preparation

Conductivity in LAO/STO was only found when LAO is grown on TiO_2-terminated STO. Precisely controlling the surface termination is difficult, because for most perovskites the energetics for both terminations differ only slightly. STO, $NdGaO_3$ and lately also $DyScO_3$ are the only perovskite materials where the termination can be controlled accurately [185–187]. All STO substrates (Crystec, Germany) used throughout this work were treated according to the protocol given by Koster *et al.* [185]. To achieve a TiO_2 termination, substrates were cleaned with organic solvents followed by a 30-minute immersion in deionized water using ultrasound. This latter step causes the hydroxylation of SrO. The $Sr(OH)_2$ complexes were washed away by a 30-second rinse in NH_4-HF. Finally, the samples were annealed *ex situ* in a tube oven at 950° C in 150 ml/min flowing O_2 for 90 min.

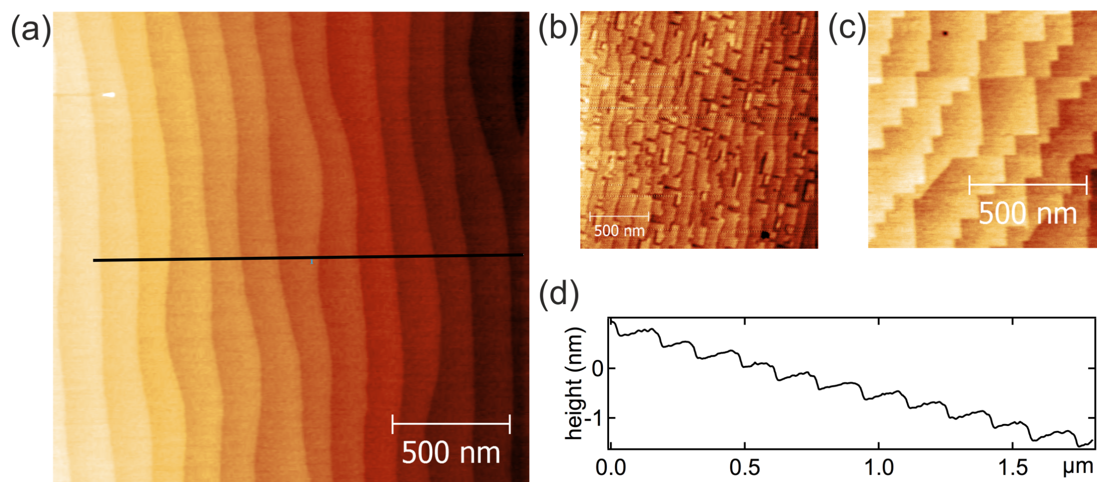

Figure 4.4: *AFM images of STO substrates: (a) with a perfect TiO_2 termination showing parallel steps. (b) and (c) with rectangular features at the step edges indicating a mixed termination. (d) height profile of the STO substrate shown in (a). The step height corresponds to the height of 1 uc.*

A typical AFM image of a treated STO substrate with a perfect TiO_2 termination is displayed in Fig. 4.4 (a). Characteristic is a terrace step height of one unit cell and

parallel step edges with only little wobbling. From the height profile shown in Fig. 4.4 (d) the average terrace step height is determined to be (0.4±0.1) nm, which corresponds to the out-of plane lattice constant of STO. Termination switches would lead to step heights of half a unit cell and a change in the friction force, which was not observed by AFM. For mixed or SrO-terminated surfaces the morphology changes and rectangular edges are observed as shown in Fig. 4.4 (b) and (c) [185, 188]. However, there is no established process to obtain a perfect SrO-termination. The standard way of achieving a SrO termination is growing one monolayer of SrO on TiO_2-terminated STO.

4.4 Film growth and structural characterization

All LAO/STO samples were grown by PLD in the MESA+ laboratory at the University of Twente. Growth conditions were as follows: the laser fluency was 1.3 J/cm^2, the laser frequency was 1 Hz and the substrate temperature was 850 °C. LAO was ablated from a single crystalline substrate (Crystec, Germany). The growth was monitored via RHEED with the oscillations of the (0,0) spot intensity being used to control the film growth. LAO thickness was varied between 2 uc and 6 uc. Special care was taken to control the oxygen partial pressure and the total growth pressure. Samples were grown at three different oxygen partial pressures, namely 10^{-1} mbar (HP), 10^{-3} mbar (MP) and 10^{-5} mbar (LP). For the samples grown in a mixed atmosphere, a certain oxygen partial pressure (e. g., 10^{-3} mbar, denoted by MP MIX) was applied, while Ar was used as inert gas to achieve the desired total pressure of 10^{-1} mbar. Post-growth oxidation (denoted by O) was done during cool-down at a temperature of 600 °C in pure oxygen atmosphere (400 mbar) for 1 h [17, 157].

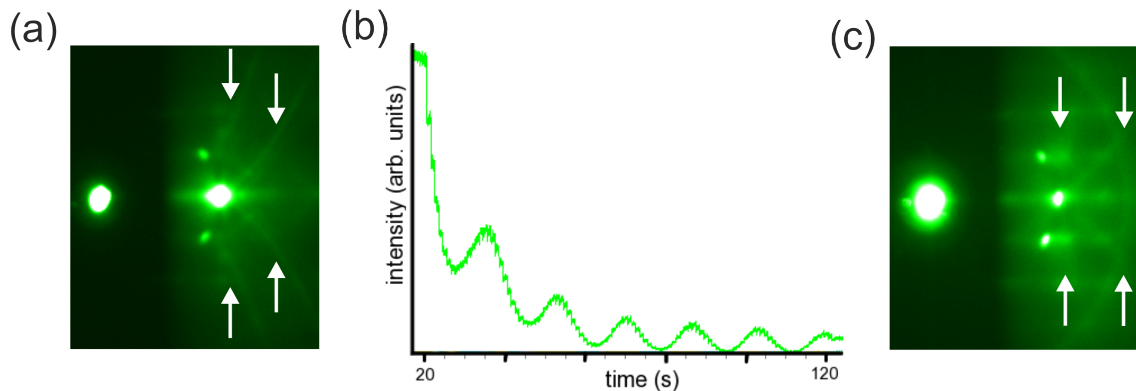

Figure 4.5: *RHEED (a) pattern of the substrate surface before growth, (b) oscillations during growth monitored for the (0,0) reflex indicating perfect layer-by-layer growth, and (c) pattern after the growth of the film. Marked are the Kikuchi lines in (a) and (c).*

A RHEED analysis typical of these samples is presented in Fig. 4.5. The RHEED pattern of the TiO_2-terminated substrate, which is shown in Fig. 4.5 (a), reflects the

smooth surface of the substrate. Strongly visible are the (0,0), (0,1) and (0,$\bar{1}$) Bragg spots, which lie on the first Laue circle. Additionally, the presence of the curved Kikuchi lines (marked in Fig. 4.5), which are only visible when the background noise is low, indicates a highly ordered and clean surface [34]. The oscillations of the spot intensity occurring during growth are shown in Fig. 4.5 (b). Six regular oscillations are observed, which point to perfect layer-by-layer growth [34]. Moreover, small intensity variations are visible on top of each oscillation. They are caused by the instantaneous deposition of a certain amount of *new* material and thus occur every second, corresponding to the laser repetition rate.* A growth rate of 16.6 pulses/uc was inferred. After growth, the 2D spots still dominate the RHEED pattern in Fig. 4.5 (c). Although the background noise is slightly enhanced and the pattern is a bit more streaky, the Kikuchi lines are still visible and stand for a well-ordered and perfectly flat film surface.

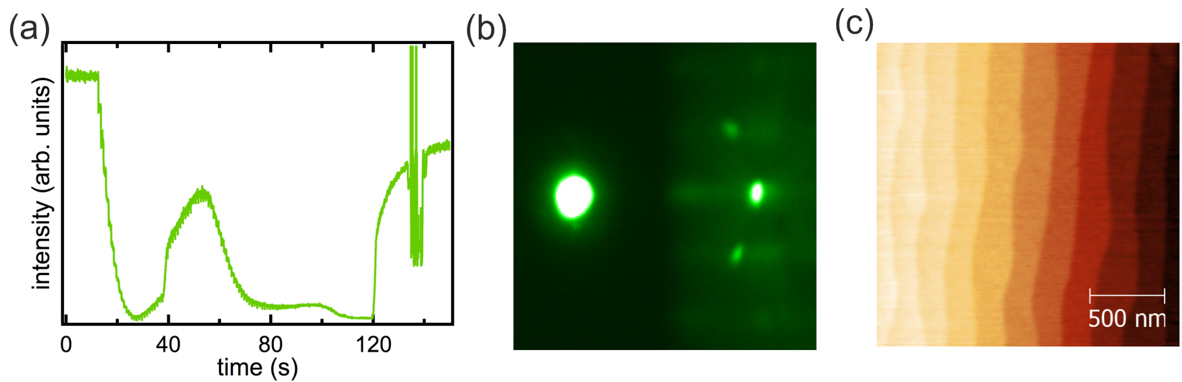

Figure 4.6: *RHEED and AFM characterization of growth at HP: (a) RHEED intensity showing no regular oscillations, (b) RHEED pattern after growth and, (c) AFM image showing a perfect 2D film surface. The AFM image is representative of all LAO/STO films of this study.*

The samples grown at a total pressure of 10^{-1} mbar are an exception in this context. No regular oscillations can be monitored during growth for these samples (see Fig. 4.6 (a)). The intensity starts to decrease, as is also the case for the other samples, but oscillations tend to die out rapidly and can not be linked to the formation of a monolayer. Nevertheless, the RHEED pattern of the film taken after growth, which is displayed in Fig. 4.6 (b), indicates a 2D surface with a comparably high quality. This is confirmed by the AFM image in Fig. 4.6 (c), which exhibits perfect single step terraces and a flat surface. The AFM image is representative of all LAO/STO films throughout this work. The lack of RHEED oscillations is most probably not caused by the increased attenuation of the electron beam at high pressures as the main spot still exhibits a comparably high signal-to-noise ratio [188]. It seems to be more likely that either the step density does not change during growth, which would point to a step-flow growth mode, or that there is a higher degree of disorder during growth, which hinders the observation

*Note that these jumps would not be present for MBE growth, as the material flux is constant.

of the oscillations. Higher disorder may be caused by changes in the plasma plume composition, namely the loss of kinetic energy and the oxidization of the particles according to the observations of Aruta *et al.* [184]. This would also influence the nucleation on the substrate.

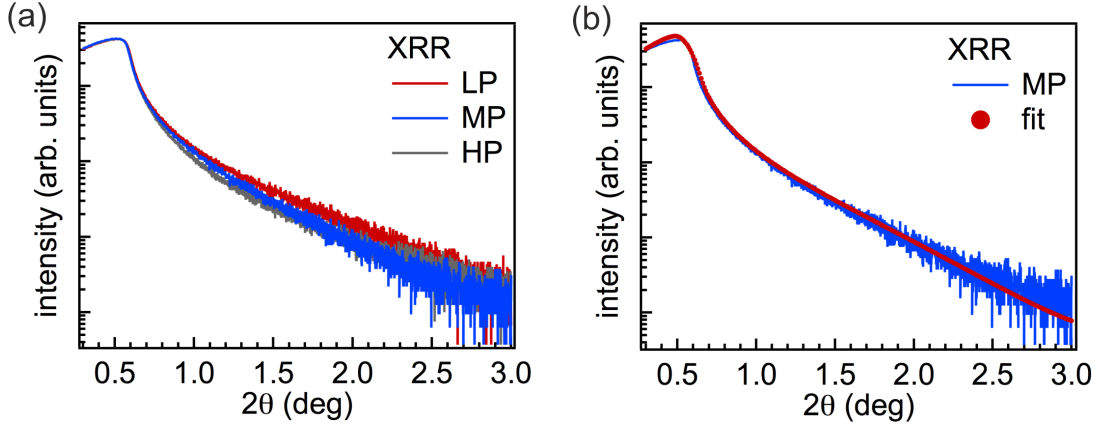

Figure 4.7: *(a) X-ray reflectivity measurements of the LP, MP and HP LAO/STO films confirm the thickness of the film grown at HP. (b) XRR spectrum and spectral fit of the MP sample. A thickness of (6.0±0.5) uc is derived.*

Growth rates for all films fabricated at 10^{-1} mbar were calibrated by the samples grown at a lower pressures, and thicknesses were confirmed by XRR. In Fig. 4.7 (a), XRR scans for the LP, MP, and HP samples are displayed. As the thickness of the films is only 6 uc, strong oscillations, as were observed for the thick Fe_3O_4/ZnO films shown in Sec. 3.6.1, cannot be expected since their period and intensity directly scale with the thickness. However, the curves show only little variation, which confirms a similar thickness of all films. A representative fit is exemplarily shown in Fig. 4.7 (b) for the MP sample. Best fit parameters give a film thickness of 6.0±0.5 uc, and a surface and interface roughness of <2 uc. Furthermore, the film thickness was confirmed for all samples grown at different pressures by STEM analyses.

4.5 Transmission electron microscopy and electron-energy loss spectroscopy

The microscopic properties of the samples were studied using scanning transmission electron microscopy (STEM) and electron-energy loss spectroscopy (EELS). Measurements were carried out by the group of J. Verbeeck at the Institute for Electron Microscopy for Materials Research at the University of Antwerp. Details on the technique can be found elsewhere [189, 190]. Quality checks of LAO/STO by STEM are commonly done throughout the literature [154, 158, 191]. For high-quality heterostructures, an abrupt interface together with a comparably low intermixing ratio was found. A general drawback

of STEM is that light elements cannot be imaged due to their low mass. This drawback was overcome by Jia *et al.* using aberration-corrected ultra-high resolution transmission electron microscopy [1]. Cross-sectional EELS can give spatially resolved information on the atomic composition and their valence states. The results for LAO/STO differ strongly in the literature, going from the observation of a Ti^{3+} layer near the interface [158], which even depends on the growth pressure [173], to no changes of the Ti valence state near the interface [192].

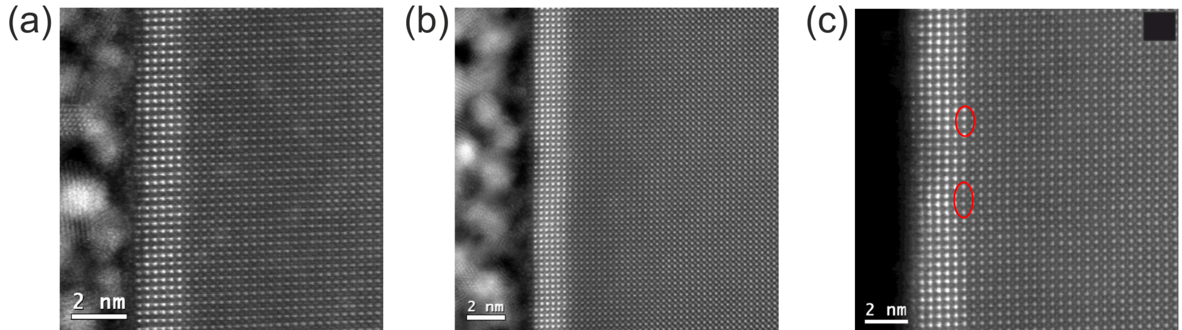

Figure 4.8: *HAADF-STEM: (a) LP, (b) MP, and (c) HP samples showing epitaxial quality and a thickness of 6 uc for all films. The red circles in (c) highlight the atomic rows which are less intense and hint at a higher intermixing ratio.*

The high angle annular dark field (HAADF) STEM images of the LP, MP and HP samples are displayed in Fig. 4.8 for a comparison. For STEM images taken in the HAADF mode, the brightness I of the atoms on a black background increases with the nuclear charge number ($I \approx Z^2$) [193]. The viewing direction is parallel to the [001] direction of the STO. Going from left to right one observes in Fig. 4.8 (a) at first an amorphous platinum layer, which is deposited during the preparation of a lamella, followed by the sample itself. For the HP sample, an additional carbon layer was deposited on the film surface (see Fig. 4.8 (c)), as this reduces the surface damage compared to the direct deposition of platinum. For all three films, one can clearly differentiate the LAO film from the STO substrate with La and Sr giving the strongest contrast of the film and the substrate due to the HAADF technique used. Disregarding the surface quality, which is strongly influenced by the deposited platinum and carbon, all films are coherently strained to the substrate forming a sharp interface with no obvious defects or dislocations. Furthermore, the film thickness proved to be identical for all samples. Both the LP sample in panel (a) and the MP sample in panel (b) exhibit darker and brighter patches in the STO itself, which could be caused during the preparation of the lamella or by an additional carbon contamination. The red circles at the interface region of the HP sample in Fig. 4.8 (c) indicate atomic rows with a higher intensity variation not present in the other two samples. This could be a sign for an enhanced intermixing ratio or for roughness at the interface.

Intensity cross-sections of the HAADF images, which were integrated parallel to the

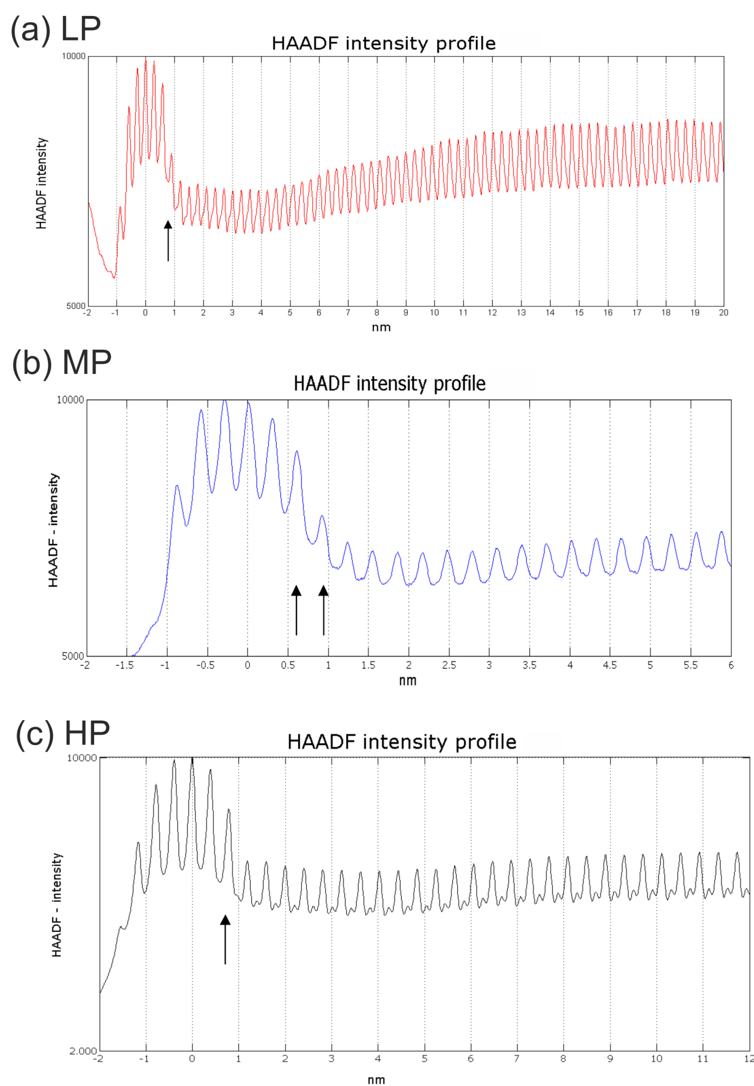

Figure 4.9: *Intensity cross-sections of the images displayed in Fig. 4.8: (a) LP, (b) MP, and (c) HP samples. The interface appears to be less sharp for the MP sample. A drop of intensity is present for all samples in the substrate near the interface.*

interfaces, are presented in Fig. 4.9 for all three samples. The strongest peaks could be identified to originate from the La atoms in the film and the Sr atoms in the substrate. Note that the cross-section for the LP sample in panel (a) is taken for a wider range, i. e., reaches deeper into the STO. For all samples an intensity variation is present in the substrate itself, which is most pronounced for the LP sample. The overall intensity drops going from the substrate deep in the bulk to the interface region (12 -2 nm), while the sharpness and the signal-to-noise ratio for the Sr atoms is not affected. The intensity decrease results from a 'darker' region within the substrate which can also be seen in Fig. 4.8 (b). The origin of this layer has not yet been understood. On the one hand, it could be caused by the fabrication process of the lamellae, by either the thinning of the sample or the deposition of the platinum. On the other hand, it could be a hint for strain effects originating from the film reaching into the substrate. If this was the case, these effects have to be taken into account when interpreting the macroscopic sample properties. Furthermore, the arrows in each image label the atoms that cannot be attributed to either La or Sr. This gives a certain measure for the interface sharpness which is best for the LP and the HP sample. For the HP lamella, there are also Ti atoms visible showing up as small bumps in between the Sr atoms. The Ti atoms cannot be observed for the other two samples due to a slight misalignment during the measurement.

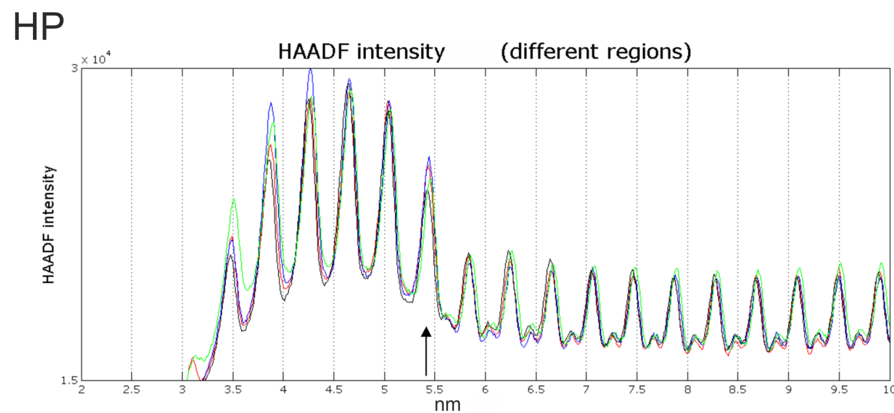

Figure 4.10: *Intensity cross-sections recorded at different spots for the HP sample. Although the intensity profiles of the substrate are virtually identical, variations can be seen within the film pointing to a higher degree of disorder.*

For the HP sample, intensity cross-sections of different regions in the STEM image are shown in Fig. 4.10. While within the substrate the intensity is virtually identical, there are strong variations within the film for different cross-sections. As the signal is produced by a column of La atoms that is perpendicular to the cross-sections, this indicates a higher degree of disorder or missing La atoms in these columns. As Al atoms are not visible, speculations on the La/Al ratio cannot be made at this point. Nevertheless, it is in line with the absence of RHEED oscillations for this film and support the above conjecture of an enhanced degree of disorder within the film for the HP sample.

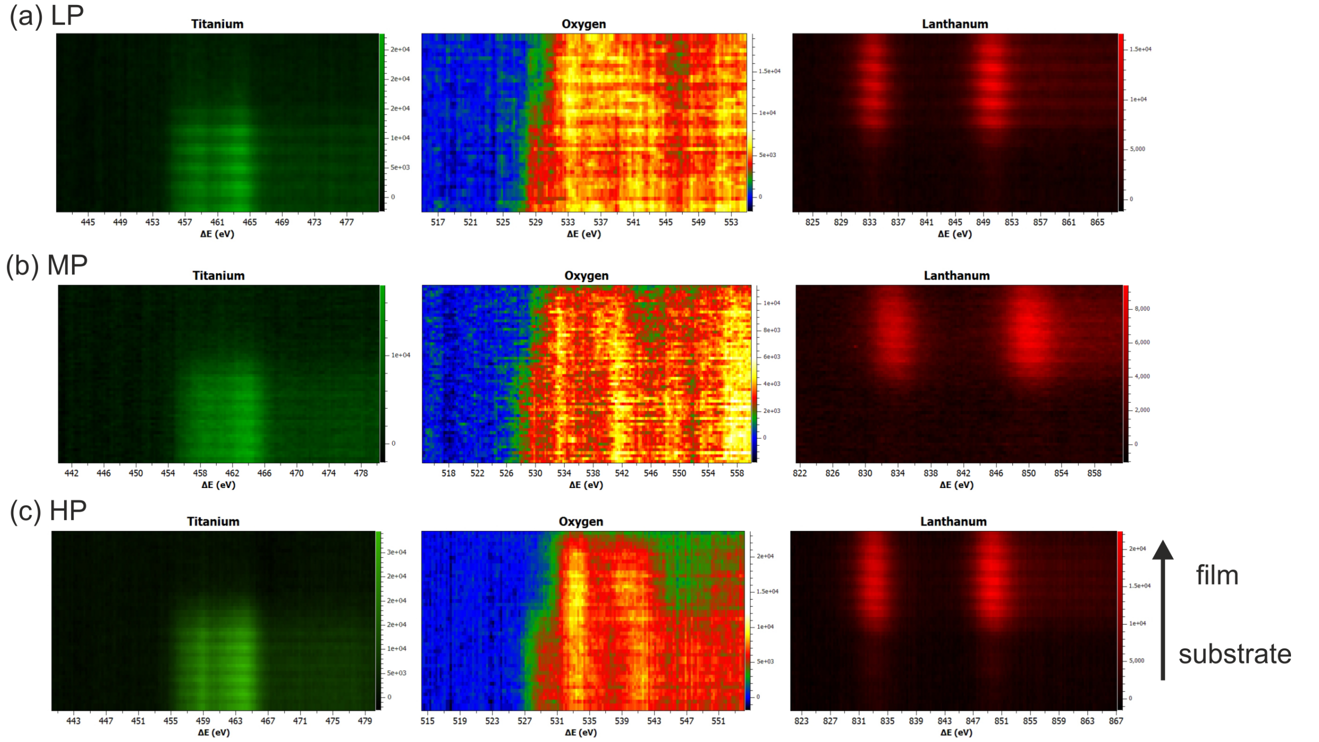

Figure 4.11: *Electron-energy loss spectra at the Ti L-, O K-, and La M-edges for (a) LP, (b) MP, and (c) HP samples.*

STEM-EELS measurements were performed by scanning across the interface with atomic resolution. A graphical representation of the Ti $L_{2,3}$-, O K-, and La $M_{4,5}$-edges going from left to right is shown in Fig. 4.11. The energy resolution is about 1 eV. Note that the color scale is not absolute, which hinders a sample-to-sample comparison. The purpose was to characterize the sharpness of the interface and the diffusion for the individual atoms. The edge onsets from the literature are 455 eV, 532 eV and, 832 eV for Ti $L_{2,3}$, O K, and La $M_{4,5}$, respectively. The stripy pattern which can be observed for all samples and all loss lines is due to the scanning direction being perpendicular to the interface. For all samples, some La and Ti interdiffusion was observed, being in the range of 1 uc in both cases. The Ti diffusion is less for the HP sample. When trying to relate the changes in growth pressure to intermixing ratios, no clear trends between the samples can be seen.

In Fig. 4.12, the Ti $L_{2,3}$-edge is displayed for the MP sample. Spectra were taken using a monochromator with an energy resolution of ~ 0.55 eV at three different points: near the LAO film (red), deep in the STO substrate (blue) and in between (green). All spectra are virtually identical. The spectra exhibit four peaks being a fingerprint for the 4+ valence state of Ti. Note that near the interface within the resolving power of TEM-EELS no Ti^{3+} can be observed either. This is in line with Ref. [192] for samples that were prepared using the same recipe.

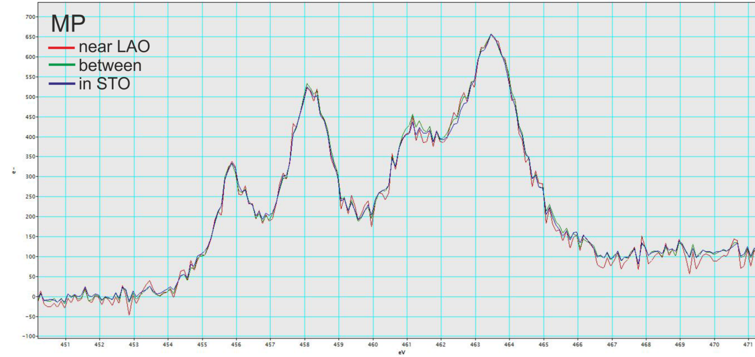

Figure 4.12: *Electron-energy loss spectra at the Ti $L_{2,3}$-edge of the MP sample. Three spectra were recorded at different distances to the interface. No indications for Ti^{3+} can be observed.*

Maurice *et al.* investigated samples grown at different growth pressures, namely 10^{-6} mbar and 0.4 mbar [173]. They found 3D relaxation mechanisms in the high-resolution TEM images of the 0.4 mbar sample, which ended in island growth clearly visible in AFM as well. However, this cannot be observed for the HP sample under investigation in this study, neither by means of STEM nor AFM. Kalabukov *et al.* carried out medium-energy ion spectroscopy (MEIS) and STEM on samples grown at 10^{-4} mbar and $5{\cdot}10^{-2}$ mbar [177]. By analyses of intensity cross-sections, they find a lower intermixing ratio together with a sharper interface for the sample grown at a higher pressure. Furthermore, they find a higher background intensity for the LAO which is grown at high pressure, which could be interpreted as a higher degree of disorder in the film. The studies of Jia *et al.* go beyond the analyses of the samples presented in this chapter [1]. They find a rotation of the oxygen octahedra not only in the LAO, but also in the interface-near layers of the STO, giving rise to a ferroelectric dipole moment for samples grown at 10^{-3} mbar. Further analyses in this direction may reveal whether the theory regarding the polarization of STO due to induced octahedral rotations by LAO are at play.

In summary, the studies show that all samples are grown epitaxially and no larger disorder or second phase formation can be observed when LAO is grown in the pressure range of 10^{-1}-10^{-5} mbar. Furthermore, it seems that some interdiffusion is always present for these heterostructures. A differentiation between the samples is difficult; however, a higher degree of disorder in the film compared to the substrate may be present in the HP samples found in the STEM cross-sections.

4.6 Extrinsic and intrinsic interface effects

To further investigate the interfacial properties of the samples grown under different conditions, van-der-Pauw conductivity measurements were carried out using a standard four-probe cryostat [194]. These measurements were compared to bulk sensitive HAX-

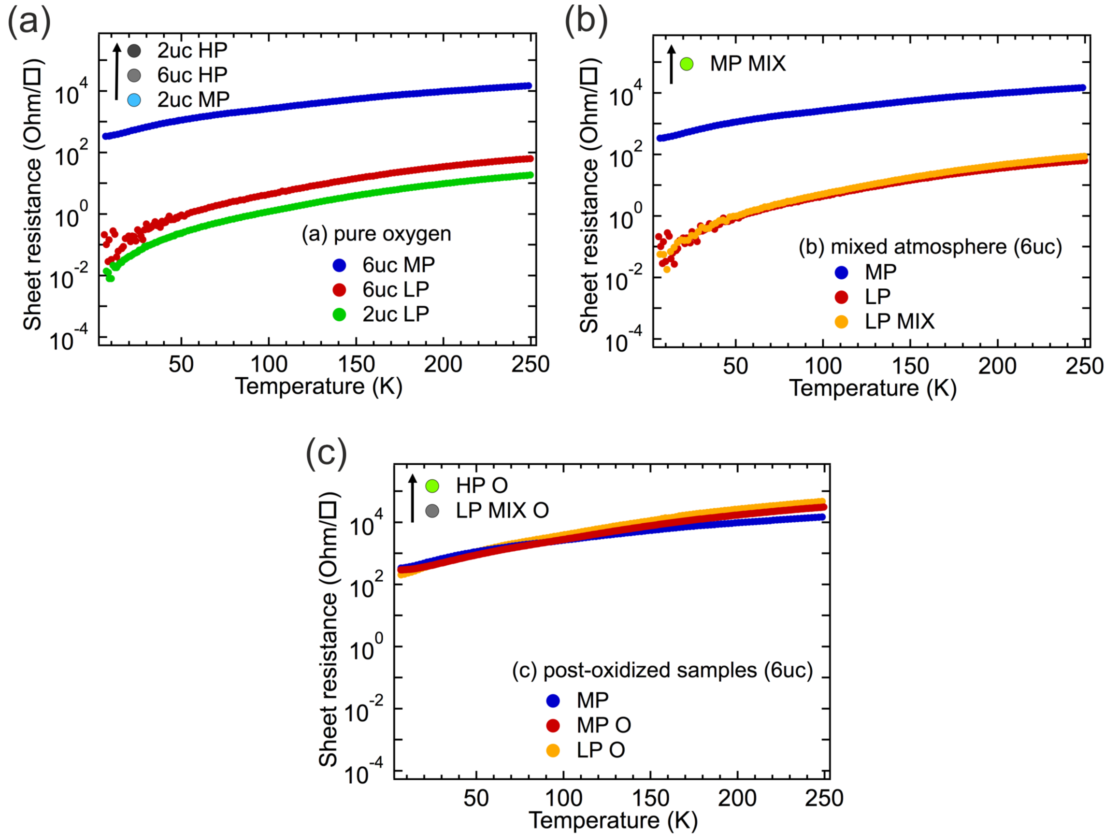

Figure 4.13: *Conductivity of LAO/STO thin films grown (a) in pure oxygen atmosphere, (b) in a mixed O_2/Ar atmosphere, and (c) of post-oxidized samples. For further explanations see text.*

PES measurements which proved to give valuable information on the chemical structure of buried layers and interfaces [48, 178]. A detailed analysis of the core-levels allows for an identification of the atoms that host possible extra charge carriers. In contrast, the valence band is formed by the orbitals of all elements in the heterostructure, which makes a detailed identification of the charge-hosting element more difficult. In the case of LAO/STO, additional electrons in the STO lead to a valence change of the Ti ions from 4+ to 3+. This valence change results in a chemically shifted Ti $2p$ doublet for emission from the Ti^{3+} states. The HAXPES measurements were carried out at beamline BW2 at HASYLAB (DESY), Hamburg [195]. The resolution was determined from the Au $4f$ core-levels to be $\Delta E < 0.6$ eV for the used photon energy of 3.5 keV. All samples were measured without any surface preparation at room temperature.

Pure oxygen atmosphere

The influence of the oxygen partial pressure for samples grown in pure oxygen at pressures of 10^{-1} (HP), 10^{-3} (MP), and 10^{-5} mbar (LP) was analyzed. The strong effect on

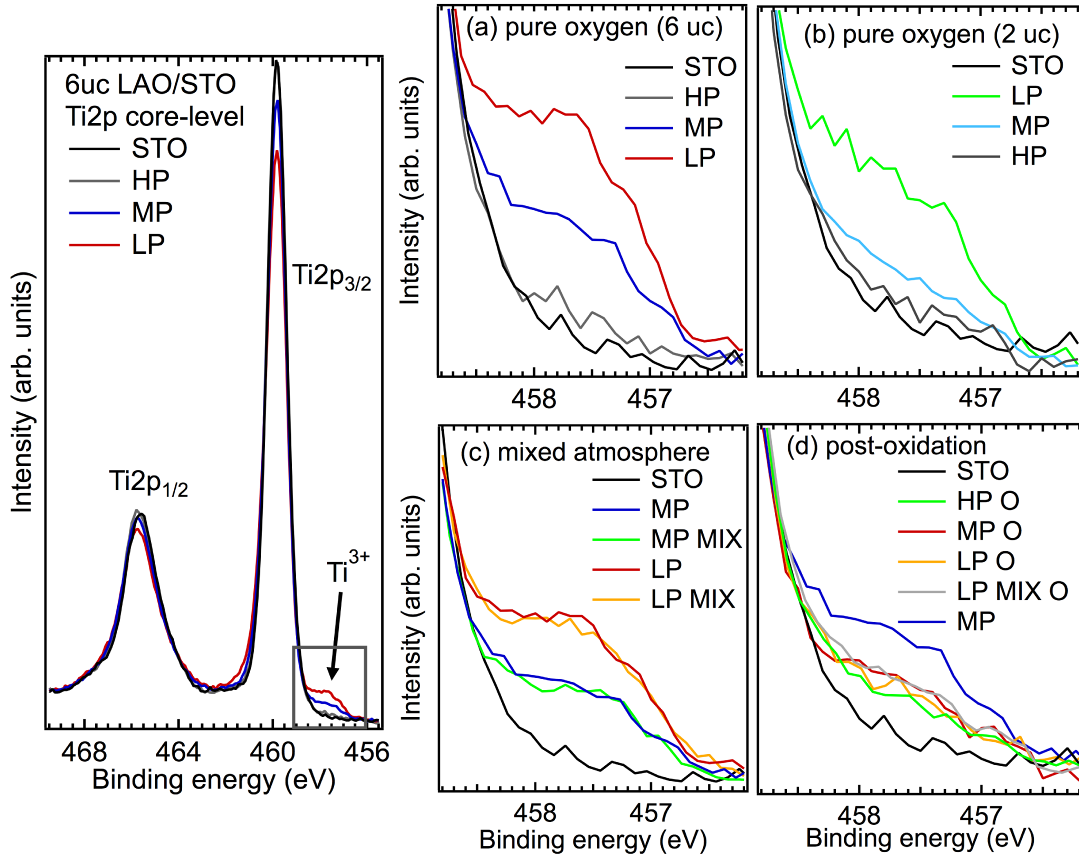

Figure 4.14: *HAXPES of LAO/STO thin films; the left panel shows the entire Ti 2p spectra. The right panels show a close-up to the Ti^{3+} region of the Ti $2p_{3/2}$ peak for samples grown (a) in pure oxygen atmosphere (6 uc LAO/STO), (b) in pure oxygen atmosphere (2 uc LAO/STO), (c) in a mixed O_2/Ar atmosphere (6 uc LAO/STO), and (c) post-oxidization of 6 uc LAO/STO samples. Further explanations see text.*

the conductivity becomes obvious from Fig. 4.13 (a). The MP samples exhibit a critical thickness regarding conductivity, i. e., the 2 uc sample is insulating while the 6 uc sample is metallic. The conductivity is within the range given also by other groups for high-quality LAO/STO samples [17, 155]. The HP samples are insulating independently of their thickness. In contrast, LP samples are highly conductive for any thickness. Note that the conductivity is four orders of magnitude higher compared to the MP samples. The transport data is now contrasted to the Ti $2p$ core-level data. The entire spectrum is shown in the left panel of Fig. 4.14, exhibiting the spin-split $2p_{1/2}$ and $2p_{3/2}$ peak at energies of 465.6 eV and 459.9 eV, respectively. On the lower binding energy side a small structure is visible corresponding to the chemically shifted Ti^{3+} component (ΔE=2.2 eV) of the $2p_{3/2}$ peak. This feature is also present for the $2p_{1/2}$ peak, but as the intensity scales with the respective Ti^{4+} $2p_{1/2}$ peak, it is hardly visible. Any further discussion of the HAXPES data will be based on the intensity of the Ti^{3+} $2p_{3/2}$ peak,

which is shown for the 6 uc and the 2 uc samples in Fig. 4.14 (a) and (b), respectively. For comparison, a STO reference that exhibits only Ti in the 4+ valence state is shown as well. The contribution of Ti^{3+} scales in inverse proportion to the growth pressure. Independently of the thickness, both the 2 uc and the 6 uc LP sample exhibit a larger amount of Ti in the 3+ valence state. This is probably due to the higher amount of O vacancies that provide the electrons in these samples, seen in both transport and HAXPES. The HP samples are insulating and exhibit little to no Ti^{3+}, independently of the overlayer thickness. In the case of the MP samples, the Ti^{3+} intensity strongly depends on the overlayer thickness, being reduced for the 6 uc film compared to the LP samples, but stronger for the 2 uc samples compared to the HP samples. The finding of Ti^{3+} in the insulating samples grown at MP may point to the presence of localized carriers in the MP samples, which cannot be detected in transport [156, 160]. Going from the thickness-dependent conductivity of the MP samples to an overlayer-independent conductivity of the LP samples, it can be concluded that at least two different mechanisms are effective in the generation of conductivity for these two pressure regimes.

Maurice *et al.* and Aruta *et al.* also found samples to be insulating when grown at 0.4 mbar and at 10^{-1} mbar, respectively [173, 184]. Maurice *et al.* explained this with structural defects in the film, which would result in an enhanced surface roughness, whereas Aruta *et al.* discussed changes in the plasma plume as a possible explanation for a higher disorder in the film. From our RHEED patterns and AFM images we cannot confirm a higher surface roughness of our samples in general. However, the lack of RHEED oscillations and the STEM images for films grown at high pressures could indeed hint at a somewhat distorted film structure. In contrast, Aruta *et al.* found samples grown at about 10^{-2} mbar to be conducting [196]. However, in this case, the sample-to-target distance was lowered from commonly >50 mm to about 30 mm. Reducing the sample-to-target distance counteracts the effects of the high growth pressure, namely the enhanced oxidization of the plume constituents and the enhanced loss of kinetic energy of the plume particles.

High-pressure growth in mixed atmosphere

To disentangle the effects of the oxygen partial pressure and the total growth pressure, samples were grown in a mixed O_2/Ar atmosphere. The oxygen partial pressure was chosen to be 10^{-3} mbar (MP MIX) and 10^{-5} mbar (LP MIX). The total pressure of 10^{-1} mbar was achieved by backfilling the PLD chamber with Ar. In Fig. 4.14 (c), HAXPES spectra of samples with a 6 uc thick LAO overlayer, grown either in pure oxygen or in a mixed atmosphere at the same O_2 partial pressure, are compared. The Ti^{3+} parts of the spectra, corresponding to the same O_2 partial pressure but to a different total pressure, lie on top of each other. Apparently, the amount of Ti^{3+} only depends on the oxygen partial pressure and with that on the oxidation potential during the deposition. However, an equivalent statement does not hold when it comes to the sheet resistances. On the one hand, the resistance curves of the LP MIX and the LP samples are con-

gruent in Fig. 4.13 (b) and exhibit both metallic behavior. On the other hand, the MP MIX sample is insulating, whereas the MP sample is metallic. It should also be noted that the resistances of the LP samples are several orders of magnitude lower than the resistance of the conducting MP sample, while the amount of Ti^{3+} of the LP compared to the MP sample varies by a factor of about 1.5 only. Thus, it can be concluded that it is essentially the oxygen partial pressure that controls the amount of charge carriers in this regime, but that the number of charge carriers does not alone determine the electric transport properties. The oxygen partial pressure may affect the amount of oxygen vacancies in the 'bulk' STO substrate, the STO substrate surface, and the LAO film. The influence of the total pressure on plume and growth kinetics is restricted to the STO substrate surface and the LAO film. Thus, it is plausible to assume that the thickness of the conducting region is different for the LP/LP MIX and the MP/MP MIX samples. In the case of the LP samples, the conducting zone apparently reaches from the interface well into the STO substrate, being insensitive to all effects which are restricted to interface and overlayer and controlled by the total pressure. If this is due to oxygen vacancies in the entire STO substrate, the discrepancy between the measured Ti^{3+} in spectroscopy and the carrier density in the Hall data will be caused by the finite probing depth of HAXPES (see Tab. 4.1). In contrast, the charge carriers contributing to transport are confined to the interface region of the STO substrate for the MP samples. Here, the conductivity does not simply scale with the amount of charge carriers, but is strongly influenced by other factors which might be intrinsic or extrinsic in nature such as a modified electronic structure at the interface or any kind of defects. The latter apparently applies to the non-conducting MP MIX samples where the interface roughness may be slightly enhanced and the overlayer somehow distorted due to the growth at a high total pressure of 10^{-1} mbar. From this series it can be concluded that it is mainly the high background pressure and with that the growth kinetics that destroys interface conductivity.

Post-oxidation

The results of post-oxidation (O) on sheet resistance and on Ti^{3+} spectral weight are displayed in Fig. 4.13 (c) and Fig. 4.14 (d), respectively. Regarding the latter, the salient observation is that independently of the treatment history, all samples show the same amount of Ti^{3+} after post-oxidation. Note that this Ti^{3+} amount is reached in both directions, i. e., by an increase or by a decrease of the initial Ti^{3+} amount present in the non-oxidized samples. The fact, that it is distinctly more than in the HP sample is all the more striking, because the O_2 partial pressure during post-oxidation exceeds the highest growth pressure by more than three orders of magnitude, while the temperature is only moderately reduced to 600°C. This can be taken as a strong hint that the applied post-oxidation step leads to a thermodynamically metastable state and that the procedure can thus be used to remove the arbitrariness in controlling the electronic interface properties by the oxygen partial growth pressure. Note that the Ti^{3+} amount is close to but

Table 4.1: *Ti^{3+}/Ti^{4+} ratios derived by HAXPES spectra analyses, carrier density and mobility derived by Hall measurements for 6 uc LAO/STO films. The conductivity values were measured at a temperature of 170 K.*

	pure O_2			
pressure [mbar]	HP		MP	LP
$I(Ti^{3+})/I(Ti^{4+})$	0.03		2.4	4.0
resistance [Ω/□]	—		$3.8 \cdot 10^3$	21.2
mobility [cm/V·s)]	—		26.1	57.5
carrier density [cm^{-2}]	—		$8.1 \cdot 10^{13}$	$7.9 \cdot 10^{15}$
	MIX atmosphere			
pressure [mbar]	MP MIX	LP MIX		
$I(Ti^{3+})/I(Ti^{4+})$	1.6	3.7		
resistance [Ω/□]	—	27.4		
mobility [cm/V·s)]	—	80.7		
carrier density [cm^{-2}]	—	$4.8 \cdot 10^{15}$		
	post-oxidation			
pressure [mbar]	HP O	LP MIX O	MP O	LP O
$I(Ti^{3+})/I(Ti^{4+})$	0.2	0.7	0.5	0.4
resistance [Ω/□]	—	—	$11 \cdot 10^3$	$16 \cdot 10^3$
mobility [cm/V·s)]	—	—	19.4	17.5
carrier density [cm^{-2}]	—	—	$1.6 \cdot 10^{13}$	$9.7 \cdot 10^{12}$

smaller with respect to the non-oxidized MP sample and comparable to the value found for samples grown by the Augsburg group [17, 178]. In transport, all samples exhibit virtually the same temperature-dependent sheet resistance after the post-oxidation step except for those grown at a high total pressure (be it in pure oxygen or in a mixed Ar/O_2 atmosphere). These findings are in line with the above-mentioned conjecture that at high pressures some kinds of defects, e. g., an enhanced interface roughness or dislocations [197] due to growth kinetics, are induced, which then cannot be removed by annealing under oxygen. Among the possible defects, point defects like oxygen vacancies, which should be healed out, or La-Sr intermixing, which should be even enhanced by interdiffusion in the post-oxidation step and hence should also affect the samples grown at low or medium total pressures, i. e., the LP and MP samples, can be excluded.

Discussion

An overview of all results is given in Tab. 4.1. The Ti^{3+}/Ti^{4+} ratio is determined by HAXPES in normal emission geometry. Values for conductivity and carrier density are given for a temperature of 170 K. The Ti^{3+}/Ti^{4+} ratios show the same trend as the sheet carrier density. A high carrier density comes along with a high Ti^{3+}/Ti^{4+} ratio. Note that for all samples where oxygen vacancies may play the dominant role the carrier density is as high as $10^{15}\,\mathrm{cm}^{-2}$, a value which is commonly found for oxygen-deficient STO. At this point all findings shall be restated in a compact form in such a way that they can also be read as general rules of how to control the electronic interface properties by means of the growth pressure.

- A critical thickness for the samples grown in pure oxygen is only observed in transport for the MP samples. The LP samples are always conducting, while the HP samples are always insulating.

- Post-oxidation leads to the same behavior both in transport and in HAXPES, except for the samples grown at a high total pressure.

- All MIX samples show the same behavior in conductivity and in the amount of Ti^{3+} spectral weight as their counterparts grown in pure oxygen, except for the MP and MP MIX samples with 6 uc LAO for which the former is conducting, the latter insulating.

- For the HP samples grown in pure oxygen, the Ti^{3+} spectral weight is almost completely suppressed.

- Remarkably, post-oxidation leads to virtually the same charge carrier concentration for all samples as inferred from HAXPES.

The occurrence of a critical thickness for the conducting interface, for whatsoever reason it may happen, shall be considered as a key property of these samples. Its absence for the LP samples, their comparably low sheet resistance, and their highest Ti^{3+} spectral weight among all samples is readily explained by a high concentration of oxygen vacancies, which reaches relatively deep into the STO substrate and can be assumed to be a purely extrinsic effect [201].

More interesting is the finding of the insulating behavior in transport for growth at a high growth pressure, i. e., for the HP, MP MIX and the LP MIX O samples. Note that for the two latter samples a finite amount of charge carriers could be identified by HAXPES. The main difference here is the oxidation potential within the plume, while growth kinetics are the same. Thus, sample properties seem to be altered by a change of the growth kinetics at 10^{-1} mbar, most probably owing to the enhanced deceleration of the particles in the plasma plume. These changes in growth kinetics seem to influence film properties in such a way that macroscopic conductivity is hindered although charge

carriers are present. This is supported by the RHEED and STEM findings, i. e., by a higher degree of disorder in these samples.

Additionally, the almost complete absence of the Ti^{3+} spectral weight in the HP case indicates an absence of charge carriers, may they be localized or delocalized. However, the structural properties, e. g., the polar character, are the same for the HP, MP MIX, and LP MIX O sample. This absence of charge carriers may be explained by the suppression of donor impurities or vacancies in the LAO film or surface. This would mean that for the electronic reconstruction to become effective, a charge reservoir of an extrinsic nature is needed which might be provided by, e. g., oxygen vacancies in the LAO overlayer [166, 202], and can be depleted by growth at high oxygen partial pressures.

Post-oxidation seems to be highly important for the formation of a conductive interface layer and removes all the effects originating from low pressure growth (cf. sample LP O). In contrast to the supply of too much oxygen during growth, conductivity is not destroyed by this procedure, concluding that this metastable state is essential to further study the purely intrinsic effects of these specimens.

4.7 Summary and outlook

The influence of the growth conditions on the interface properties of LAO/STO heterostructures was systematically studied. Structural analyses by means of RHEED, AFM and STEM verify similar film properties for all growth conditions, except a too high total pressure leads to a somewhat distorted film structure. A comparison of HAXPES measurements and conductivity measurements reveal that it is the oxygen partial pressure during growth that determines the amount of charge carriers in the STO, while it is the total growth pressure that determines the macroscopic sample properties. Thus, a too high growth pressure destroys interface conductivity mainly due to the growth kinetics that most probably lead to a distorted film structure. Interface conductivity above a critical overlayer thickness is found for samples either grown at a medium oxygen partial pressure or treated by post-oxidation, the latter leading to a metastable state. Oxygen vacancies originating from an insufficient supply during growth are refilled by the post-oxidation procedures, nevertheless the effects of a too high total pressure, namely a change of the growth kinetics, cannot be counteracted.

Although a critical thickness is observed for growth at a medium oxygen pressure and for post-oxidized samples, differences in the amount of charge carriers and the total resistance are observed. This may offer a good starting point for future experiments addressing questions like the role of localized and delocalized charge carriers as well as the occurrence of superconductivity and ferromagnetism.

5 $LaVO_3/SrTiO_3$ – electrostatic doping of a Mott insulator

Abstract

LVO/STO heterostructures show congeneric behavior compared to LAO/STO regarding a thickness-dependent conductivity, most likely explained by an electronic reconstruction. Unlike LAO, which is a wide band gap insulator, LVO is a strongly correlated system, which has an antiferromagnetic Mott insulating ground state. Heterostructures were grown by means of pulsed laser deposition and structural properties as well as phase purity were verified by several methods. Hard x-ray photoelectron spectroscopy studies show a charge accumulation near the interface on the LVO side for conducting samples. This means, that a band-filling-controlled metal-insulator transition by pure electrostatics is achieved without suffering from chemical impurities. Multiplet calculations and a comparison to single crystal spectra are presented to determine the precise valence state of vanadium in LVO/STO, but without yielding consistent results. Finally, a band diagram is proposed, which shows a slight band offset of the valence bands at the interface and an upward bending in the STO towards the interface.

5.1 Introduction

The striking observation of a 2DES in LAO/STO triggered enormous efforts to explore other systems for similar behavior. If the electronic reconstruction picture is correct, the growth of other polar perovskites on non-polar materials like STO should also lead to conductivity at the interfaces. While the interface of $LaCrO_3/SrTiO_3$ turns out to be insulating, most probably due to cation intermixing, the interface of $KTaO_3$/STO shows n-type conductivity [203, 204]. However, $KTaO_3$ has a negative polarization (compared to LAO) which in principle should lead to p-type interface conductivity. Interfaces of $LaGaO_3$/STO, $GdTiO_3$/STO, and LVO/STO exhibit n-type conductivity and thus support the picture of the electronic reconstruction [19, 205, 206]. While $LaGaO_3$ is a band insulator, $GdTiO_3$ and LVO are Mott insulators and are therefore interesting for studying the physics of correlated materials. As far as photoemission is concerned, $GdTiO_3$ exhibits the drawback that Ti is present in different valence states in both the film and the substrate. Hence, no chemical contrast can be exploited to study a possible charge reordering and interface effects. In LVO/STO there are two different

B-cations. Furthermore, the vanadium and the titanium atoms are multivalent, i. e., both have the ability to host extra electrons. This, together with the small Mott gap of only 1.1 eV, makes this system exceedingly interesting, because in the picture of an electronic reconstruction it is *a priori* not clear where the electrons will go to [207].

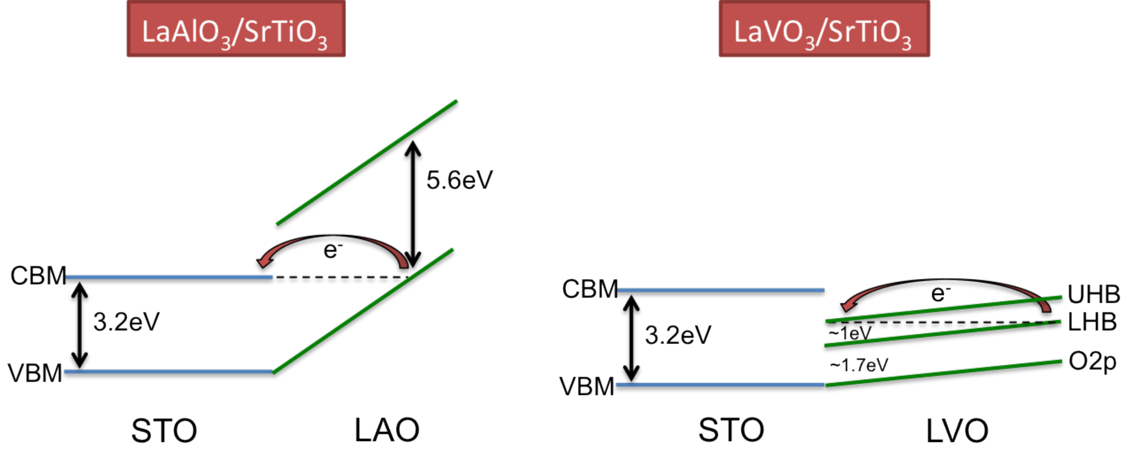

Figure 5.1: *Potential build-up and possible charge transfer in LAO/STO and LVO/STO. Band alignment considerations suggest a charge transfer into the substrate material for LAO/STO. In contrast, a charge transfer within the film material seems to be more favorable in the case of LVO/STO.*

The schematic depiction shown in Fig. 5.1 illustrates the different scenarios comparing the band pictures of LAO/STO and LVO/STO. Note that this picture is simplified as the exact band alignment is far from clear and the alignment of the valence band maxima at the interface is assumed. In the case of LVO, this is denoted by 'O 2*p*'. For LAO the transfer of (in the ideal case) 0.5 e^- per 2D unit cell is energetically more favorable, if the valence band maximum at the surface of the LAO crosses the conduction band minimum of the STO. For this to happen the potential build-up has to be big enough to overcome the band gap of STO. In contrast, for LVO/STO the smaller Mott gap of LVO might play the essential role and electron transfer may happen from the lower Hubbard band at the surface to the upper Hubbard band at the interface within the LVO overlayer itself. This would lead to the rather interesting situation of an electrostatically doped interface at the LVO side. A population of the interfacial V 3*d* states may result in a filling-controlled Mott transition, without the impurity potential introduced by chemical dopants.

In this chapter, spectroscopic evidence is presented that supports the model explained above. LVO/STO films were grown with various LVO thicknesses for both types of interfaces. A thorough analysis of the growth and the sample properties is presented. By means of bulk sensitive HAXPES measurements, a charge transfer towards the interface is observed, but on the LVO side. Additionally, a band bending effect could be found in the interface-near STO layers. Further approaches are made to determine the exact vanadium valence state and the amount of charge transferred to the interface.

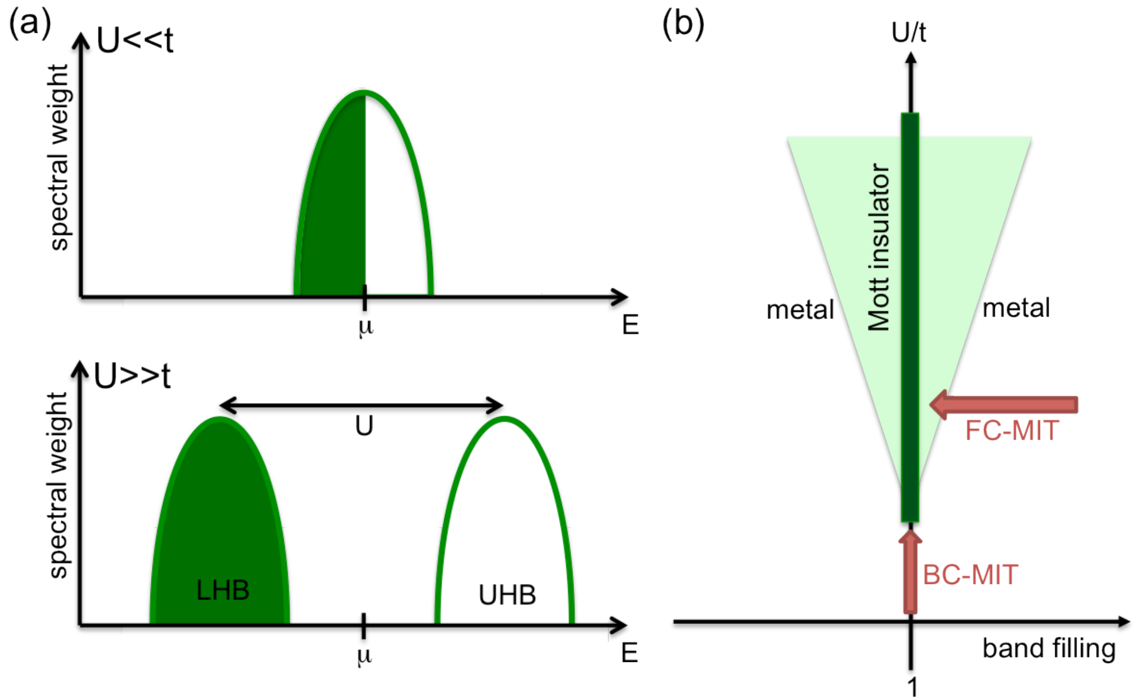

Figure 5.2: *(a) Schematics of the band structure for the cases $U << t$ and $U >> t$ within the Hubbard model, where U is the Coulomb repulsion and t the hopping parameter proportional to the bandwidth. For the case $U >> t$, the band splits into the lower and the upper Hubbard band (LHB/UHB). (b) Schematic phase diagram of the Hubbard model showing the filling-controlled (FC) and the bandwidth-controlled (BC) MIT.*

5.2 Doping of a Mott insulator

The insulating ground state of a Mott material is in general caused by correlation effects of the electrons in the outer *d*- and *f*-shells [208]. These correlation effects induce a charge gap at half filling of the bands, whereas band theory predicts a metal. A powerful model that describes the occurrence of a charge gap due to electron correlations is the well-known Hubbard model [209]. Besides the Mott insulating phase itself, metallic phases exit near the Mott insulator. Describing and understanding the electronic structure of the metallic and the insulating phases is interesting *per se*, but it may also help conceiving the physics of high-T_c superconductors like $La_{2-x}Sr_xCuO_4$ or the colossal magnetoresistance in $La_{1-x}Sr_xMnO_3$ [210, 211]. Both materials can be considered to be doped Mott insulators.

In Fig. 5.2 (a) the formation of the bands is illustrated, both neglecting electron-electron interaction (upper panel) and taking these interactions into account (lower panel). For weakly or non-interacting electrons a single band is formed by the overlap of the electron orbitals. In this simple model, it is assumed that only one electron orbital per lattice site exists. Thus, the band is exactly half-filled when each lattice site is

occupied by one electron. The hopping of an electron with opposite spin on an already occupied lattice site results in a strong Coulomb repulsion. In the Mott picture, this would lead to a splitting of this band into a lower fully occupied band and an upper one formed by electrons sitting on a doubly occupied lattice site. Thus, an insulating behavior will be the result when every lattice site is occupied by one electron like shown in the lower panel of Fig. 5.2 (a). These bands are named after J. Hubbard, who presented a theoretical model to explain this behavior [209]. Accordingly, the Hubbard-Hamiltonian is given by

$$H_{\text{Hubbard}} = -t \sum_{\langle ij \rangle \sigma} (c^{\dagger}_{i\sigma} c_{j\sigma} + c^{\dagger}_{j\sigma} c_{i\sigma}) + U \sum_{i} n_{i\uparrow} n_{i\downarrow}. \tag{5.1}$$

Here, i and j label lattice sites, $\langle ij \rangle$ stands for the summation over nearest neighbours, and $\sigma = \uparrow, \downarrow$ accounts for the spin degree of freedom. $n_{i\sigma}$ is defined by $c^{\dagger}_{i\sigma} c_{i\sigma}$, where $c^{\dagger}_{i\sigma}(c_{i\sigma})$ denote the creation (annihilation) of an electron at site i with spin σ. Hence, the second sum of Eq. 5.1 counts only doubly occupied sites. The most important parameters are the hopping integral t, which gives the probability amplitude for one electron to move from site i to j, and U, which is the Coulomb repulsion for two electrons occupying the same site. The hopping amplitude t scales directly with the bandwidth W of the respective band. Note that in the non-interacting case (U=0) the Hamiltonian describes a tight-binding band. Depending on whether $U << t$ or $U >> t$, the system will be metallic or insulating, as shown in Fig. 5.2 (a). This opens two ways to drive an MIT. On the one hand, the correlation strength U/t at half-band filling (n=1) can be varied, which is called bandwidth-controlled (BC)-MIT. On the other hand, for filling-controlled (FC)-MITs, the band filling is changed away from n=1. A schematic phase diagram of these MITs is shown in Fig. 5.2 (b) [211]. Taking only a single band into account, a band insulator corresponds to either n=0 or n=2 filling of the band. For a half-filled band (n=1), the Mott insulating phase is observed for $U >> t$, depicted in dark green in Fig. 5.2 (b). A noninteger filling of the bands usually leads to metallic behavior. However, a fluctuation-dominated phase is found (light green), which in principle should be metallic, but in fact is strongly influenced by the insulating phase. Additionally, the BC-MIT and the FC-MIT are indicated by the red arrows. For the first one, the lattice stucture of the material is varied in practice by applying, e. g., external pressure or chemical pressure. For the second one, the system is doped with additional electrons or holes, going away from half-filling of the bands.

In the Hubbard model presented above, only electrons in a single orbital are considered. However, transition metal oxides are multi-orbital d-electron systems. Here, orbital degeneracy and the overlap of the d bands and the p bands of ligand atoms are important and can be described in an extended Hubbard model [212]. A renormalization of the band near the Fermi-level can also be used to derive effective values from the simplified Hubbard model.

The perovskite vanadates offer the opportunity to study both kinds of MITs. An

example of a BC-MIT is $Ca_{1-x}Sr_xVO_3$. $SrVO_3$ exhibits an ideal cubic perovskite structure, whereas $CaVO_3$ crystallizes in an orthorhombic $GdFeO_3$-type structure due to the smaller radius of the A-cation. Chemical pressure is introduced into the system by substituting Sr^{2+} by Ca^{2+}, which results in a lower V-O-V bonding angle. This causes a reduced bandwidth and thus an enhanced correlation strength U/t. An FC-MIT can be found in the solid solution $La_{1-x}Sr_xVO_3$. The successive replacement of trivalent La by divalent Sr leads to an effective hole doping, going from a $3d^2$ towards a $3d^1$ configuration. Conducting behavior was observed above a critical doping concentration of $x > 0.2$ [213]. However, the substitution of the A-cation leads to a smaller V-O-V bonding angle for this material, too, resulting in a decrease of U/t [214]. For the observation of a 'clean' FC-MIT, it would be necessary to incorporate the electrons without any change of the underlying crystal structure, i. e., no substitution of atoms. LVO/STO heterostructures might serve for this purpose, if the model of doping by pure electrostatics described in Sec. 5.1 was valid.

Theoretical predictions of the photoemission spectra for pure LVO were given by Mossanek *et al.* [215]. Within their cluster model calculations, the transition-metal ground state is calculated taking also charge transfers of the forms $3d^n$, $3d^{n+1}\underline{L}$, and $3d^{n+2}\underline{L}^2$, etc., into account, where $\underline{L}$ denotes a hole in the O $2p$ ligand bands. A Coulomb repulsion of U=4.2 eV was assumed. In agreement with photoemission spectra they could identify one incoherently screened peak at about 1.8 eV. The ground state was found to be covalent, composed by the $3d^n$ and $3d^{n+1}\underline{L}$ states, resulting in an effective electron count of 2.4 for the vanadium [216]. This would imply that the insulating ground state in the simplified phase diagram (see Fig. 5.2 (b)) is slightly above half filling within the light green area.

5.3 Growth and characterization

The empirically found phase diagram shown in Fig. 5.3 for the growth of thick LVO films on STO substrates by PLD was proposed by Wadati *et al.* [217]. Depending on the oxygen partial pressure and the substrate temperature, either LVO or the higher oxidized $LaVO_4$ (LVO4) is formed. However, the phase transition is not sharp and a mixed phase develops in a mid-pressure regime. The physical properties of these two phases vary tremendously. LVO4 is monoclinic with a monazite-type structure ($P2_1/c$, a=0.705 nm, b=0.729 nm, c=0.673 nm, β=104.85°) and exhibits an insulating $3d^0$ electronic configuration [218]. The Mott insulating ($3d^2$) LVO has a $GdFeO_3$-type orthorhombic structure with the lattice parameters a=0.556 nm, b=0.785 nm, and c=0.556 nm, and can be described as a pseudocubic perovskite structure with a lattice parameter of a=0.392 nm [219]. As crystalline quality and phase purity are essential for discussing and interpreting the presented results, a thorough sample characterization is required.

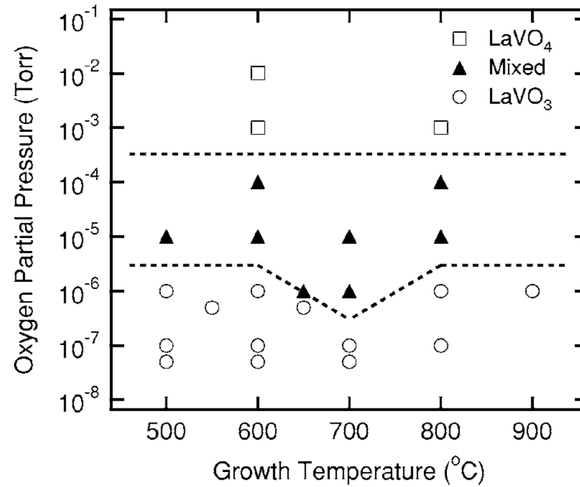

Figure 5.3: *Phase diagram for the growth of thick $LaVO_x$ films proposed by Wadati et al. [217]. Depending on the growth pressure and the growth temperature, different $LaVO_x$ phases can be stabilized.*

PLD settings

All films were grown in the MESA+ laboratory at the University of Twente using PLD. As a substrate, TiO_2-STO was used; it was prepared using the standard preparation techniques (cf. Sect. 4.3) [185]. When LVO is deposited directly on TiO_2-STO, so-called n-type interfaces are formed with the first layer being $(LaO)^+$. For the p-type interfaces a termination switch from TiO_2-STO to SrO-STO was achieved by growing 1 uc of $SrVO_3$ (SVO). Both materials, LVO and SVO, were ablated from polycrystalline targets. The PLD settings were identical for all films. A laser fluency of 2.2 J/cm^2 and a repetition rate of 1 Hz was used. The thickness was controlled by *in situ* RHEED. As already pointed out, the most crucial parameters during growth are the substrate temperature and the oxygen partial pressure. Best film quality was achieved when a pressure of $1.1 \cdot 10^{-5}$ mbar and a temperature of 670 °C were used. Samples were cooled down at growth pressure without an additional annealing or oxidation step. Note that the growth settings had to be adjusted and optimized with respect to the phase diagram shown in Fig. 5.3 for the specific PLD system.

RHEED and AFM

The RHEED oscillations recorded during the growth of a 10 uc LVO/STO film are shown in Fig. 5.4 (a). Note that for a better illustration the dotted line indicates a zoom into the data starting at the 3rd oscillation. The drop in the intensity during the first oscillation is caused by the heteroepitaxy. After this drop, the intensity is nearly recovered for the growth of every monolayer. The growth rate was determined to be 20 pulses/uc. The RHEED pattern of the film is shown in Fig. 5.4 (b). Although the film pattern is

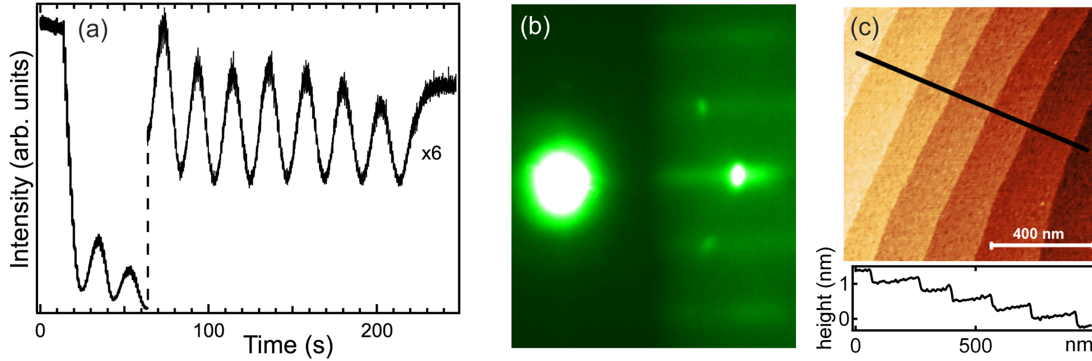

Figure 5.4: *Characterization of a 10 uc LVO/STO film. (a) RHEED oscillations during growth indicating layer-by-layer growth. (b) The RHEED pattern taken directly after growth is typical of a 2D film surface. (c) AFM image and height profile showing single unit cell steps, which confirm the 2D film surface.*

a bit streaky, all three Bragg spots (0,0), (0,$\bar{1}$) and (0,1) are sharp and distinct, which points to a 2D film surface. The oscillations together with the RHEED pattern taken directly after growth indicate a perfect layer-by-layer growth. Figure 5.4 (c) shows the AFM image of the 10 uc LVO/STO film together with a height profile that was recorded along the line shown in the image. The film surface is atomically flat with a step width corresponding to the miscut of the substrate and a step height of a single unit cell (c=0.39±0.01 nm).

Hotta *et al.* compared the structural properties of thick $LaVO_x$ films grown at different oxygen partial pressures [220]. For the LVO phase they observed regular RHEED oscillations pointing to layer-by-layer growth. They were able to confirm the 2D growth by AFM, as the images exhibit regular steps with a step height corresponding to 1 uc. For the LVO4 phase, they found an island-like growth mode evidenced by AFM and a loss of RHEED oscillations.

X-ray reflectivity and x-ray diffraction

XRR and XRD measurements were performed to analyze the structural properties and the film composition. The x-ray reflectivity is plotted in Fig. 5.5 (a). Both materials, LVO and LVO4, differ strongly in their densities (ρ_{LVO}=6.8 g/cm^2, ρ_{LVO4}=5.0 g/cm^2), which is reflected in the XRR spectra (cf. Sect. 2.4). A comparison of simulations for both materials assuming that surface and interface roughness are identical, with the data of a 10 uc sample confirms the LVO phase. The simulated LVO spectrum exhibits clear oscillations, which are also present in the measured data, but absent in the LVO4 simulation. Note that the data can be fitted more accurately, when an extra carbon layer is assumed to be on the surface. This is a natural assumption as all measurements were done *ex situ*.

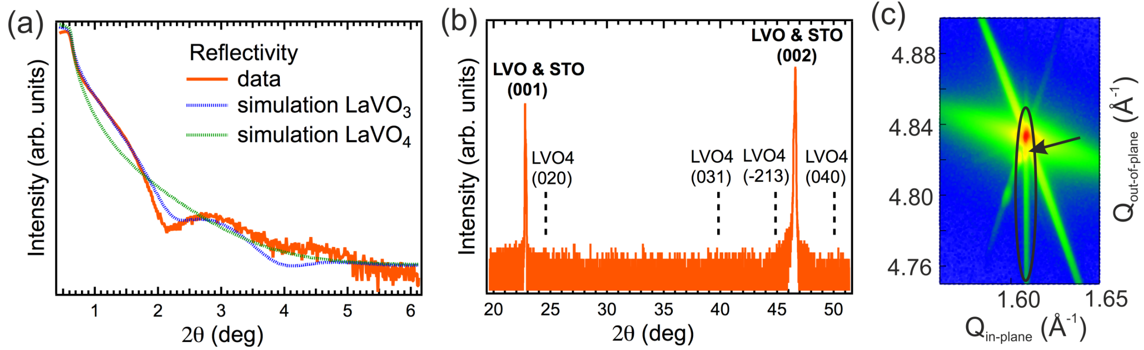

Figure 5.5: *Structural characterization. (a) X-ray reflectivity: A comparison to simulations of LVO and LVO4 confirms the LVO phase for the films under investigation. (b) Wide range θ-2θ scan exhibiting only (00n) Bragg peaks corresponding to LVO and STO. The dotted lines indicate the expected positions of LVO4 Bragg peaks. (c) Reciprocal space map of the (103) Bragg peak. The arrow points to the maximum of the film peak, which indicates a coherently strained LVO overlayer.*

Figure 5.5 (b) shows a wide range θ-2θ scan. Two peaks are strongly visible, which can be identified as the (001) and (002) Bragg reflections of LVO and STO. Due to the vanishing lattice mismatch, their position is identical. The dotted lines indicate the expected positions of peaks related to LVO4 (cf. Hotta *et al.* [220]). However, none of them could be observed in the spectrum. This stands for a good epitaxial quality and crystalline film growth. For a more detailed diffraction analysis of the film, a reciprocal space map of the (103) Bragg reflection is displayed in Fig. 5.5 (c). The advantage of this analysis is that one can discriminate the instrumental broadening from film features. The drives of the XRD machine, e. g., cause a broadening in θ-2θ direction, which appears from the upper left to the lower right corner in this map. The substrate peak can be identified by the highest intensity (red), while the film peak appears as the vertically elongated line with its maximum shown by the arrow. The elongation is due to the finite film thickness. Both peaks exhibit the same $Q_{\text{in-plane}}$ value of 1.61 $Å^{-1}$, which corresponds exactly to the STO lattice constant. In the out-of-plane direction, the film peak exhibits a slightly smaller Q value with respect to the substrate peak, indicating an elongation of the c-axis lattice constant.

Scanning transmission electron microscopy

HAADF-STEM images (cf. Sect. 4.5) were taken by M. Kamp from the Wilhelm Conrad Röntgen Research Center for Complex Material Systems at the University of Würzburg. The image in Fig. 5.6 of a 10 uc LVO/STO film confirms the all-perovskite structure of both substrate and film. The viewing direction is along the [001] direction of the STO. Labelled are the atomic positions of the film atoms La and V as well as the substrate atoms Sr and Ti. Disregarding the surface quality, which is strongly influenced by the deposited carbon during lamella preparation, the film is coherently strained to the

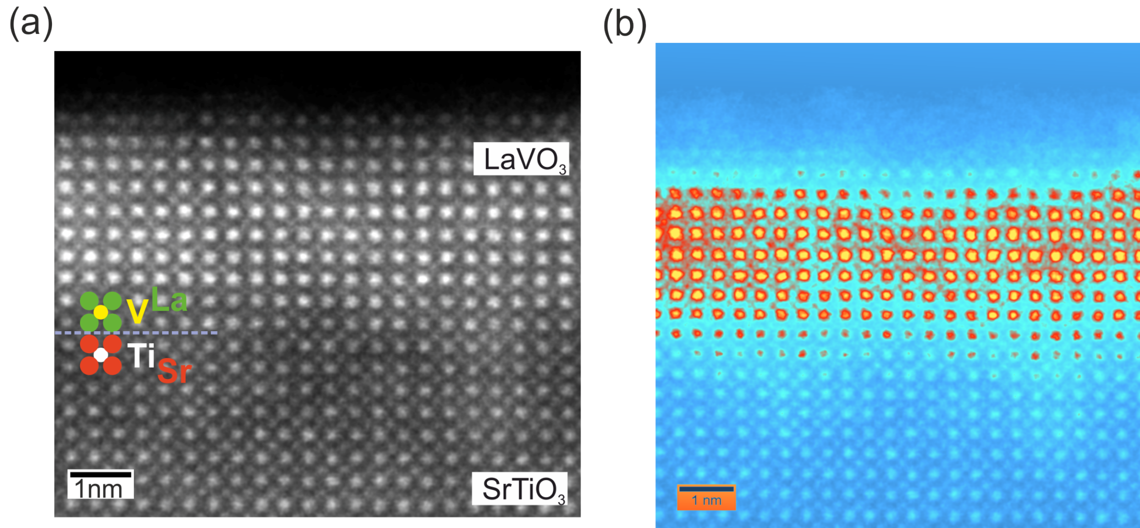

Figure 5.6: *(a) HAADF-STEM image of a 10 uc LVO/STO thin film. (b) STEM image in a false color plot. The film exhibits a perovskite lattice structure without any obvious defects or dislocations. The interface roughness can be estimated to be about 1-2 uc.*

substrate with no obvious defects, dislocations or impurity phases, forming a sharp interface. In Fig. 5.6 (b), the image is further processed, i. e., mainly the colors are inverted. This makes it more easy to distinguish the film from the substrate and to show the sharpness of the interface. However, a comparison to the STEM images of LAO/STO from Sec. 4.5 indicates that the interface of LVO/STO is more blurry and the interface sharpness in the case of LVO/STO is estimated to be about 1-2 uc.

Fitting Kourkoutis *et al.* analyzed the growth of LVO4 and LVO on STO substrates by means of STEM. They found 3D islands and clusters in the case of LVO4, while LVO is coherently strained to the substrate [218]. Furthermore, this group also analyzed LVO/STO superlattices. They found p-type interfaces (going from LVO to STO with respect to the growth direction) always to be more sharp in comparison to n-type interfaces [221]. As a possible explanation they name Sr segregation being stronger for n-type interfaces. This could also be the case for the LVO/STO films investigated in this thesis.

In summary, the structural analysis by means of various methods revealed the films analyzed in the scope of this thesis to be clearly LVO. Films grow layer-by-layer, as indicated by RHEED, and no impurity phases could be observed by XRD. However, the interface sharpness seems to be reduced as indicated by STEM, possibly due to Sr segregation.

5.4 Thickness-dependent transport properties

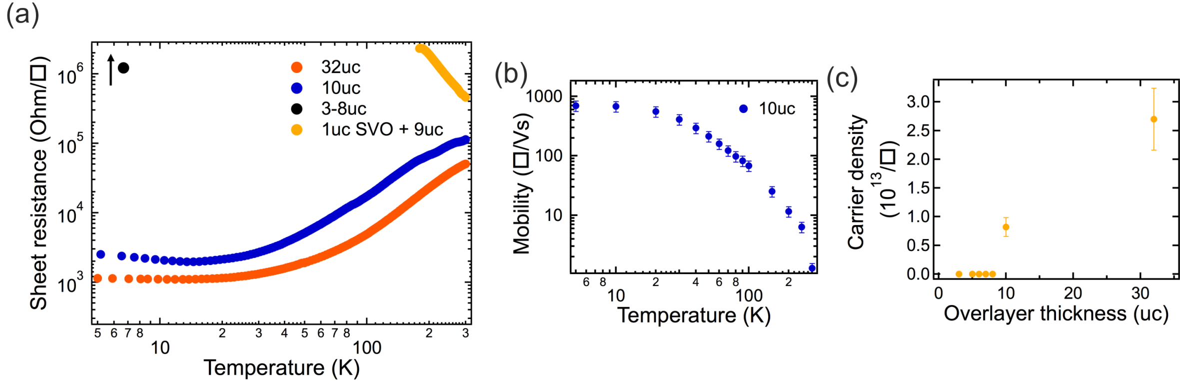

Figure 5.7: *Transport properties: (a) Sheet resistance of samples exhibiting different overlayer thicknesses and interface terminations. Conducting behavior is found for a film thickness above 8 uc. (b) Electron mobility of a 10 uc sample. (c) Carrier density for different overlayer thicknesses.*

Transport measurements were carried out in van-der-Pauw geometry. For the determination of the sheet carrier density, the magnetic field was swept between ± 3 T. Contacting the interface was accomplished by planting small gold contacts on the very edges of the samples. The temperature-dependent conductivity for samples with different overlayer thicknesses is shown in Fig. 5.7 (a). Conducting behavior is observed above an overlayer thickness of 8 uc. A resistance $> 20\,\mathrm{M\Omega}$ is found for the insulating films. For the conducting samples, the sheet resistance is in the same range as given by Hotta *et al.* for LVO/STO and standard high-quality LAO/STO films, which are taken as a reference for a 2DES [17, 19, 155, 222]. However, Hotta *et al.* found a critical thickness for conductivity of only 5 uc. The interface of the 1 uc SVO + 9 uc sample is insulating, which agrees with the literature [19]. This is even more surprising as growth of this interface was accomplished by depositing 1 uc of SVO, which exhibits metallic behavior as bulk material. The temperature dependence of the carrier mobility is plotted in Fig. 5.7 (b). It increases at low temperatures to values up to $600\,\mathrm{cm^2/Vs}$ and is thus as high as found in LAO/STO thin films [17, 191]. The carrier density is about $10^{13}\,\mathrm{cm^{-2}}$ for the conducting samples. While it shows only little dependence on the temperature, it increases with the overlayer thickness.

The results of the conductivity measurements relate the LVO/STO system closely to the LAO/STO system, suggesting a similar mechanism at play. The sheet carrier density derived by Hall measurements for LVO/STO is lower than proposed by the model of the electronic reconstruction. Similar observations have been made for LAO/STO, where it was suggested that mobile and immobile carriers could be present, the latter not measurable in transport [160, 178]. For the 32 uc LVO/STO sample a higher carrier density was found compared to the 10 uc sample. In the simple model of the electronic reconstruction, the number of charge carriers transferred to the interface scales with the

overlayer film thickness. Although more data points are needed that support the trend of an increased carrier density for thicker LVO overlayers, it can give further indication for an electronic reconstruction in LVO/STO.

5.5 Charge transfer within the film

HAXPES was employed to explore the electronic structure of the LVO/STO heterostructures, as a detailed analysis of the core-levels provides valuable information on the charge distribution (cf. Sect. 4.6). Experiments were carried out at the synchrotron beamlines KMC-1 at BESSY (Berlin) [130] and BW2 at HASYLAB (Hamburg) [195]. Photon energies of 3 keV, 3.5 keV, 4 keV, and 5 keV were used. Additionally, the detection angle was varied between θ=5° and 50°.

5.5.1 Analysis of core-level and valence band spectra

V $2p$ **core-level**

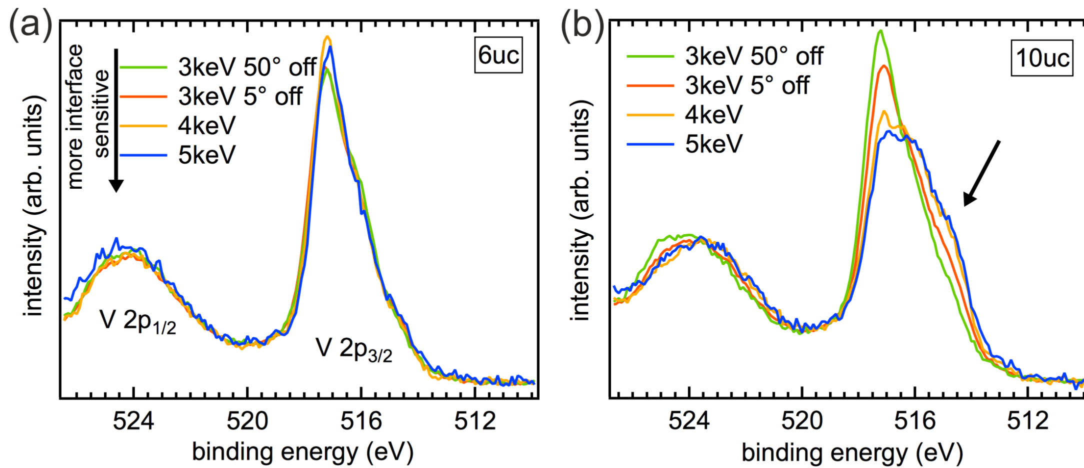

Figure 5.8: *HAXPES depth profiling of the V 2p core-level. Spectra for (a) a 6 uc and (b) a 10 uc LVO/STO film. No dependence on the probing depth is found for the 6 uc sample. In contrast, for the 10 uc sample a shoulder (indicated by the arrow) is present at the lower binding energy side for interface sensitive measurements. This indicates the presence of extra electrons near the interface.*

The V $2p$ core-level spectra are displayed for a 6 uc and a 10 uc LVO/STO film in Fig. 5.8 (a) and (b). Both spectra show the V $2p_{1/2}$ peak at a binding energy of about 524 eV and the V $2p_{3/2}$ at about 517 eV. Spectra are normalized to equal integrated intensity. For the 6 uc film, all spectra are virtually identical exhibiting no dependence on the probing depth. This stands for uniform film growth and similar electronic properties throughout the entire film. However, the shape of this core-level cannot be assumed to be a standard Voigt profile. The asymmetry can be attributed to the complex multiplet

and crystal field effects of the $2p^5 3d^2$ HAXPES final state. So fitting of such a peak is difficult and the discussion will first be kept on a qualitative level. Energy position and lineshape agree with earlier photoemisson studies of LVO thin films [217]. Without any indication of the presence of LVO4, we take this spectrum as representative of nominally trivalent V ions in the LVO film. In contrast, the spectra of the 10 uc sample in Fig. 5.8 (b) show a pronounced change with the probing depth. While for the most surface sensitive photoemission conditions the spectrum is almost identical to that of the 6 uc sample, a pronounced shift of spectral weight towards lower binding energy occurs for increasing interface sensitivity (see arrow in Fig. 5.8 (b)). This indicates a reduction of the V valence from its nominal 3+ value from the surface towards the interface, i. e., at or near the interface the V valence states become populated by excess electrons leading to a $3d^{2+x}$ configuration. This behavior can be seen on both the V $2p_{1/2}$ and the V $2p_{3/2}$ core-levels.

Ti $2p_{3/2}$ core-level

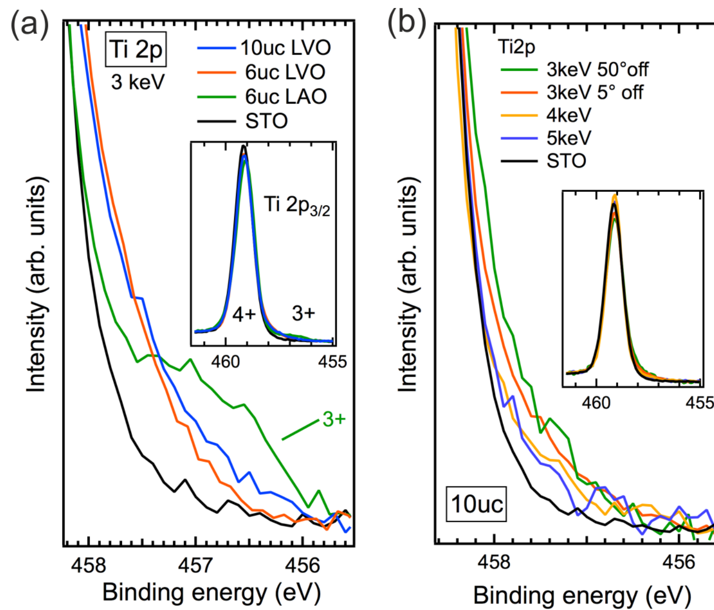

Figure 5.9: *(a) Comparison between the lower binding energy parts of the Ti $2p_{3/2}$ core-level HAXPES spectra of STO, LAO/STO and LVO/STO. The inset shows the entire Ti $2p_{3/2}$ core-level spectra. In LVO/STO, no LAO/STO-like Ti^{3+} peak is observed, but the peak exhibits an asymmetry independent of the overlayer thickness. (b) HAXPES depth profiling for the 10 uc LVO/STO sample. The asymmetry of the Ti $2p_{3/2}$ core-level is most pronounced for interface sensitive measurements.*

Spectra of the Ti $2p_{3/2}$ core-level taken on a 6 uc and a 10 uc LVO/STO film are displayed in Fig. 5.9 (a). The main Ti $2p_{3/2}$ peak is located at a binding energy of 459.1 eV. For comparison, the Ti spectra of bulk STO and a 6 uc LAO/STO reference film are shown. While the inset shows the complete Ti $2p_{3/2}$ core-level spectra, the main figure

displays a zoom to the lower binding energy parts. Clear differences can be seen in the spectra. The LAO/STO sample displays an additional peak, which can be related to Ti^{3+} states originating from the 2DES. In contrast, the LVO/STO spectra exhibits a certain asymmetry, which becomes evident when compared to bare STO. This feature is more smeared out in LVO/STO and cannot be described as a second peak with a distinct chemical shift as is the case for LAO/STO ($\Delta E(\mathrm{Ti}^{3+})$=2.2 eV). Furthermore, as this asymmetry is present for both the 6 uc and the 10 uc samples it cannot be directly related to the mechanism that generates conductivity. In Fig. 5.9 (b) the depth dependence of the Ti $2p_{3/2}$ core-level for 10 uc LVO/STO samples is shown. Once again compared to STO, the asymmetry is enhanced in more surface sensitive measurements. This gradual change could give a hint to a band bending effect at the interface [56, 57]. The higher asymmetry in the interface sensitive spectra implies an upward band bending of the STO bands near the interface. The same behavior is also found for the 6 uc LVO/STO spectra. The effect will be further analyzed and discussed in Sec. 5.5.3.

Valence band

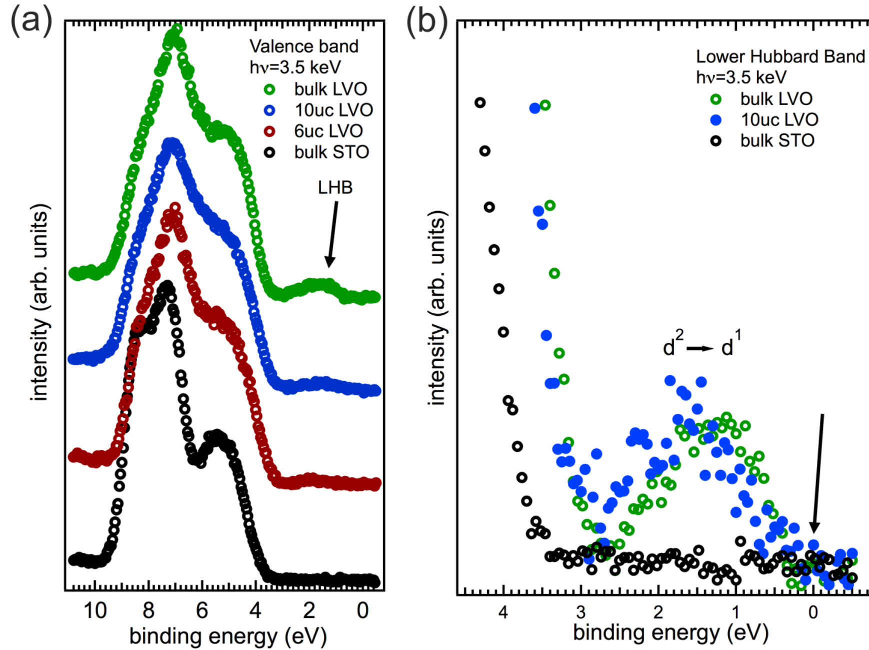

Figure 5.10: *(a) HAXPES valence band spectra of bulk STO, bulk LVO, 6 uc LVO, and 10 uc LVO. In all LVO spectra, the LHB is present at a binding energy of about 2 eV. (b) Lower Hubbard band of a 10 uc LVO sample in comparison to bulk LVO and bulk STO. No indication of a quasi-particle peak or upper Hubbard band are observed at the Fermi-level.*

Valence band spectra for both film thicknesses and bulk materials are displayed in Fig. 5.10 (a). The main part of the spectra originating from the O $2p$ related states lies

between 9 and 3 eV for all samples. For the bulk LVO and also for the LVO films an additional peak is visible between 2 and 0 eV. This can be identified as the lower Hubbard band corresponding to the V d^2 to V d^1 transition; it is in line with previous valence band analyses and is a clear fingerprint for LVO [215, 217]. The spectral weight of the peak scales with the probed LVO volume and is smallest and hardly visible for the 6 uc sample. In Fig. 5.10 (b) a zoom to the Fermi energy region is shown. In principle, the doping of extra electrons, which is evident from the V $2p$ core-level analysis, into the V $3d$ states should lead to the population of the upper Hubbard band. However, such a peak could not be discerned. Note that the same problem occurs in HAXPES for conducting LAO/STO. In this case the Ti $3d$ states could not be observed directly. The signal originating from the extra electrons in the V $3d$ states is damped by an overlayer of 10 uc and amounts to only a few percent of the signal of the undoped LVO/STO. Moreover, HAXPES cross-sections are exceedingly small, especially for the valence and conduction band region [52, 53]. For doping a Mott insulator, a jump of the chemical potential is observed as the Fermi-level is pinned at the upper Hubbard band or at a respective quasi-particle peak [211]. From a comparison of the valence bands such a shift is not observed. On the one hand, charging effects of the insulating samples cannot be entirely excluded. On the other hand, the calculations of Mossanek *et al.* indicate that the insulating ground state of LVO does not exactly correspond to half-filled bands and thus the Fermi-level could already be pinned for the insulating samples [215].

Discussion

From the qualitative analyses of the film and the substrate core-levels, important information on the electronic structure of these samples can be extracted:

- No changes in the Ti $2p$ core-level could be found between conducting and non-conducting samples.
- The spectral weight transferred in the V $2p$ spectra to lower binding energies, which is present only for the conducting samples, points to an electron-rich layer near the interface. In the electronic reconstruction picture this implies a transfer of electrons within the film.
- The asymmetry in the Ti $2p$ core-levels is most likely caused by an upward band bending near the interface on the STO side of the interface.

Based on these findings, a depiction of the electronic reconstruction as could be the case for LVO/STO is shown in Fig. 5.11. To circumvent the polar catastrophe, electrons are transferred to the $(VO_2)^-$ planes near the interface. This compensates for the potential build-up without involving the STO. Note that the potential in the vacuum is not zero in this case, but constant. Furthermore, the average potential within the LVO is not zero either, in contrast to the average potential within the LAO for LAO/STO.

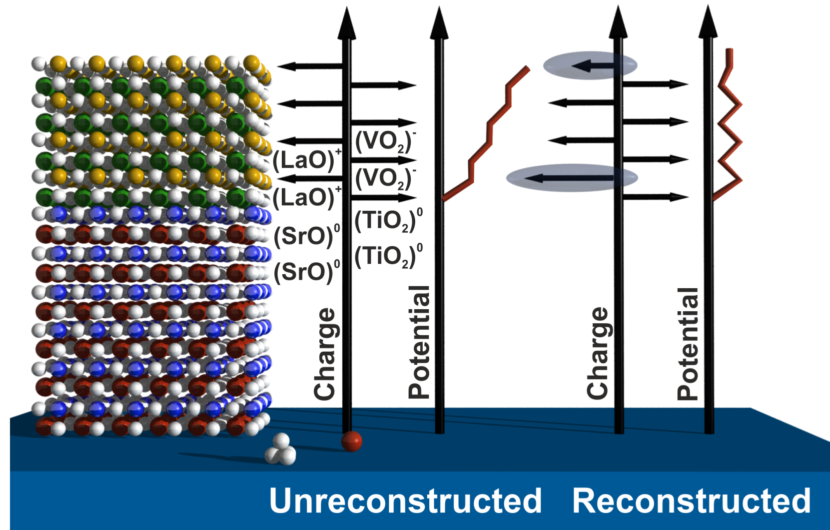

Figure 5.11: *Model of an electronic reconstruction scenario in LVO/STO. A charge transfer of half an electron from the surface towards the interface within the film material compensates the potential build-up and results in a constant potential outside the heterostructure.*

Thus, this theoretical model does not describe the energetically most favorable state. Additionally, the charge cannot be transferred to the very last interface layer as this is $(LaO)^+$.

The critical overlayer thickness is increased in the case of LVO compared to LAO. If the polar discontinuity can be assumed to be the driving force for the formation of a conducting layer, the higher overlayer thickness could be explained by a difference in the bonding character going from LAO to LVO. It could be the case that the single layers of $(LaO)^+$ and $(VO_2)^-$ exhibit a stronger out-of-plane covalent character and hence are less ionic. Thus, the potential build-up would be slower for LVO/STO. A higher dielectric constant of LVO compared to LAO would also result in an enhanced critical thickness. However, exact values could not be obtained from the literature. A further explanation may be provided by a preferential Sr segregation in LVO/STO as the Sr atoms would provide additional interface charges [221]. There is also a discrepancy to the literature concerning the critical overlayer thickness for LVO/STO, which cannot be fully explained up to now [19]. It can only be speculated that there are slight differences in substrate preparation or cool-down procedures that make films conducting also for thinner overlayers.

The mechanism described here – an electronic reconstruction in the film itself – would imply a doped region in the LVO film. Extra electrons in this film region can only be hosted in the UHB of the LVO. In the simplest picture this could be achieved by transferring electrons from the LHB at the surface to the UHB at the interface, which

requires a potential gradient within the LVO film and the LHB being hole-doped at the surface, i. e., located at the Fermi-level. However, the LHB in the valence band spectra in Fig. 5.10 is at the same high binding energy for all samples. Similar observations have been made for LAO/STO, where it was suggested that alternatively excess electrons can be introduced by oxygen vacancies at the surface, providing a natural explanation for the absence of a band gradient [166]. A similar picture could be proposed for LVO/STO.

Based on these results, the occurrence of a conducting 2DES in LVO/STO induces a band-filling-controlled Mott MIT in LVO. In bulk oxides such transitions are normally achieved by chemical doping (e. g., cation substitution). From a purely electronic point of view, metallization of a Mott insulator should occur already at the smallest band fillings. However, antiferromagnetism often stabilizes the insulating phase up to finite doping levels [211]. Moreover, the transition is often further delayed or even completely suppressed by dopant-induced impurity potentials and disorder. In contrast, the metallization of LVO/STO heterostructures is based on a purely electrostatic mechanism and thus offers the unique possibility to study the filling-controlled Mott transition in the absence of dopant effects.

5.5.2 A more detailed view on the vanadium spectra

Reduction and oxidation of LVO/STO thin films

As mentioned before, the V 2*p* core-level of LVO/STO exhibits a complicated line shape due to multiplet and crystal field splitting. Moreover, the spectral line shape changes tremendously when the vanadium valence state is altered, because the multiplet splitting strongly depends on the number of electrons in the *d*-shell. One way of changing the vanadium valence state is to change the oxygen stoichiometry of the film. Oxygen vacancies donate two electrons per atom and thus cause an effective electron doping of the system. In principle this should also drive a MIT, however, not as an interface effect but in the volume of the film. Nevertheless, spectral changes in the line shape should be comparable. Hence, a 6 uc LVO/STO film was reduced in vacuum and subsequently oxidized to analyze the influence on the core-level and valence band spectra. The exact treatment procedure is given in Tab. 5.1.

Table 5.1: *Steps of the reduction and oxidation series of the 6 uc LVO/STO film of Fig. 5.12.*

reduction		oxidation	
step 1	2h, 330°C	step 5	0.5h, 10^{-5} mbar, 365°C
step 2	2h, 355°C	step 6	0.5h, 10^{-5} mbar, 365°C
step 3	2h, 365°C	step 7	1h, 10^{-3} mbar, 365°C
step 4	2h, 425°C	step 8	1h, ambient air

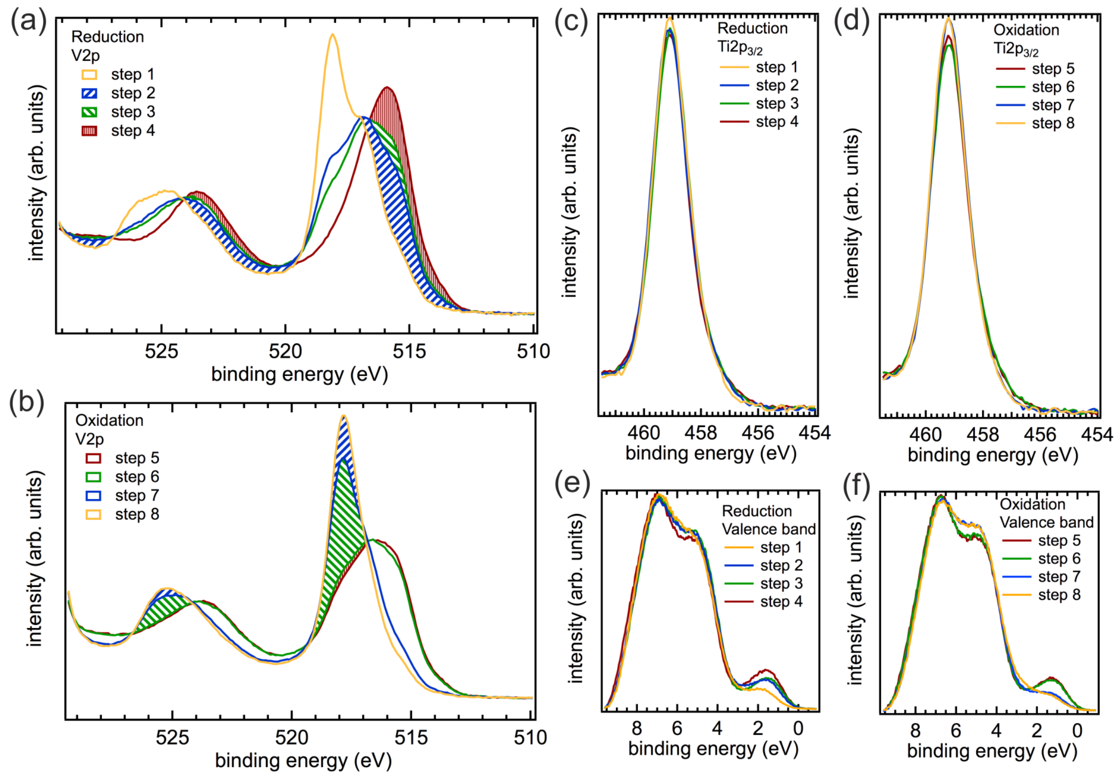

Figure 5.12: *XPS core-level spectra of an in situ reduced 6 uc LVO/STO thin film: (a) V 2p spectra show a transfer of spectral weight to lower binding energies. (c) Ti $2p_{3/2}$ core-level spectra display only marginal differences. (e) Valence band region: The peak near the Fermi-level gains spectral weight. Subsequent oxidation of the film in a moderate O_2 atmosphere: (b) V 2p, (d) Ti $2p_{3/2}$ and (f) valence band spectra show the reversibility of the process.*

Films were first reduced under high-vacuum conditions at elevated temperatures up to 425°C for several hours. Oxidation was achieved by heating the film in oxygen. For cool down the oxygen pressure remained unchanged. In the last step, the samples were taken out of the process chamber to study the influence of the ambient pressure.

The evolution of the V $2p$ spectra upon reduction is shown in Fig. 5.12 (a). The longer the sample is heated in vacuum, the more the spectral weight is shifted to lower binding energies. This can be interpreted as a fingerprint of the extra electrons hosted in the V $3d$ states. A subsequent oxidation at moderate temperatures leads to a re-filling of the oxygen vacancies. The spectral weight is shifted back, as can be seen in Fig. 5.12 (b), and the initial line shape of the V $2p$ spectrum is essentially recovered. As this effect is reversible it can be concluded that the LVO phase, i. e., the perovskite lattice structure, is preserved during the treatment. The effect can be clearly attributed to a change in the oxygen stoichiometry, as a La or V deficiency or enhanced intermixing at the interface caused by the annealing process would not be reversible by oxidation. Comparing this

data to the 10 uc LVO/STO spectra, the shoulder shown in Fig. 5.8 (b) can be directly interpreted as a sign for electron doping near the interface in the film.

In Fig. 5.12 (c) and (d), Ti $2p_{3/2}$ core-level spectra are shown for the different reduction and oxidation steps. The asymmetry of the peak remains almost unaffected during reduction and oxidation. A much stronger effect during reduction and oxidation would be expected, if the asymmetry would be directly related to the Ti^{3+} states.

The valence bands are displayed in Fig. 5.12 (e) and (f). While the changes in the main peak between 9 and 3 eV are comparably small and can be attributed to the loss of oxygen, the incoherent part gains spectral weight and shifts to lower binding energies during reduction. This indicates a further population of the V $3d$ states and is in line with the behavior of the V $2p$ core-level. However, the limited resolution of XPS ($\Delta E \approx 0.7$ eV) does not allow to determine whether the LHB becomes further populated or the UHB is populated. Similar behavior was observed by Maiti *et al.* who analyzed the valence band of $La_{1-x}Ca_xO_3$ crystals by means of UPS and XPS [223]. While in UPS the development of a quasi-particle peak was found for increasing x, in XPS only one broad peak was observed.

Comparison to vanadium oxide single crystals

Besides the qualitative evolution of the spectra due to electron doping, the precise valence states of the LVO/STO thin films are of interest and would allow a quantification of the charge transfer. However, the multiplet splitting of the core-levels hinders a fit using standard line shapes. A comparison between the thin film spectra and spectra of compound materials which host in a well-defined valence state may yield additional information provided that the line shape is mainly determined by the mutliplet splitting, i. e., the electron d count, and not by the crystal field that depends on the crystal structure.

V_2O_5, VO_2, and VOCl HAXPES and XPS spectra were measured. For these HAXPES measurements, the same settings were used as for the LVO films. All spectra were calibrated with respect to an Au reference sample. The vanadium oxide crystals exhibit a vanadium valence reaching from 5+ (d^0) to 3+ (d^2). For V^{3+}, VOCl was used, as high-quality stoichiometric V_2O_3 was not available in this study. All single crystals were prepared by *in situ* filing. No contaminations like carbon could be observed afterwards. A drawback of this comparison is that no V^{2+} reference was available. This will be further discussed in the following.

Both V $2p$ core-level spectra and valence band spectra are displayed in Fig. 5.13 (a) and (b). The blue spectrum corresponds to V_2O_5, which is a d^0-system. The absence of the $3d$ peak around 1-2 eV in the valence band and the sharp and nearly symmetric V $2p$ spin-orbit split doublet give an indication for that. The green and red spectra correspond to VO_2 (d^1) and VOCl (d^2), respectively. The core-levels display a strong asymmetry, which can be attributed to the multiplet effects of the $2p^53d^1$ and the $2p^53d^2$ PES final states, respectively. The higher the d electron count, the more spectral weight

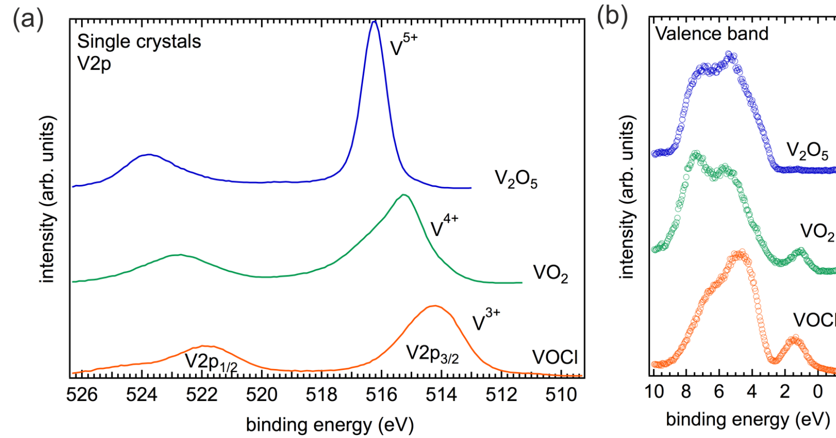

Figure 5.13: *HAXPES spectra of single crystal vanadium references: V_2O_5, VO_2 and VOCl. (a) The V 2p core-level spectra strongly depend on the vanadium valence state. (b) Valence band region showing the lower Hubbard band for VO_2 and VOCl.*

is transferred to lower binding energy, because the core-hole screening is enhanced. In the valence band region, an additional peak develops near the Fermi energy upon occupation of the vanadium *d* band. This peak can be identified as the lower Hubbard band. The spectral weight for VOCl is increased as the electron count of this orbital is twice as high as that of VO_2. For a more detailed discussion it should be referred to Zimmermann *et al.* and Glawion *et al.* [224, 225].

The V 2*p* spectra of VOCl with a nominal valence state of 3+ are compared to the 6 uc LVO film in Fig. 5.14 (a). Both the spectral line shape and the energetic position are different. Thus, either the V valence in the LVO film is not purely 3+ or VOCl is not suitable as a reference. If both spectra can be assumed to represent 3+, effects like crystal field splitting due to the different crystal structure and ligand configuration could be responsible for the deviations, and a further analysis can only be made using theoretical calculations. From a comparison of the perovskite $LaFeO_3$ to the Fe_2O_3 single crystal spectra, it is known, for instance, that the lineshape is more narrow in the case of $LaFeO_3$, while the energetic position is roughly the same [226]. Assuming that the reason for the spectral difference is due to the fact that the valance state in the LVO film is not exactly 3+, the broadened structure which is shifted to higher binding energies implies the presence of higher valence states. In order to extract qualitative information on this issue, a superposition of single crystal spectra is used to produce a numerical fit of the angle-dependent and the energy-dependent HAXPES data of the 6 uc and the 10 uc LVO thin films as well as the reduction/oxidation series. For all spectra, a linear background was subtracted, since a Shirley background led to non-physical behavior, probably due to the vicinity of the O 1*s* core-level. Furthermore, all spectra were normalized to equal integrated intensity. As all films were calibrated to a Au reference, the energetic position of the vanadium core-level was kept constant in the fit procedure, leaving the relative weights of the individual V valencies the only free fit parameter.

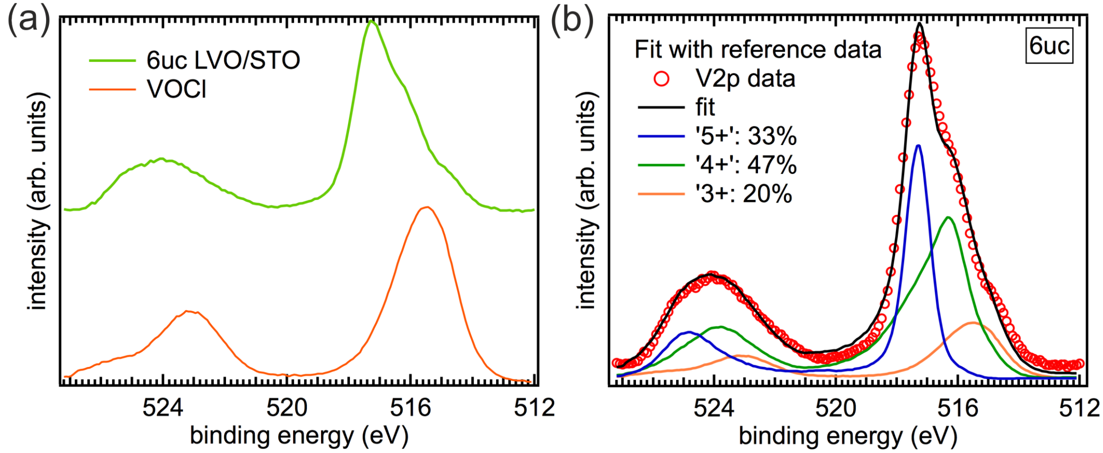

Figure 5.14: *(a) V 2p core-level spectra of VOCl and a 6 uc LVO/STO film. (b) Fit of the V 2p spectrum of a 6 uc sample using single crystal reference spectra.*

Figure 5.14 (b) shows the fit of the 6 uc film with the single crystal reference spectra. Note that since the fit is not made using Voigt profiles but measured data, the accuracy of a standard fit cannot be reached. Taking this into account, the film data is well-reproduced from the fit. Furthermore, inferred from the comparison shown in Fig. 5.14 (b), spectral weight seems to be shifted only to the higher binding energy side with respect to VOCl (V^{3+}), allowing an accurate fit without a 2+ reference, which should be shifted to lower binding energies. Also in the case of the 10 uc film, similar fits are obtained without a 2+ reference, but it should be pointed out that a 2+ component cannot be ruled out completely.

Table 5.2: *Average V valence state derived from a fit with single crystal reference spectra for depth profiling of a 6 uc and a 10 uc LVO film.*

depth profiling	average V valence	
	6 uc	10 uc
3 keV, 50°off	4.1	4.1
3 keV, 5°off	4.1	4.0
4 keV, 5°off	4.2	3.8
5 keV, 5°off	4.2	3.7

The fit allows to give an estimate of the average valence state of the vanadium in the LVO/STO films. Results are given in Tab. 5.2 for the depth profiling of the 6 uc and the 10 uc LVO film and in Tab. 5.3 for the reduction/oxidation series. Although the error margin is about 20 %, the average valence is in all cases higher than the nominal valence of 3+, which is obvious, as all reference spectra have a higher valence

Table 5.3: *Average vanadium valence during reduction and oxidation of a 6 uc LVO/STO film.*

reduction	average V valence	oxidation	average V valence
2 h, 330°C	4.0	0.5 h, 10^{-5} mbar, 365°C	3.5
2 h, 355°C	3.6	0.5 h, 10^{-5} mbar, 365°C	3.6
2 h, 365°C	3.5	1 h, 10^{-3} mbar, 365°C	4.2
2 h, 425°C	3.1	1 h, ambient air	4.4

state. For the insulating 6 uc sample an average valence of 4.1+, which is essentially the same for all probing depths, is derived. In contrast, it decreases for the most interface sensitive measurements of the conducting 10 uc samples down to a value of about 3.7+. These findings are in line with the qualitative discussion of the data. The reduction and oxidation series show the same trend. For the most reduced state of the series, the average valence is highest. Note that the minimum valence reached is about 3.1+. This analysis implies that the starting point, namely the 6 uc LVO/STO film, has a higher oxidation state, although the film is single-phase LVO as verified by the structural analysis. A comparison of the valence band spectra cannot be made, as the valence band of the thin films is a composition of STO *and* LVO.

Multiplet calculations

For the fits presented above it is assumed, that effects like crystal field splitting and ligand configuration play only a minor role for the comparison of single crystal data to film data and fits completely rely on the energy calibration using an Au reference spectra. Another approach to disentangle the vanadium spectra and determine the valence states involves theoretical simulations using ligand-field multiplet theory. These simulations can reproduce the spectral line shapes and relative peak positions of different V valences taking into account both the different electron d count and the crystal-field splitting. However, the simulations lack absolute binding energies and thus the positions have to be adapted to the experimental data. Simulations were done using the program ‘CTM4XAS’ [227]. A detailed description and review can be found in Refs. [228, 229]. The program uses Hartree Fock methods taking into account spin-orbit multiplets, crystal field splitting and charge transfer multiplets. This many-body cluster approach embeds the ion under consideration into a cluster of ligand atoms representing the crystalline symmetry. The method has been very successful to calculate excitation spectra for correlated materials, as initial and final states are calculated on equal footing. The following parameters were used to generate reference spectra for the valence states V^{5+} to V^{2+}: The spin-orbit coupling parameters were kept the same as for the free atom. Octahedral crystal symmetry (O_h) with a crystal field splitting of $10Dq$=2 eV and a charge transfer energy Δ of 2 eV was used. As the program only derives discrete energetic positions, the spectra had to be convolved using a Lorentzian

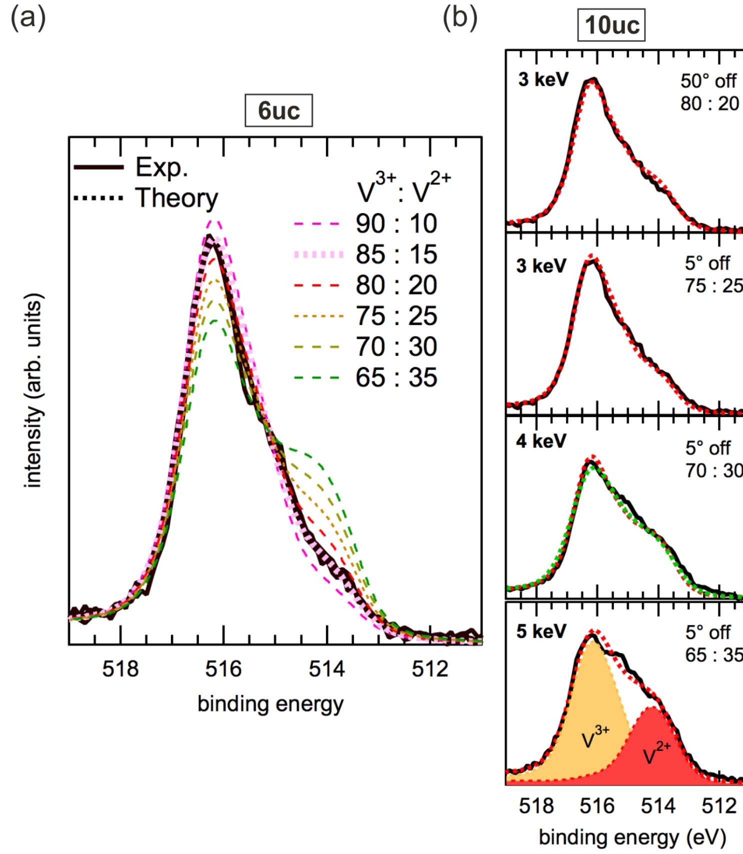

Figure 5.15: *Multiplet simulations for the LVO films. Spectra were simulated with a 3+ and 2+ component. (a) Experimental data of the 6 uc LVO/STO film together with simulated spectra for different 3+/2+ ratios. (b) Best fit simulations for the different measurement geometries for the 10 uc LVO film.*

width of 200 meV and a Gaussian width of 400 meV for comparison to the experiment. The best fit was produced for the V $2p_{3/2}$ spectrum with only the V^{3+} and V^{2+} reference spectra superposed. For other combinations of V^{5+}, V^{4+}, V^{3+}, and V^{2+} valence spectra, chemical shifts and satellite structures did not fit the experimental data. However, note that also in this case it was possible to reproduce the V $2p_{3/2}$ only, failing for the V $2p_{1/2}$ as the simulated spectra were too narrow in energy to account for the experimental structure. All simulated spectra had to be shifted by 2.6 eV to higher binding energies to fit the data.

Simulations of the V $2p_{3/2}$ core-level spectra are shown in Fig 5.15 (a) and (b) for the 6 uc and the 10 uc LVO/STO sample, respectively. Panel (a) shows simulated spectra with different V^{3+}/V^{2+} ratios and the best fit simulation for the 6 uc LVO/STO sample, giving a ratio of 85:15. Note that the spectrum cannot be reproduced by multiplet calculations using a pure V^{3+} reference spectrum either, and an average valence state of 2.85 is derived. The average valence derived from the simulations is in strong contrast to

the values derived from the fit using single crystal reference spectra. However, this should not be surprising, as for the fit spectra exhibiting valences from V^{3+} to V^{5+} were used, while simulations were done using spectra of V^{2+} and V^{3+} valences. The panel (b) of Fig. 5.15 shows the best fit simulations for the 10 uc sample for the various measurement geometries. As the experimental energy resolution is reduced for the spectra taken at 4 keV and 5 keV, simulations were convolved using a Gaussian width of 500 meV. In the case of 4 keV the simulations for both a 400 meV and a 500 meV broadening are shown. The average valences of both samples are given in Tab. 5.4 and show the same trend as the valence derived from the single crystal fits.

Table 5.4: *Average vanadium valence of 6 uc and 10 uc LVO/STO derived from fits based on multiplet calculations.*

depth profiling	average V valence	
	6 uc	10 uc
3 keV, 50°off	—	2.8
3 keV, 5°off	2.85	2.75
4 keV, 5°off	—	2.7
5 keV, 5°off	—	2.65

Discussion

Two ways of carrying out a quantitative analysis of the V $2p$ core-level spectra were presented. Both approaches face certain drawbacks. A fitting procedure based on single crystal reference spectra requires an absolute energy calibration. Although lacking a V^{2+} reference spectrum, the film spectra can be fitted quite accurately using V^{5+} to V^{3+} reference spectra. However, this results directly in a valence state $> 3+$. For the simulations based on multiplet calculations, V^{3+} and V^{2+} spectra were taken as a starting point, which led to the best fit for the V $3p_{3/2}$ core-level spectra. However, the absolute binding energies had to be corrected in this case. Although the final decision about which method describes the results best cannot be settled at this point, consequences and possibilities to validate the approaches shall be discussed and contrasted to the literature.

Both methods yield a valence state different from purely 3+ for the insulating 6 uc sample. The lower oxidation state derived for LVO/STO from the analysis, which is based on mulitplet calculations, would be in line with the results of Mossanek *et al.* [216]. By means of cluster calculations, they found an average V valence of 2.6 due to covalence and a strong contribution of the $3d^3\underline{L}^1$ state for LVO single crystals. However, this covalence has no influence on the insulating behavior of the samples as they found only minor occupation of the non-local $3d^3\underline{D}^1$ state, where $\underline{\mathrm{D}}$ denotes a hole in the next-

nearest V $3d$ state. Although in a simple Mott picture this implies that the ground state of the film does not exactly correspond a half-filling of the bands, the underlying physics remain unchanged, including the electrostatic doping of a Mott insulator.

All other explanations for both a higher and a lower V valence would imply some vacancy or excess atom formation with extra charges being trapped, as the ground state of the samples is insulating. For possible vacancies or excess atoms, all cation atoms can be most likely ruled out as possible sources as indicated by the reversibility of the reduction and oxidation series. This leaves an oxygen off-stoichiometry, may it be due to excess oxygen or oxygen vacancies, as a possible source. According to Maiti *et al.*, polycrystalline $La_{1-x}Ca_xO_{3+\delta}$ was stabilized for a δ between -0.01 to 0.04. Hur *et al.* reported the fabrication of $LaVO_{3-\delta}$ with a δ of up to 0.08 [230]. For other perovskites it is known that the oxygen stoichiometry strongly depends on the material. While STO tends to exhibit oxygen vacancies, excess oxygen can be incorporated in $LaTiO_{3+\delta}$ [231, 232]. This makes predictions for $LaVO_3$ difficult. However, as a higher oxidized phase exists for both LVO and $LaTiO_3$ – this is not the case for STO – the incorporation of excess oxygen seems likely, but has to be kept on a speculative level.

Any oxygen vacancies or excess oxygen will modify the picture of the electronic reconstruction and electrostatic doping. In either way, the starting point is shifted from a clean d^2 Mott insulator to a $d^{2\pm x}$ system which remains insulating due to the localization of the extra charge. As long as the oxygen vacancies or the excess oxygen atoms are randomly distributed in the film, the potential build-up will only slightly be influenced by increasing or decreasing the potential gradient, i. e., the critical thickness may be altered, leaving the mechanism and its result, namely the electrostatic doping of a Mott insulator, unchanged. An oxygen off-stoichiometry which delays the MIT may also explain the discrepancy to the literature regarding the critical overlayer thickness [19, 230].

To further shed light on this issue, a detailed analysis of the exact oxygen stoichiometry is of great importance. Oxygen sensitive TEM may give a further insight, but *ex situ* lamella preparation will have a strong influence. Furthermore, the analysis of a reduction and oxidation series of *in situ* grown LVO/STO films by means of UPS may give further information. The development of the LHB during reduction and oxidation may reveal the starting $3d$ configuration. In the ideal case, these measurements can be contrasted to *in situ* conductivity measurements.

5.5.3 Band bending and band alignment

The asymmetry of the Ti $2p_{3/2}$ core-level for the insulating 6 uc as well as the conducting 10 uc LVO/STO samples give the first indication for a band bending near the interface, as was already discussed in Sec. 5.5.1. However, if band bending is the reason for the asymmetry, a peak broadening or an asymmetry should be present at all other STO core-levels as well.

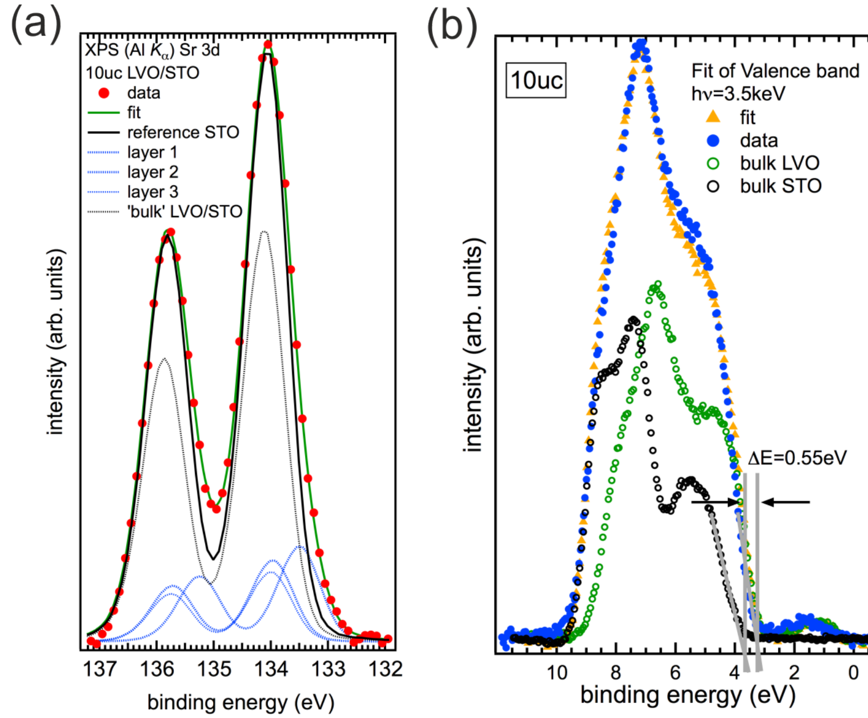

Figure 5.16: *(a) XPS spectra of the Sr 3d core-level for a 10 uc film, fitted with a STO reference. For details see text. (b) Fit of the valence band of the 10 uc film with weighted bulk LVO and STO reference data. From this a valence band offset of 0.55 eV is derived for LVO/STO.*

The Sr 3d core-level spectrum of the 10 uc LVO/STO sample is displayed in Fig. 5.16 (a). Compared to a STO reference spectrum this core-level, too, exhibits a distinct asymmetry at the lower binding energy side for both the insulating (not shown) and the conducting samples. This is in line with the findings at the Ti core-level (cf. Fig. 5.9). They both point towards an upward band bending at the interface. To quantify this effect, the Sr 3d peak was background-corrected including the subtraction of a La satellite. Bulk STO reference data was used to model the layer-resolved spectra taking the exponential damping of the photoemission signal into account. Thus, for a given mean free path, in this case λ_{eff}=25 Å (Al K_α, θ=8° off NE), the intensity of every layer is fixed. As shown in Fig. 5.16 (a), for layer 1, which is the first STO layer at the interface, the intensity is higher compared to the 2$^{\text{nd}}$ and 3$^{\text{rd}}$ layer. All layers below, from layer 4 onwards, are added up and labelled with bulk LVO/STO as there were only marginal energy shifts among these layers.

The calculated energy shifts are listed in Tab. 5.5 for the 6 uc and the 10 uc sample. For the insulating 6 uc sample, the shifts are smaller. The band bending is in upward direction, which indicates that there is no formation of an electron pocket at the STO-

Table 5.5: *Band offsets and band bending in the STO determined by XPS.*

	6 uc	10 uc
band bending [eV]		
1st layer	0.36±0.05	0.67±0.05
2nd layer	0.08±0.05	0.20±0.05
3rd layer	–	0.17±0.05
band offset (fit of VB) [eV]	0.54±0.05	0.55±0.05

side of the interface.* Furthermore, the band bending is strongly localized at the interface and reaches only about 3 uc into the STO substrate. An upward band bending at the interface on the STO side would also be expected from a comparison of the electron affinities of LVO (χ=5.5 eV) and STO (χ=3.9 eV) assuming Fermi-level alignment [233, 234].

In chapter 5.1, a schematic band alignment was proposed to motivate electronic reconstruction within the film layer itself and thus the Mott MIT by pure electrostatics. However, this hypothetical model was only based on literature values for the band gaps and the alignment of the 'O 2*p*' part of the valence band in both materials. As stated in Sec. 2.5, photoemission can be used to analyze valence band offsets.

The valence band was decomposed using bulk STO and bulk LVO reference spectra as shown in Fig. 5.16 (b) for the 10 uc film. Here, the photoemission spectra of 'bulk' LVO with weighted exponential damping factors was integrated over 10 uc. For STO, integration was done for an infinitely thick layer. In this case as well, the only free parameter was the shift in binding energy. The fit reproduces all features of the spectra quite accurately. The shift of the valence bands, as can be inferred from Fig. 5.16, is about 0.55 eV for both samples.

Table 5.6: *Band gap and electron affinities for STO and LVO bulk materials taken from the literature.*

	STO	LVO
band gap [eV]	3.3 [234]	Mott: 1.0 [207]
		CT: 3.9 [207]
electron affinity [eV]	3.9 [234]	5.5 [233]

In Tab. 5.6, literature values for the electron affinity, which is defined as the energy difference between the vacuum level and the lower edge of the lowest unoccupied band, and the band gap are given. These values cannot be measured by photoemission as

*A downward band bending is not observed for LAO/STO either. Here, the population of so-called *in-gap* states is discussed as a reason for the interface conductivity [180].

only occupied states are accessible for this method. The Mott gap was determined by optical methods and is thus the gap from the upper edge of the LHB to the lower edge of the UHB. The charge transfer gap (CT) in LVO is defined from the leading edge of the 'O 2*p*' part of the valence band to the lower edge of the UHB.

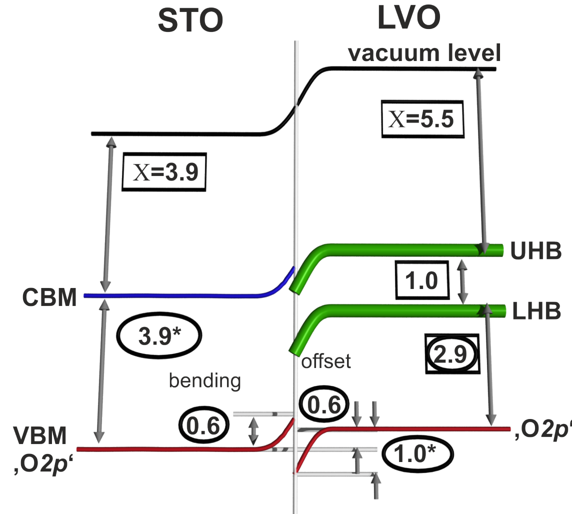

Figure 5.17: *Schematics of the possible band alignment in $LaVO_3/SrTiO_3$ heterostructures. In rectangles: literature values, in circles: measured values. For further explanations see text.*

Taking these values from the literature, a preliminary band diagram can be drawn (see Fig. 5.17). Literature values are labelled by rectangles, whereas measured data is given in circles. Discrepancies between measurement and literature values as well as features not observed in measurements are labelled with a star. The band bending in STO can be explained most likely by the difference in the electron affinities. The Fermi-level has to be somewhere between the conduction band minimum (CBM) and the valence band maximum in the STO, most likely close to the CBM. For LVO it lies in between the lower and upper Hubbard band. Assuming Fermi-level alignment in these heterostructures, the vacuum level has to be continuous, which directly leads to an upward bending in the STO and a downward bending in the LVO, both caused by the small Mott gap of LVO. However, the values of the band bending in the respective material depend on the precise position of the Fermi-level, which is not known. The band bending of 1 eV within the LVO is not measured either, but derived under the assumption that for both materials the Fermi-levels are close to the CBM and UHB, respectively. A downward band bending would make the UHB of the LVO more favorable with respect to the CBM of the STO and thus enable interface conductivity on the LVO side. Furthermore, no potential gradient was assumed within the LVO as this could not have been observed neither in the La core-level spectra, nor in the valence band spectra.

A severe discrepancy in this picture is the difference between the band gap of STO as derived from photoemission and the literature value. Although assuming the Fermi-level

to be pinned in the STO near the CBM due to impurity doping, the measured band gap is larger than the literature value (3.3 eV) and extends up to 3.9 eV for the LVO/STO heterostructures. A similar observation was made for LAO/STO heterostructures [235]. Charging effects can most likely be excluded for the conducting samples. However, surface and interface photovoltage effects caused by x-ray exposure cannot be excluded and further analyses have to be done for both the LAO/STO and the LVO/STO system [63, 64]. Another explanation for the large value of the STO band gap may be provided by a comparison to spectroscopic ellipsometry measurements. Although a band gap of 3.25 eV is derived, the main absorption edge is at about 3.8 eV and thus at a comparable value [237]. For LAO/STO, Susaki *et al.* reported changes in the work function with respect to the overlayer film thickness [236], which has a strong influence on the band diagram and could explain the thickness-dependent transport. To clarify this for LVO/STO, Kelvin probe experiments are desirable.

5.6 Summary and outlook

LVO/STO heterostructures were grown successfully by means of PLD. A thorough phase characterization revealed the LVO perovskite phase. Transport properties show similar behavior to LAO/STO heterostructures with a thickness-dependent conductivity most likely explained by an electronic reconstruction. HAXPES analyses clearly indicate a reconstruction within the film layer, not involving the STO substrate. However, the precise V valence remains unsettled. *In situ* conductivity and UPS measurements of, e. g., the 6 uc samples and their behavior upon reduction and oxidation may give further insight. Furthermore, other experiments, which independently determine the V valence state and the oxygen-stoichiometry, can be conducted. Regarding the former, XAS or resonant inelastic x-ray scattering measurements may provide additional information. The precise determination of the oxygen-stoichiometry for oxide thin films remains challenging and currently it does not seem possible to retrieve detailed information by any method.

Apart from the determination of the precise vanadium valence, the validity of the electronic reconstruction scenario should be further investigated. Conductivity measurements of a sample series exhibiting different overlayer thicknesses will verify or falsify the scaling of the sheet carrier density with the overlayer thickness. Moreover, all issues and findings for LAO/STO starting from the questions whether the ground state also hosts superconductivity and/or magnetism to the influence of a gate field on the conductivity are of strong interest for the LVO/STO as well, the latter being highly interesting for future 'Mottronic' applications [20].

Avoiding a potential built-up in the LVO in these heterostructures requires a reconstruction of both the interface and the surface. Up to now only interface effects that result from a charge transfer from the surface to the interface have been analyzed. However, the reconstruction mechansim at the surface remains unclear. The advantages of *in*

situ growth and analysis should enable LEED and UPS studies, which offer the possibility of further addressing this question. This should help to clarify the influence of surface adsorbates and the question whether the surface reconstructs atomically, electronically or by the creation of oxygen vacancies.

6 Summary

This thesis deals with the growth and characterization of three different oxide heterostructures, which are interesting for basic research on striking physical phenomena at interfaces, but also from a technological point of view.

The heterostructures formed by the ferrimagnetic Fe_3O_4 and the semiconducting ZnO is highly ranked as a material system suitable for spin injection. A comparative study of films grown by both pulsed laser deposition and molecular beam epitaxy revealed that by choosing an adequate oxygen pressure both methods are suitable to grow these heterostructures. A pressure variation during growth hindered the formation of a FeO-like interface layer. The high lattice mismatch between film and substrate causes an island-like growth mode, nevertheless the crystalline islands are in registry to the substrate. The islands that coalesce in thicker films exhibit a nearly relaxed lattice structure for a film thickness above 2 nm as proven by reflection high energy electron diffraction and x-ray diffraction. By photoemission and absorption experiments the electronic structure of Fe_3O_4 is identified, but a slight oxygen off-stoichiometry towards an overoxidation is present. Temperature-dependent coercivity measurements showed indications for the Verwey transistion characteristic of stoichiometric Fe_3O_4. This may point to an off-stoichiometry that is only present within the photoemission and absorption probing depth. X-ray magnetic circular dichroism and vibrating sample magnetometry show reduced magnetic moments, which cannot be entirely explained by temperature effects. However, anti-phase boundaries caused by the initial island growth might give an explanation as they act as domain wall pinning centers. As growth proved to be successful the next step would be to analyze the spin injection efficiency, for instance, by spin-dependent conductivity measurements.

The conducting interface between the two band insulators $LaAlO_3$ and $SrTiO_3$, which only occurs above a critical overlayer thickness, is discussed in the second part of this thesis. The origin of this conductivity is most likely an electronic reconstruction caused by the polar character of the $LaAlO_3$. However, electronic properties strongly depend on growth parameters like the total pressure, the oxygen partial pressure and a post-oxidation procedure. The detailed structural analysis of samples grown under different conditions revealed comparable properties, except for a higher degree of disorder that may be present in the samples grown at 10^{-1} mbar as indicated by the absence of reflection high energy electron diffraction oscillations during growth as well as scanning transmission electron microscopy analysis. By contrasting conductivity measurements to hard x-ray photoelectron spectroscopy studies the following conclusions can be drawn: (i) All samples grown at a total pressure of 10^{-1} mbar turned out to be insulating. (ii)

A growth pressure of 10^{-5} mbar leads to oxygen-vacancy-mediated conductivity in bulk $SrTiO_3$. (iii) The ratio of Ti^{3+} scales with the oxygen partial pressure, while macroscopic conductivity depends on the overall growth pressure. Thus, the presence of charge carriers does not necessarily lead to conductivity. Furthermore, this indicates that it is mainly the growth kinetics at high pressures that destroy conductivity. (iv) A post-oxidation procedure removes the arbitrariness in controlling the electronic interface properties by the oxygen pressure during growth and leads to a metastable state. By applying this procedure thickness-dependent conductivity is observed except for the sample exhibiting a higher degree of disorder in the film. This post-oxidation procedure can be seen as a basic prerequisite for samples grown by different groups to ensure comparability and to further analyze and study the properties of $LaAlO_3/SrTiO_3$.

The replacement of the band insulating $LaAlO_3$ by the Mott insulating $LaVO_3$, which is also a polar oxide, paves the way to study correlation effects at oxide interfaces. Structures were grown by pulsed laser deposition and a detailed structural analysis was carried out. Both reflection high energy electron diffraction patterns and oscillations show two-dimensional growth, which is also confirmed by atomic force microscopy. X-ray diffraction, x-ray reflectivity and scanning transmission electron microscopy reveal the perovskite phase without any impurity phases of this heterostructure. Conductivity was found above a LVO film thickness of 8 uc. Both, a sheet carrier density of about $10^{13}\,cm^{-2}$ and a high mobility of about $600\,cm^2/Vs$ at low temperatures closely relate this material system to $LaAlO_3/SrTiO_3$ and suggest a similar mechanism for the formation of the conducting interface, i. e., an electronic reconstruction. Hard x-ray photoelectron spectroscopy measurements, however, reveal that the reconstruction and thus the conductivity takes place within the film layer. Although the precise valence state of the vanadium cannot be settled, a charge transfer towards the interface is observed when analyzing the V $2p$ core-level. This observation distinguishes $LaVO_3/SrTiO_3$ from other heterostructures exhibiting interface conductivity. Electrostatic doping of a Mott insulator opens the possibility to study the band-filling-controlled Mott metal-insulator transition without suffering from chemical impurities.

Appendix

Table 6.1: *Table of investigated samples. Number, abbreviation, growth parameters.* *grown at the University of Twente by PLD, †grown at the University of Würzburg by MBE*

sample (no.)	abbreviation	thickness	pressure [mbar]	temperature [°C]	time [min]
		Fe_3O_4/ZnO			
ZnO_034*	sample A	4 nm	$1.1{\cdot}10^{-6}$	390	4.0
ZnO_029*	sample B	4 nm	$5.6{\cdot}10^{-6}$	390	5.5
ZnO_036*	sample C	4 nm	$2.5{\cdot}10^{-5}$–	390	1.0+
			$9.5{\cdot}10^{-6}$		3.0
ZnO_037*	sample D	19 nm	$3.3{\cdot}10^{-5}$–	390	1.0+
			$9.8{\cdot}10^{-6}$		20
ZnO_033*	sample E	4 nm	$8.7{\cdot}10^{-5}$	390	4.0
MgO_012*	sample F	57 nm	$1.0{\cdot}10^{-6}$	390	20
ZnO_14†	sample G	12 nm	$5.3{\cdot}10^{-6}$–	310	10+
			$1.0{\cdot}10^{-6}$		30
MgO_10†	sample H	18 nm	$2.5{\cdot}10^{-5}$	310	60
ZnO_018*	sample I	30 nm	$1.0{\cdot}10^{-5}$	390	30
ZnO_08†	sample J	3 nm	$1.0{\cdot}10^{-6}$	310	10
ZnO_09†	sample K	3 nm	$5.0{\cdot}10^{-6}$	310	10
ZnO_10†	sample L	7 nm	$5.0{\cdot}10^{-6}$	310	20

sample (no.)	abbreviation	thickness	pressure [mbar]	temperature [°C]
		LAO/STO		
STO_028*	HP	6 uc	10^{-1}	850
STO_031*	MP	6 uc	10^{-3}	850
STO_030*	LP	6 uc	10^{-5}	850
STO_047*	HP 2 uc	2 uc	10^{-1}	850
STO_043*	MP 2 uc	2 uc	10^{-3}	850
STO_048*	LP 2 uc	2 uc	10^{-5}	850
STO_055*	MIX MP	6 uc	10^{-3} (O_2)+ 10^{-1} (Ar)	850
STO_051*	MIX LP	6 uc	10^{-5} (O_2)+ 10^{-1} (Ar)	850
STO_0x2*	HP PO	6 uc	10^{-1} + post oxidized	850
STO_0x3*	LP MIX PO	6 uc	10^{-5} (O_2)+ 10^{-1} (Ar) post oxidized	850
STO_053*	MP PO	6 uc	10^{-3} + post oxidized	850
STO_058*	LP PO	6 uc	10^{-5} + post oxidized	850
		LVO/STO		
STO_041*	6 uc	6 uc	$1 \cdot 10^{-5}$	670
STO_057*		6 uc	$1 \cdot 10^{-5}$	670
STO_037*	10 uc	10 uc	$1 \cdot 10^{-5}$	670
STO_052*		10 uc	$1 \cdot 10^{-5}$	670
STO_024*	32 uc	32 uc	$1 \cdot 10^{-5}$	670
STO_060*	1 uc SVO + 9 uc LVO	10 uc	$1 \cdot 10^{-5}$	670

Bibliography

[1] C. L. Jia et al., Phys. Rev. B **79**, 081405 (R) (2009).

[2] S. Yuasa, T. Nagahama, A. Fukushima, Y. Suzuki, and K. Ando, Nat. Mater. **3**, 868 (2004).

[3] S. S. P. Parkin et al., Nat. Mater. **3**, 862 (2004).

[4] Editorial, Nat. Mater. **11**, 91 (2012).

[5] D. G. Schlom and J. Mannhart, Nat. Mater **10**, 168 (2011).

[6] A. P. Ramirez, Science **315**, 1377 (2007).

[7] J. Mannhart and D. G. Schlom, Science **327**, 1607 (2010).

[8] H. Y. Hwang et al., Nat. Mater. **11**, 103 (2012).

[9] C. Cen, S. Thiel, J. Mannhart, and J. Levy, Science **323**, 5917 (2009).

[10] G. Rijnders and D. H. A. Blank, Nature **433**, 369 (2005).

[11] S. Datta and B. Das, Appl. Phys. Lett. **56**, 665 (1990).

[12] M. Fonin et al., Phys. Rev. B **72**, 104436 (2005).

[13] Y. S. Dedkov, U. Rüdiger, and G. Güntherodt, Phys. Rev. B **65**, 064417 (2002).

[14] S. J. Pearton, D. P. Norton, K. Ip, Y. W. Heo, and T. Steiner, Superlattices and Microstruct. **34**, 3 (2003).

[15] A. Ohtomo and H. Y. Hwang, Nature **427**, 423 (2004).

[16] D. A. Dikin et al., arXiv: **1103.4006v1** (2011).

[17] S. Thiel, G. Hammerl, A. Schmehl, C. W. Schneider, and J. Mannhart, Science **313**, 1942 (2006).

[18] H. Y. Hwang, Science **313**, 1895 (2006).

[19] Y. Hotta, T. Susaki, and H. Y. Hwang, Phys. Rev. Lett. **99**, 236805 (2007).

[20] J. Chakhalian, A. J. Millis, and J. Rondinelli, Nat. Mater. **11**, 92 (2012).

[21] I. H. Inoue and M. J. Rozenberg, Adv. Funct. Mater. **18**, 2289 (2008).

[22] A. Y. Cho, Appl. Phys. Lett. **19**, 467 (1971).

[23] L. L. Chang, L. Esaki, W. E. Howard, and R. Ludeke, J. Vac. Sci. Technol. **10**, 11 (1973).

[24] M. König et al., Science **318**, 766 (2007).

[25] D. Dijkkamp et al., Appl. Phys. Lett. **51**, 619 (1987).

[26] I. Bozovic and J. N. Eckstein, Appl. Surf. Sci. **113/114**, 189 (1998).

[27] M. Strikovski and J. H. Miller, Appl. Phys. Lett. **73**, 1733 (1998).

[28] D. B. Geohegan, Thin Solid Films **220**, 138 (1992).

[29] M. A. Herman and H. Sitter, *Molecular Beam Epitaxy - Fundamentals and Current Status*, Springer, 1996.

[30] J. A. Venables, G. D. T. Spiller, and M. Hanbücken, Rep. Prog. Phys. **47**, 399 (1984).

[31] A. Fischer, H. Kühne, and H. Richter, Phys. Rev. Lett. **73**, 2712 (1994).

[32] R. Eason, *Pulsed laser deposition of thin films*, Wiley-VCH, 2007.

[33] W. Braun, *Applied RHEED - Reflection High-Engergy Electron Diffraction During Crystal Growth*, Springer, 1999.

[34] A. Ichimiya and P. I. Cohen, *Reflection High Energy Electron Diffraction*, Cambridge, 2004.

[35] J. M. McCoy, U. Korte, P. A. Maksym, and G. Meyer-Ehmsen, Surf. Sci. **261**, 29 (1992).

[36] J. N. Neave, B. A. Joyce, P. J. Dobson, and N. Norton, Appl. Phys. A **31**, 1 (1983).

[37] G. S. Petrich et al., J. Cryst. Growth **95**, 23 (1989).

[38] I. K. Robinson and D. J. Tweet, Rep. Prog. Phys. **55**, 599 (1992).

[39] M. Birkholz, *Thin Film Analysis by X-Ray Scattering: Techniques for Structural Characterization*, Wiley-VCH, 2005.

[40] H. Kiessig, Ann. Phys. **5**, 769 (1931).

[41] J. Als-Nielsen and D. McMorrow, *Elements of Modern X-Ray Physics*, Wiley, 2001.

[42] L. N'evot and P. Croce, Rev. Phys. Appl. **15**, 761 (1980).

[43] D. K. G. de Boer, Phys. Rev. B **51**, 5297 (1995).

[44] H. R. Hertz, Ann. Phys. Chem. **31**, 983 (1887).

[45] A. Einstein, Ann. Phys. **17**, 132 (1905).

[46] A. Damascelli, Z. Hussain, and Z.-X. Shen, Rev. Mod. Phys. **75**, 473 (2003).

[47] K. Siegbahn, Science **217**, 111 (1982).

[48] R. Claessen et al., New J. Phys. **11**, 125007 (2009).

[49] S. Hüfner, *Photoelectron Spectroscopy*, Springer, 2003.

[50] F. Reinert and S. Hüfner, New J. Phys. **7**, 97 (2005).

[51] J. J. Yeh and I. Lindau, At. Data Nucl. Data Tables **32**, 1 (1985).

[52] M. B. Trzhaskovskaya, V. I. Nefedov, and V. G. Yarzhemsky, Atom. Data Nucl. Data **77**, 97 (2001).

[53] M. B. Trzhaskovskaya, V. I. Nefedov, and V. G. Yarzhemsky, Atom. Data Nucl. Data **82**, 257 (2002).

[54] S. Tanuma et al., Surf. Interface Anal. **37**, 833 (2005).

[55] D. Briggs and M. P. Seah, editors, *Practical Surface Analysis*, Wiley, 1990.

[56] K. Kakushima et al., J. Appl. Phys. **104**, 104908 (2008).

[57] M. Minohara, I. Ohkubo, H. Kumigashira, and M. Oshima, Appl. Phys. Lett. **90**, 132123 (2007).

[58] G. Martin, A. Botchkarev, A. Rockett, and H. Morkoc, Appl. Phys. Lett. **68**, 2541 (1996).

[59] J. R. Waldrop and R. W. Grant, Appl. Phys. Lett. **68**, 2879 (1996).

[60] E. A. Kraut, R. W. Grant, J. R. Waldrop, and S. P. Kowalczyk, Phys. Rev. Lett. **44**, 1620 (1980).

[61] S. A. Chambers, T. Droubay, T. C. Kaspar, and M. Gutowski, J. Vac. Sci. Technol. B **22**, 2205 (2004).

[62] M. Perego and G. Seguini, J. Appl. Phys. **110**, 053711 (2011).

[63] M. H. Hecht, Phys. Rev. B **41**, 7918 (R) (1990).

[64] K. Horn, M. Alonso, and R. Cimino, Appl. Phys. Sci. **56-58**, 271 (1992).

[65] D. D. Awschalom and M. E. Flatte, Nat. Phys. **3**, 153 (2007).

[66] H. Ohno, Science **281**, 951 (1998).

[67] S. A. Wolf et al., Science **294**, 1488 (2001).

[68] Z. Zhang and S. Satpathy, Phys. Rev. B **44**, 13319 (1991).

[69] M. Holub and P. Bhattacharya, J. Phys. D. Appl. Phys. **40**, R179 (2007).

[70] R. Fiederling et al., Nature **402**, 787 (1999).

[71] D. C. Look, Mater. Sci. Eng. B **80**, 383 (2001).

[72] S. A. Chambers, Adv. Mater. **22**, 219 (2010).

[73] S. Ghosh et al., Appl. Phys. Lett. **86**, 232507 (2005).

[74] A. Yanase and N. Hamade, J. Phys. Soc. Jpn. **68**, 1607 (1999).

[75] G. A. Samara and G. A. Giardini, Phys. Rev. **186**, 577 (1969).

[76] P. Seneor et al., Appl. Phys. Lett. **74**, 4017 (1999).

[77] P. J. van der Zaag et al., J. Magn. Magn. Mater. **211**, 301 (2000).

[78] T. Kado, Appl. Phys. Lett. **92**, 092502 (2008).

[79] E. J. W. Verwey, Nature **144**, 327 (1939).

[80] D. Schrupp et al., Europhys. Lett. **70(6)**, 789 (2005).

[81] R. Aragón, Phys. Rev. B **46**, 5328 (1992).

[82] G. Schmidt, D. Ferrand, L. W. Molenkamp, A. T. Filip, and B. J. van Wees, Phys. Rev. B **62**, R4790 (2000).

[83] P. A. Miles, W. B. Westphal, and A. von Hippel, Rev. Mod. Phys. **29**, 279 (1957).

[84] S. Agrawal, M. B. A. Jalil, S. G. Tan, K. L. Teo, and T. Liew, Phys. Rev. B **72**, 075352 (2005).

[85] M. B. A. Jalil, S. G. Tan, S. B. Kumar, and S. Bae, Phys. Rev. B **73**, 134417 (2006).

[86] M. Paul et al., Phys. Rev. B **79**, 233101 (2009).

[87] W. Weiss and M. Ritter, Phys. Rev. B **59**, 5201 (1999).

[88] P. W. Tasker, J. Phys. C: Solid State Phys. **12**, 4977 (1979).

[89] Z. Kąkol and J. M. Honig, Phys. Rev. B **40**, 9090 (1989).

[90] N. G. Condon et al., Phys. Rev. B **55**, 15885 (1996).

[91] B. Carvello and L. Ranno, J. Magn. Magn. Mater. **272**, 1926 (2004).

[92] Y. X. Lu et al., Phys. Rev. B **70**, 233304 (2004).

[93] D. T. Margulies et al., Phys. Rev. B **53**, 9175 (1996).

[94] M. S. Park, J.-H. Song, and A. J. Freeman, Phys. Rev. B **79**, 024420 (2009).

[95] T. Schedel-Niedrig, W. Weiss, and R. Schlögl, Phys. Rev. B **52**, 17449 (1995).

[96] J. F. Anderson et al., Phys. Rev. B **56**, 9902 (1997).

[97] W. Kim, K. Kawaguchi, N. Koshizaki, M. Sohma, and T. Matsumoto, J. Appl. Phys. **93**, 8032 (2003).

[98] C. Ruby, J. Fusy, and J.-M. R. Genin, Thin Solid Films **352**, 22 (1999).

[99] F. C. Voogt et al., Phys. Rev. B **60**, 11194 (1999).

[100] B. Handke, J. Haber, T. Slezak, M. Kubik, and J. Korecki, Vacuum **63**, 331 (2001).

[101] E. J. Preisler, J. Brooke, N. C. Oldham, and T. C. McGill, J. Vac. Sci. Technol. B **21**, 1745 (2003).

[102] S. M. Watts, K. Nakajima, S. van Dijken, and J. M. D. Coey, J. Appl. Phys. **95**, 7465 (2004).

[103] S. Jain, A. O. Adeyeye, and C. B. Boothroyd, J. Appl. Phys. **97**, 093713 (2005).

[104] M. Ferhat and K. Yoh, Appl. Phys. Lett. **90**, 112501 (2007).

[105] A. Nielsen et al., Appl. Phys. Lett. **93**, 162510 (2008).

[106] P. Li, B. L. Guo, and H. L. Bai, J. Appl. Phys. **109**, 013908 (2011).

[107] C. W. Schneider et al., Appl. Phys. Lett. **97**, 192107 (2010).

[108] D. M. Lind, S. D. Berry, G. Chern, H. Mathias, and L. R. Testardi, Phys. Rev. B **45**, 1838 (1992).

[109] T. Fujii et al., Phys. Rev. B **59**, 3195 (1999).

[110] S. A. Chambers and S. A. Joyce, Surf. Sci. **420**, 111 (1999).

[111] S. A. Chambers, Surf. Sci. Rep. **39**, 105 (2000).

[112] C. R. Brundle, T. J. Chuang, and K. Wandelt, Surf. Sci. **68**, 459 (1977).

[113] N. S. McIntyre and D. G. Zetaruk, Anal. Chem. **49**, 1521 (1977).

[114] T. Yamashita and P. Hayes, Appl. Surf. Sci. **254**, 2441 (2008).

[115] P. Mills and J. L. Sullivan, J. Phys. D. Appl. Phys. **16**, 723 (1983).

[116] X. Gu et al., J Mater. Sci-Mater. El. **15**, 373 (2004).

[117] H.-J. Ko et al., J. Cryst. Growth **269**, 493 (2004).

[118] C. N. Chinnasamy et al., IEEE T. Magn. **38(5)**, 2640 (2002).

[119] J. Wang, T. Deng, and Y. Dai, J. Alloy. Compd. **390**, 127 (2005).

[120] H. Fjellvåg, F. Grønvold, S. Stolen, and B. Hauback, J. Solid State Chem. **124**, 52 (1996).

[121] S. Gota, E. Guiot, M. Henriot, and M. Gautier-Soyer, Phys. Rev. B **60**, 14387 (1999).

[122] D. Wett, A. Demund, H. Schmidt, and R. Szargan, Appl. Surf. Sci. **254**, 2309 (2008).

[123] M. Paul, *Molecular beam epitaxy and properties of magnetite thin films on semiconducting substrates*, PhD thesis, University of Würzburg, EP4, 2010.

[124] N. Berdunov, S. Murphy, G. Mariotto, and I. V. Shvets, Phys. Rev. B **70**, 085404 (2004).

[125] M. Ritter and W. Weiss, Surf. Sci. **432**, 81 (1999).

[126] S. S. Perry and P. B. Merrill, Surf. Sci. **383**, 268 (1997).

[127] M. A. James, F. C. Voogt, L. Niesen, O. C. Rogojanu, and T. Hibma, Surf. Sci. **402**, 332 (1998).

[128] X. W. Li, A. Gupta, G. Xiao, W. Qian, and V. P. Dravid, Appl. Phys. Lett. **73**, 3282 (1998).

[129] E. Pellegrin et al., phys. stat. sol. (b) **215**, 797 (1999).

[130] M. Gorgoi et al., Nucl Instrum Meth A **601**, 48 (2009).

[131] C. T. Chen et al., Phys. Rev. Lett. **75**, 152 (1995).

[132] J. J. Stöhr and H. C. Siegmann, *Magnetism: From fundamentals to nanoscale dynamics*, Springer-Verlag, 2006.

[133] D. Kufer, Wachstum und Eigenschaften von dünnen Magnetitfilmen auf Halbleitersubstraten, Master's thesis, University of Würzburg, EP4, 2010.

[134] E. Goering, S. Gold, M. Lafkioti, and G. Schütz, Europhys. Lett. **73**, 97 (2006).

[135] M. Kallmayer et al., J. Appl. Phys. **103**, 07D715 (2008).

[136] F. Schedin, E. W. Hill, G. van der Laan, and G. Thornton, J. Appl. Phys. **96**, 1165 (2004).

[137] S. Foner, Rev. Sci. Instrum. **30**, 548 (1959).

[138] Z. Q. Qiu and S. D. Bader, Rev. Sci. Instrum. **71**, 1243 (2000).

[139] S. Celotto, W. Eerenstein, and T. Hibma, Eur. Phys. J. B **36**, 271 (2003).

[140] W. Eerenstein, T. T. M. Palstra, T. Hibma, and S. Celotto, Phys. Rev. B. **68**, 014428 (2003).

[141] T. Hibma et al., J. Appl. Phys. **85**, 5291 (1999).

[142] F. C. Voogt et al., Phys. Rev. B **57**, R8107 (1998).

[143] A. M. Bataille et al., Phys. Rev. B **74**, 155438 (2006).

[144] O. Özdemir, D. J. Dunlop, and B. M. Moskowitz, Earth Planet Sc. Lett. **194**, 343 (2002).

[145] M. Büttner et al., J. Magn. Magn. Mater. **323**, 1179 (2011).

[146] M. Bohra et al., J. Magn. Magn. Mater. **321**, 3738 (2009).

[147] R. Aragón, D. J. Buttrey, J. P. Shepherd, and J. M. Honig, Phys. Rev. B **31**, 430 (1985).

[148] M. Paul et al., Appl. Phys. Lett. **98**, 012512 (2011).

[149] S. Brück et al., Appl. Phys. Lett. **100**, 081603 (2012).

[150] C. H. Ahn, K. M. Rabe, and J.-M. Triscone, Science **303**, 488 (2004).

[151] T. Yoshida et al., Europhys. Lett. **59(2)**, 258 (2002).

[152] M. Huijben et al., Adv. Mater. **21**, 1665 (2009).

[153] K. A. Müller and W. Berlinger, Phys. Rev. Lett. **21**, 814 (1968).

[154] N. Reyren et al., Science **317**, 1196 (2007).

[155] A. Brinkman et al., Nat. Mater. **6**, 493 (2007).

[156] J. A. Bert et al., Nat. Phys. **7**, 767 (2011).

[157] C. Cancellieri et al., Europhys. Lett. **91**, 17004 (2010).

[158] N. Nakagawa, H. Y. Hwang, and D. A. Muller, Nat. Mater. **5**, 204 (2006).

[159] J. Lee and A. A. Demkov, Phys. Rev. B **78**, 193104 (2008).

[160] Z. S. Popović, S. Satpathy, and R. M. Martin, Phys. Rev. Lett. **101**, 256801 (2008).

[161] R. Pentcheva and W. E. Pickett, Phys. Rev. Lett. **102**, 107602 (2009).

[162] Y. Li and J. Yu, J. Appl. Phys. **108**, 013701 (2010).

[163] Y. Segal, J. H. Ngai, J. W. Reiner, F. J. Walker, and C. H. Ahn, Phys. Rev. B **80**, 241107(R) (2009).

[164] M. Takizawa, S. Tsuda, T. Susaki, H. Y. Hwang, and A. Fujimori, Phys. Rev. B **84**, 245124 (2011).

[165] L. Zhang et al., Phys. Rev. B **82**, 125412 (2010).

[166] Z. Zhong, P. X. Xu, and P. J. Kelly, Phys. Rev. B **82**, 165127 (2010).

[167] Y. Li, S. N. Phattalung, S. Limpijumnong, and J. Yu, Phys. Rev. B **84**, 245307 (2011).

[168] H. Boschker et al., An alternative model for conductivity at the $LaAlO_3/SrTiO_3$ interface based on the induced polarization in the $SrTiO_3$, submitted to J. Chem. Phys.

[169] A. Savoia et al., Phys. Rev. B **80**, 075110 (2009).

[170] N. Ogawa et al., Phys. Rev. B **80**, 081106(R) (2009).

[171] H. L. Cai, X. S. Wub, and J. Gao, Chem. Phys. Lett. **467**, 313 (2009).

[172] W. Siemons et al., Phys. Rev. B **76**, 155111 (2007).

[173] J.-L. Maurice et al., Europhys. Lett. **82**, 17003 (2008).

[174] J.-L. Maurice et al., Mater. Sci. Eng. B **144**, 1 (2007).

[175] A. S. Kalabukhov et al., Phys. Rev. Lett. **103**, 146101 (2009).

[176] P. R. Willmott et al., Phys. Rev. Lett. **99**, 155502 (2007).

[177] A. Kalabukhov et al., Europhys. Lett. **93**, 37001 (2011).

[178] M. Sing et al., Phys. Rev. Lett. **102**, 176805 (2009).

[179] G. Berner et al., Phys. Rev. B **82**, 241405 (2010).

[180] A. Koitzsch et al., Phys. Rev. B **84**, 245121 (2011).

[181] G. Drera et al., Appl. Phys. Lett. **98**, 052907 (2011).

[182] M. Salluzzo et al., Phys. Rev. Lett. **102**, 166804 (2009).

[183] A. Kalabukhov et al., Phys. Rev. B **75**, 121404(R) (2007).

[184] C. Aruta et al., Appl. Phys. Lett. **97**, 252105 (2010).

[185] G. Koster, B. L. Kropman, G. Rijnders, D. H. A. Blank, and H. Rogalla, Appl. Phys. Lett. **73**, 2920 (1998).

[186] T. Ohnishi et al., Appl. Phys. Lett. **74**, 2531 (1999).

[187] J. E. Kleibeuker et al., Adv. Funct. Mater. **20**, 3490 (2010).

[188] G. Rijnders, *The Initial Growth of Complex Oxides*, PhD thesis, University of Twente, 2001.

[189] L. Reimer, *Transmission electron microscopy*, Springer, 1989.

[190] R. F. Egerton, Rep. Prog. Phys. **72**, 016502 (2009).

[191] M. Huijben et al., Nat. Mater. **5**, 556 (2006).

[192] J. Verbeeck et al., Phys. Rev. B **81**, 085113 (2010).

[193] P. D. Nellist and S. J. Pennycook, Ultramicroscopy **78**, 111 (1999).

[194] L. J. van der Pauw, Philips Res. Repts **13**, 1 (1958).

[195] W. Drube, T. M. Grehk, R. Treusch, and G. Materlik, J. Electron Spec. Rel. Phenom. **88-91**, 683 (1998).

[196] C. Aruta et al., arXiv: **1201.0454v1** (2011).

[197] S. Thiel et al., Phys. Rev. Lett. **102**, 046809 (2009).

[198] *NIST Standard Reference Database 71, NIST Electron Inelastic-Mean-Free-Path Database: Ver. 1.1, URL http://www.nist.gov/srd/nist71.htm.*

[199] D. Shirley, Phys. Rev. B **5**, 4709 (1972).

[200] S. Doniach and M. Sunjic, J. Phys. C: Solid State Phys. **3**, 285 (1970).

[201] M. Basletic et al., Nat. Mater. **7**, 621 (2008).

[202] C. Cen et al., Nat. Mater. **7**, 298 (2008).

[203] S. A. Chambers et al., Phys. Rev. Lett. **107**, 206802 (2011).

[204] A. Kalabukhov, R. Gunnarsson, T. Claeson, and D. Winkler, arXiv: **0704.1050v1** (2007).

[205] P. Perna et al., Appl. Phys. Lett. **97**, 152111 (2010).

[206] P. Moetakef et al., Appl. Phys. Lett. **99**, 232116 (2011).

[207] T. Arima, Y. Tokura, and J. B. Torrance, Phys. Rev. B **48**, 17006 (1993).

[208] N. F. Mott, Proceedings of the Physical Society **62**, 416 (1949).

[209] J. Hubbard, Proceedings of the Royal Society of London Series A **276**, 238 (1963).

[210] P. A. Lee, N. Nagaosa, and X.-G. Wen, Rev. Mod. Phys. **78**, 17 (2006).

[211] M. Imada, A. Fujimori, and Y. Tokura, Rev. Mod. Phys. **70**, 1039 (1998).

[212] J. S. Lee, M. W. Kim, and T. W. Noh, New J. Phys. **7**, 147 (2005).

[213] F. Inaba, T. Arima, T. Ishikawa, T. Katsufuji, and Y. Tokura, Phys. Rev. B **52**, 2221(R) (1995).

[214] A. Fujimori et al., J. Electron Spectrosc. **117**, 277 (2001).

[215] R. J. O. Mossanek et al., Phys. Rev. B **78**, 075103 (2008).

[216] R. J. O. Mossanek et al., J. Phys.: Condens. Matter **22**, 095601 (2010).

[217] H. Wadati et al., J. Appl. Phys. **102**, 053707 (2007).

[218] L. F. Kourkoutis, Y. Hotta, T. Susaki, H. Y. Hwang, and D. A. Muller, Phys. Rev. Lett. **97**, 256803 (2006).

[219] P. Bordet et al., J. Solid State Chem. **106**, 253 (1993).

[220] Y. Hotta et al., Appl. Phys. Lett. **89**, 031918 (2006).

[221] L. Fitting-Kourkoutis, D. A. Müller, Y. Hotta, and H. Y. Hwang, Appl. Phys. Lett. **91**, 163101 (2007).

[222] A. Müller et al., Oxygen growth pressure effects on the physics of $LaAlO_3/SrTiO_3$ heterostructures, in preparation.

[223] K. Maiti and D. D. Sarma, Phys. Rev. B **61**, 2525 (1999).

[224] R. Zimmermann, R. Claessen, F. Reinert, P. Steiner, and S. Hüfner, J. Phys.: Condens. Matter **10**, 5697 (1998).

[225] S. Glawion et al., Phys. Rev. B **80**, 155119 (2009).

[226] J. E. Kleibeuker, *Reconstructions at complex oxide interfaces*, PhD thesis, University of Twente, IMS, 2012, private communications.

[227] E. Stavitski and F. M. F. de Groot, Mircon **41**, 687 (2010).

[228] F. M. F. de Groot, Coordin. Chem. Rev. **249**, 31 (2005).

[229] F. M. F. de Groot and A. Kotani, *Core Level Spectroscopy of Solid*, Taylor & Francis Group, 2008.

[230] N. H. Hur et al., Solid State Commun. **92**, 541 (1994).

[231] M. E. Zvanut et al., J. Appl. Phys. **104**, 064122 (2008).

[232] A. Schmehl, F. Lichtenberg, H. Bielefeldt, J. Mannhart, and D. G. Schlom, Appl. Phys. Lett. **82**, 3077 (2003).

[233] S. F. Matar and G. Campet, J. Phys. Chem. Solids **68**, 331 (2007).

[234] J. Robertson and B. Falabretti, Mater. Sci. Eng. B **135**, 267 (2006).

[235] G. Berner, HAXPES study of the band alignment in LAO/STO heterostructures, private communication.

[236] T. Susaki, A. Makishima, and H. Hosono, Phys. Rev. B **84**, 115456 (2011).

[237] K. van Benthem, C. Elsässer, and R. H. French, J. Appl. Phys. **90**, 6156 (2001).

List of own publications

- **A. Müller**, H. Boschker, F. Pfaff, G. Berner, W. Drube, G. Koster, G. Rijnders, D. H. A. Blank, M. Sing, and R. Claessen, *Fabrication dependent properties of $LaAlO_3/SrTiO_3$ studied by hard X-ray photoemission spectroscopy*, in preparation.

- **A. Müller**, H. Boschker, F. Pfaff, G. Koster, G. Rijnders, D. H. A. Blank, M. Sing, and R. Claessen, *Spectroscopic evidence of electron transfer at the interface of $LaVO_3/SrTiO_3$ heterostructures*, submitted to PRL.

- H. Boschker, A. Brinkman, **A. Müller**, G. Hassink, M. Huijben, J. Kleibeuker, G. Koster, D. H. A. Blank, G. Rijnders, M. Sing, and R. Claessen, *An alternative model for conductivity at the $LaAlO_3/SrTiO_3$ interface based on the induced polarization in the $SrTiO_3$*, submitted.

- S. Brück, M. Paul, H. Tian, **A. Müller**, D. Kufer, C. Praetorius, K. Fauth, P. Audehm, E. Goering, J. Verbeeck, G. Van Tendeloo, M. Sing, and R. Claessen, *Magnetic and electronic properties of the interface between half metallic Fe_3O_4 and semiconducting ZnO*, Applied Physics Letters **100**, 081603 (2012).

- M. Paul, D. Kufer, **A. Müller**, A. Ruff, M. Kamp, N. J. C. Ingle, M. Sing, and R. Claessen, *Fe_3O_4/ZnO: A high-quality magnetic oxide-semiconductor heterostructure*, Journal of Applied Physics **110**, 073519 (2011).

- **A. Müller**, A. Ruff, M. Paul, A. Wetscherek, G. Berner, U. Bauer, C. Praetorius, K. Fauth, M. Przybylski, M. Gorgoi, M. Sing, and R. Claessen, *Fe_3O_4 on ZnO: A spectroscopic study of film and interface properties*, Thin Solid Films **520**, 368 (2011).

- M. Paul, D. Kufer, **A. Müller**, S. Brück, E. Goering, M. Kamp, J. Verbeeck, H. Tian, G. van Tendeloo, N.J.C. Ingle, M. Sing, and R. Claessen, *Fe_3O_4/ZnO: A high-quality magnetic oxide-semiconductor heterostructure by reactive deposition*, Applied Physics Letters **98**, 012512 (2011).

- R. Claessen, M. Sing, M. Paul, G. Berner, A. Wetscherek, **A. Müller**, and W. Drube, *Hard X-ray photoelectron spectroscopy of oxide hybrid and heterostructures: a new method for the study of buried interfaces*, New Journal of Physics **11**, 125007 (2009).

- M. Paul, **A. Müller**, A. Ruff, B. Schmid, G. Berner, M. Sing, R. Claessen, and M. Mertin, *Probing the interface of Fe_3O_4/GaAs thin films by hard X-ray photoelectron spectroscopy*, Physical Review B **79**, 233101 (2009).

- M. Sing, G. Berner, K. Goß, **A. Müller**, A. Ruff, A. Wetscherek, S. Thiel, J. Mannhart, S. A. Pauli, C. W. Schneider, P. R. Willmott, M. Gorgoi, F. Schäfers, and R. Claessen, *Profiling the interface electron gas of $LaAlO_3/SrTiO_3$ heterostructures by hard X-ray photoelectron spectroscopy*, Physical Review Letters **102**, 176805 (2009).

- B. Schmid, **A. Müller**, M. Sing, R. Claessen, J. Wenisch, K. Brunner, L. Molenkamp, and W. Drube, *Surface segregation of interstitial manganese in $Ga_{1-x}Mn_xAs$ studied by hard X-ray photoemission spectroscopy*, Physical Review B **78**, 075319 (2008).

- **A. Müller**, *Photoemissionsspektroskopie an nasschemisch präparierten Oberflächen verdünnter magnetischer Halbleiter*, diploma thesis (2007).

Acknowledgement

Als erstes möchte ich mich bei Herrn Prof. R. Claessen bedanken, der es mir ermöglicht hat in seiner Gruppe zu lernen und zu arbeiten. Ich konnte hier mein Wissen im Bereich der Festkörperphysik stark vertiefen. Desweiteren möchte ich danke sagen für die Möglichkeit ein Jahr meiner Doktorandenzeit im Ausland zu verbringen und an zahlreichen internationalen Konferenzen teilzunehmen.

Hartelijke dank ook aan Prof. D. Blank, Prof. G. Rijnders en G. Koster. Ik heb een hele mooie tijd met het team gehad en kon daarbij alles over PLD, XRD en veles meer leren. Vooral de verklaringen van het AFM van Dave hoogst persoonlijk zal ik niet gauw vergeten! Naast het werken en leren kwamen de borrels niet te kort, bedankt. Verder bedanke ik me bij Prof. G. Rijnders voor die bereidheid tweede experte van dit proefschrift te zijn.

Desweiten danke ich PD M. Sing für die Unterstützung in den letzen vier Jahren und seine physikalischen Ratschläge, wenn sie mal wieder von Nöten waren. Nochmals danke für das Korrekturenlesen meiner Arbeit.

Furthermore, I would like to thank the following persons:

- Prof. G. Sangiovanni für die Bereitschaft 3. Prüfer im Promotionskolloquium zu sein
- all people joining me to beamtimes for their help and night shifts
- all beamline scientists and their help also during night shifts
- A. Ruff und M. Paul für die Zusammenarbeit in der Magnetitforschung
- G. Berner und F. Pfaff für die Zusammenarbeit im Bereich der Heterostrukturforschung
- Prof. K. Fauth, C. Praetorius and D. Kufer für die XMCD Messungen und Auswertung
- Dr. J. Verbeeck, S. Lichtert and Prof. M. Kamp for the magnificent STEM images and the data analysis
- H. Boschker and N. H. Hansen for the help with XRD and XRR measurements

- U. Bauer für die MOKE Messungen
- S. Glawion für die Multiplet Rechnungen
- Hans, Sebastian, Andreas and Anita for proofreading and much more...
- allen Mitarbeitern vom Lehrstuhl EP4 für das angenehme Arbeitsklima und die Gespräche am Mittagstisch
- een verdere dank gaat natuurlijk aan het oude Comat Team, dat zijn Hans, Josée, Jeroen, Joost en Bouwe. Jullie hebben ervoor gezord, dat ik me in jullie groep gelijk opgenomen en thuis voelde. Zowel bij borrels, bbq's, bij mountainbike, op konzerten, bij schaatsen, zo ook in het stadion van Twente tegen Schalke. Het was altijd vrolijk en bereidde me steeds enorm veel plezier. Oh ja, het laboratorium was ook geweldig en heb van jullie een heleboel geleerd!
- alle andere personen van IMS voor die vriendelijke opname van een Duitser
- meinen Mitbewohnern, den Drei Amigos, wer auch immer gerade dazugehört, für den angenehmen Aufenthalt hier in Würzburg
- und natürlich der Seele von EP4, Moni Seifer. Sie hat mir immer mit Rat und Tat zur Seite gestanden und ich möchte ihr besonders für die Hilfe und Unterstützung danken

Zuletzt will ich natürlich allen meinen Freunden, meiner Freundin und meinen Eltern für die Unterstützung und den Rückhalt, nicht nur in den letzten fünf Jahren, danken. Ohne euch hätte ich vieles nicht so leicht und die letzten Wochen vielleicht gar nicht gemeistert.